ORBITAL ORDER IN IRON-BASED SUPERCONDUCTORS

BY

WEICHENG LV

DISSERTATION

Submitted in partial fulfillment of the requirements
for the degree of Doctor of Philosophy in Physics
in the Graduate College of the
University of Illinois at Urbana-Champaign, 2012

Urbana, Illinois

Doctoral Committee:

Professor Eduardo Fradkin, Chair
Professor Philip Phillips, Director of Research
Professor Peter Abbamonte
Professor John Stack

Abstract

In this thesis, we propose that a ferro-orbital order, which breaks the degeneracy between the Fe d_{xz} and d_{yz} orbitals, is the effective cause of the structural and the magnetic transitions in the iron-based superconductors. We will discuss this orbital order in the framework of the local-itinerant dichotomy. First, due to the spatial anisotropy of the occupied orbitals that form the local moments, the magnetic exchange constants acquire dramatically different values along the two in-plane directions. Second, the itinerant electrons also undergo a nematic transition, causing the anisotropy observed in various experiments. Finally, combining orbital order in both the local moments and itinerant electrons, we find that the underlying magnetism is unfrustrated, consistent with the inelastic neutron scattering results.

The thesis is organized as follows. We will first provide the necessary background knowledge of the iron-based superconductors in Chapter 1. As a preliminary, we discuss in detail three different theoretical approaches, namely the weak-coupling, strong-coupling and local-itinerant models. Chapter 2 serves as the motivation of the thesis. Various experimental results will be presented to demonstrate the existence of the in-plane anisotropy. We will introduce two distinct theoretical scenarios that account for the nematic order. We will argue that orbital order, instead of the spin-nematic order, is the underlying mechanism. Chapters 3, 4, and 5 are the main contents of the thesis. In Chapter 3, we will study the orbital order from the strong-coupling theories, with emphasis on the Kugel-Khomskii model. Chapter 4 deals with the orbital order in the weak-coupling theories and its experimental consequences. Finally in Chapter 5, we propose the degenerate double-exchange model, and show how the orbital order in the itinerant electrons leads to the unfrustrated effective spin model.

To Lingling and my parents.

Acknowledgments

First I would like to thank my advisor, Philip Phillips. In the early years, he closely directed me in different research projects. His guidance and patience helped me go through those unproductive days. After my research work took shape, he started to encourage me to pursue my own ideas. This experience made me better prepared to be an independent researcher. Without Philip's continuous efforts and supports, this thesis is simply impossible.

I have been very fortunate to work with Frank Früger and Wei-Cheng Lee. They not only educated me with their knowledge, but also shared with me their brilliant ideas. I am grateful to them for being my collaborators. I also would like to thank fellow group members, Jiansheng Wu for jointly developing the idea of orbital order, Ting-Pong Choy for some earlier collaboration, and Seungmin Hong for sharing the office, and numerous academic and nonacademic discussions there.

For the people at the Department of Physics, I am especially grateful to Laura Greene for her efforts to establish a close collaboration between the experimentalists and theorists. Her group members, Hamood Arham and Wan Kyu Park, were always willing to share their data, for which I wish to have a better explanation. I also would like to thank my thesis committee members, Eduardo Fradkin, Peter Abbamonte, and John Stack. Finally, I thank all the members of the condensed matter theory discussion group, especially Man-Hong Yung and Ching-Kai Chiu for organizing the meetings.

The research community of the iron-based superconductors is always inspiring. I benefited from many helpful conversations with my colleagues from other institutions. The incomplete list in alphabetical order includes Milan Allan, James Analytis, Cheng-Chien Chen, Jiun-Haw Chu, Andrey Chubukov, Elbio Dagotto, Pengcheng Dai, Séamus Davis, Daniel Dessau, Rafael Fernandes, Dong-Hui Lu, Wei Ku, Adriana Moreo, Qimiao Si, Qiang Wang, Ming Yi, and Rong Yu. Among those, I am especially grateful to Elbio Dagotto for giving me a second chance so that I can graduate on time.

My deepest gratitude goes to Lingling Miao and my parents for their unconditional love and support. It is to them that this thesis is dedicated. I am also thankful to all my friends, who always gave me good cheers for my many years at Urbana.

The work presented in this thesis is supported by the teaching assistantship from the Department of Physics, University of Illinois; by the National Science Foundation under Grant No. DMR-0605769 and DMR-0940992; and by the Center for Emergent Superconductivity, an Energy Frontier Research Center funded by the U.S. Department of Energy, Office of Science, Office of Basic Energy Sciences under Award No. DE-AC0298CH1088.

Table of Contents

List of Figures

List of Abbreviations

AFM	Antiferromagnetic.
ARPES	Angle-resolved photoemission spectroscopy.
BZ	Brillouin zone.
DDEX	Degenerate double-exchange.
DFT	Density functional theory.
DMFT	Dynamical mean-field theory.
DOS	Density of states.
FM	Ferromagnetic.
FRG	Functional renormalization group.
INS	Inelastic neutron scattering.
LDA	Local density approximation.
NN	Nearest neighbor.
NNN	Next nearest neighbor.
PCS	Point contact spectroscopy.
PM	Paramagnetic.
QPI	Quasiparticle interference.
RA	Resistivity anomaly.
RIXS	Resonant inelastic x-ray scattering.
RPA	Random phase approximation.
SC	Superconductivity.
SDW	Spin density wave.
SPT	Structural phase transition.
SQUID	Superconducting quantum interference device.
STM	Scanning tunneling microscopy.
XAS	X-ray absorption.

List of Symbols

$A(k, \omega)$	Spectral function.
$\mathcal{G}(k, \omega)$	Green function.
$g(k)$	Superconducting structure function.
J	Magnetic exchange or Hund's coupling.
J'	Pairing hopping energy.
J_{H}	Hund's coupling.
m	Magnetic moment.
n	Electron filling level.
T_c	Superconducting transition temperature.
T_{K}	Kondo temperature.
T_N	Néel temperature.
$T_{\mathcal{N}}$	Nematic transition temperature.
T_S	Structural transition temperature.
T_{SDW}	Spin-density-wave onset temperature.
$\boldsymbol{Q}$	Magnetic ordering wave vector.
U	Intra-orbital Coulomb repulsion.
V	Inter-orbital Coulomb repulsion.
$\chi(q, \omega)$	Dynamical susceptibility.
$\Delta(k)$	Superconducting order parameter.
$\Gamma(k, k')$	Effective pairing interaction.
ρ	Resistivity.
$\boldsymbol{\sigma}$	Pauli matrix.
$\sigma(\omega)$	Optical conductivity.

Chapter 1

Background on iron-based superconductors

As the title suggests, this thesis focuses on the so-called iron-based superconductors, which are a class of high-temperature superconducting materials discovered in 2008 [1]. Only four years have passed since their initial discovery. But great progress has been made and general consensus has been reached in this relatively young field. Interested readers may refer to many existing review articles [2, 3, 4, 5, 6] for a comprehensive understanding of the current research status of the iron-based superconductors.

Nonetheless, the author thinks it is necessary to provide his own perspective on this field, which will be the contents of this chapter. We will start with a short introduction to the general properties of the iron-based superconductors in Sec. 1.1. Particular emphasis will be put on the structural and the magnetic transitions, and their competition with the superconducting phase. Then we will move on to theoretical aspects in Sec. 1.2 and compare two distinct approaches for treating the iron-based superconductors, namely the weak-coupling and the strong-coupling theories. The local-itinerant model that combines both theories is also introduced.

1.1 Basic properties

The whole field of the iron-based superconductors started in February 2008, when Hideo Hosono and coworkers found that in layered iron-based materials LaOFeAs, superconductivity (SC) can be induced by replacing O with F, with the transition temperature T_c reaching as high as 26 K [1]. Following this seminal work, many new superconducting materials with the chemical composition of $RO_{1-x}F_xFeAs$ (R = Ce, Pr, Sm, Nd, etc.) [7, 8, 9, 10, 11] were discovered. In about two months, the superconducting transition temperature T_c was raised to around 55 K [11], which is only second to that of the copper-oxide superconductors (cuprates). In addition to the aforementioned materials with the 1111 chemical formula (the so-called 1111 family), new families of the iron-based superconductors were also discovered in a short time. They include $Ba_{1-x}K_xFe_2As_2$ [12, 13] (122 family), LiFeAs [14, 15] (111 family), $Fe_{1+y}Te_{1-x}Se_x$ [16] (11 family), and many others with more exotic compositions [17, 18].

The crystal structures of several representative iron-based superconductors

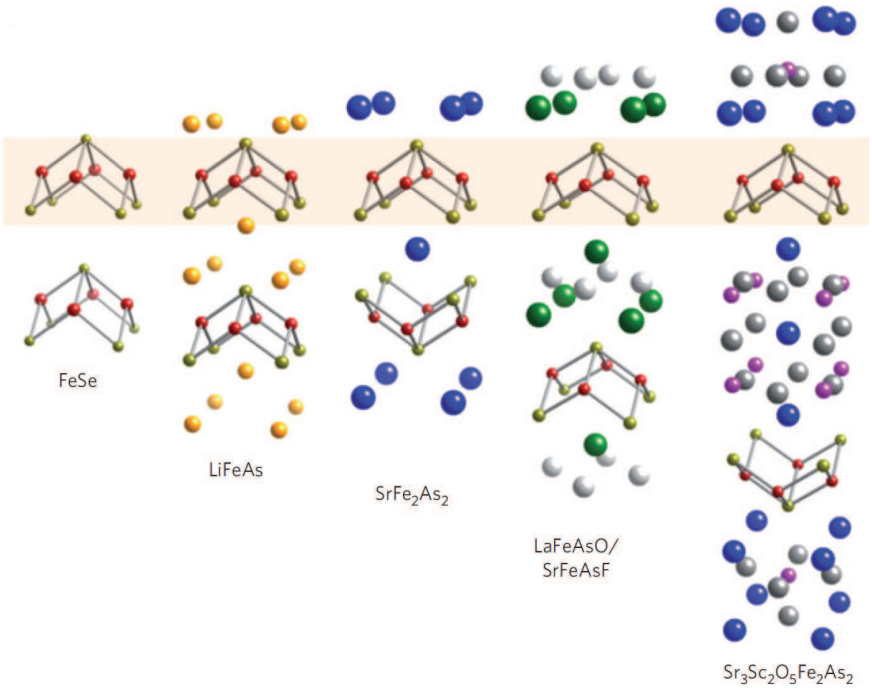

Figure 1.1: Crystal structures of several families of the iron-based superconductors. The quasi-two-dimensional tetrahedral coordinated FePn/Ch (Pn = P, As; Ch = Se, Te) plane is their common component. From Ref. [4].

are shown in Fig. 1.1. The common building blocks are FePn/Ch (Pn = P, As; Ch = Se, Te) planes sandwiched between different spacer layers, which either serve as the charge reservoir, or apply a chemical pressure to the FePn/Ch plane. The only exception is the $Fe_{1+y}Te_{1-x}Se_x$ system, in which the spacer layer does not exist and the FeCh planes simply stack together. It is generally accepted that high-temperature superconductivity and other interesting phenomena originate from this FePn/Ch plane, similar to the CuO plane in the cuprate superconductors. The materials with the FePn planes are named *iron pnictides*, while people call those with the FeCh layers *iron chalcogenides*.

As we see from Fig. 1.1, within the FeAs layer, the Fe atoms form a square lattice, whereas the As atoms are located at the center of each Fe square, sitting either above or below the Fe plane in an alternating order. Each Fe atom and its four neighboring As atoms form a tetrahedron structure, the geometry of which plays a critical role in mediating superconductivity. Due to the alternating position of the As atoms, the true crystal unit cell contains two Fe atoms. However, many theoretical models are constructed with the unit cell containing only one Fe atom. In Chapter 4, we will discuss in detail how these models can be constructed by unambiguously unfolding the 2-Fe Brillouin zone (BZ) into the 1-Fe BZ. The readers need to keep in mind this distinction when browsing existing literatures, some of which do not explicitly specify which conventions

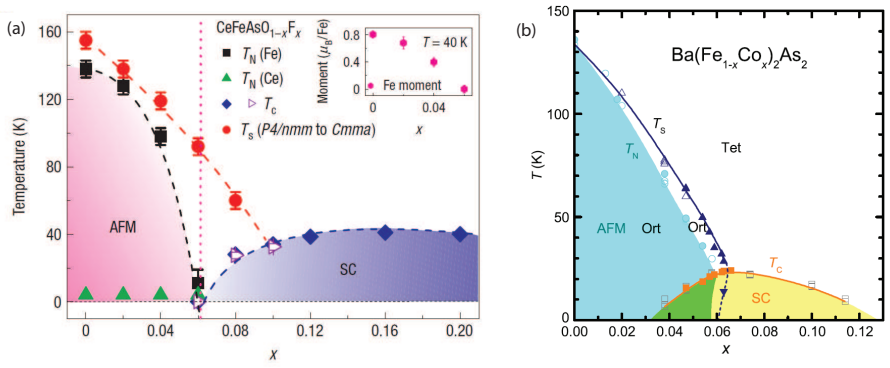

Figure 1.2: Temperature T versus composition x phase diagrams of the iron-based superconductors (a) $CeO_{1-x}F_xFeAs$ and (b) $Ba(Fe_{1-x}Co_x)_2As_2$. From Ref. [19] and [20].

are used.

Fig. 1.2 displays the phase diagrams of two typical iron-based superconductors, $CeO_{1-x}F_xFeAs$ (1111 family) [19] and $Ba(Fe_{1-x}Co_x)_2As_2$ (122 family) [20]. Similar to the cuprates, high-temperature superconductivity in the iron pnictides also arises from doping the antiferromagnetic (AFM) parent compounds. However, there are more important differences between the two. Unlike the cuprates, the parent compounds of the iron-based superconductors are metals instead of insulators. Simple chemical counting finds that Fe has a valence of 2+. So there are six electrons occupying the five outmost $3d$ orbitals, which clearly suggests that the iron-based superconductors are intrinsically multi-orbital systems. This is also different from the cuprates, in which all the $3d$ orbitals are doubly occupied except the half filled $d_{x^2-y^2}$ orbital.

In the iron-based superconductors, charge doping can be achieved, either by replacing O^{2-} with F^- in the charge reservoir layer in $CeO_{1-x}F_xFeAs$ [Fig. 1.2(a)], or by substituting Co^+ for Fe^{2+} directly in the FeAs plane in $Ba(Fe_{1-x}Co_x)_2As_2$ [Fig. 1.2(b)]. Both of these two are electron-doped materials. But similar T-x phase diagrams are also found in $Ba_{1-x}K_xFe_2As_2$ with hole doping and $BaFe_2(As_{1-x}P_x)_2$ with isovalent doping. Even applying pressure P, we still see a T-P phase diagram that is very similar in shape with the T-x phase diagram. We recall that in the cuprates, superconductivity can only be induced through charge doping in the reservoir layer.

Now let us set out to discuss each phase in the phase diagram. As illustrated in Fig. 1.2, the iron-based superconductors have a tetragonal crystal structure at high temperature. When the temperature decreases below the structural phase transition temperature T_S, a lattice distortion occurs in the parent compounds and the underdoped materials and reduces the crystal symmetry from tetragonal to orthorhombic. In the orthorhombic phase, the Fe-Fe lattice constant is elongated along one direction, and shortened along the other (Fig. 1.3). If we further lower the temperature below the Néel temperature T_N, a stripe-

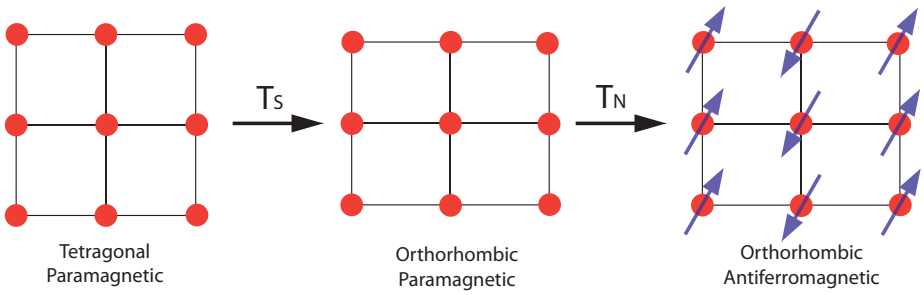

Figure 1.3: Illustration of the structural and the magnetic phase transitions in the iron-based superconductors. T_S and T_N are the structural phase transition temperature and the Néel temperature, respectively.

type long-range magnetic order sets in on the distorted Fe lattice. As shown in Fig. 1.3, the Fe spins are aligned antiferromagnetically along the longer direction and ferromagnetically along the shorter, characterized by the ordering wave vector $\boldsymbol{Q} = (\pi, 0)$. It should be noted that the ordered magnetic moment is very small, ranging from 0.3 μ_B in LaOFeAs [21] to around 0.8 μ_B in $BaFe_2As_2$ [22] and $CaFe_2As_2$ [23]. The $Fe_{1+y}Te$ system possesses a large moment around 2 μ_B, but its magnetic order is double-stripe type with $\boldsymbol{Q} = (\pi/2, \pi/2)$ [24, 25].

We should also note here that the structural and the magnetic transitions occur almost simultaneously, suggesting possible common origins. It has been found that in the 1111 family, the structural transition always occurs at a higher temperature than the magnetic one ($T_S > T_N$), with both transitions being second order. For the 122 family, this situation still holds for the electron-doped $Ba(Fe_{1-x}Co_x)_2As_2$ and the isovalent-doped $BaFe_2(As_{1-x}P_x)_2$. However, in the parent compounds and the hole-doped $Ba_{1-x}K_xFe_2As_2$, the structural and the magnetic transitions set in at the same temperature ($T_S = T_N$) and there is only one first-order transition. Recently, more detailed experiments have shown that in the parent compound $BaFe_2As_2$, these two transitions are actually separated by less than 1 K. The structural transition is still second order, whereas an apparent first-order discontinuity is seen at T_N [26, 27]. One important exception is the FeSe material, in which a structural transition happens at 90 K and there is no magnetic order down to zero temperature [28].

Understanding the structural and the magnetic transitions is a fundamental issue in the iron-based superconductors. One straightforward observation here is that the structural transition can occur in the absence of the magnetic order, but not vice versa. The reason is simply because the $(\pi, 0)$ AFM order breaks the lattice C_4 symmetry and has to be accompanied by the lattice distortion. This symmetry breaking naturally arises from the *orbital order* in a multi-orbital system, such as the iron-based superconductors. Orbital order is the central topic of the thesis. We will show in detail how the orbital order occurs and discuss its experimental consequences. In short, a ferro-orbital order of

the Fe d_{xz} and d_{yz} orbitals breaks the C_4 lattice symmetry and drives the structural transition from tetragonal to orthorhombic. Meanwhile, it enhances spin fluctuations along one particular direction, and leads to either a $(\pi, 0)$ or $(0, \pi)$ magnetic order.

Why are we so concerned with the structural and the magnetic transitions? Explaining their origin is certainly an interesting question in its own right. More importantly, their close relation with superconductivity may provide important clues for the pairing mechanism. From the phase diagram of $CeO_{1-x}F_xFeAs$ in Fig. 1.2(a), we see that superconductivity only emerges when the AFM order is completely suppressed, but is able to coexist with the orthorhombic distortion over some regime. However, in $Ba(Fe_{1-x}Co_x)_2As_2$ there is indeed a coexistent phase of superconductivity and the AFM order [Fig. 1.2(b)]. We would like to emphasize that T_c seems to be highest just when both the structural phase transition and the long-range AFM order are suppressed.

It is generally accepted that superconductivity in the iron-based superconductors does not come from conventional phonon-mediated pairing. The close proximity of the structural and the magnetic transitions to the superconducting phase gives us two different types of pairing mechanisms. The dominating viewpoint is that electron pairing arises from the spin-fluctuation exchange. This idea has a long history [29] and successfully predicted d-wave gap symmetry in cuprate superconductors (for a review, see Ref. [30]). When long-range AFM order is suppressed, spin fluctuations remain peaked at the original ordering wave vector $\boldsymbol{Q}$ and strongly scatter the Cooper pairs connected by $\boldsymbol{Q}$. This electron-electron interaction is always repulsive in the singlet channel, and thus requires a sign change of the superconducting order parameter,

$$\Delta(\boldsymbol{k}) = -\Delta(\boldsymbol{k} + \boldsymbol{Q}). \tag{1.1}$$

In the cuprates, $\boldsymbol{Q} = (\pi, \pi)$, leading to a d-wave superconducting gap. For the iron pnictides with $\boldsymbol{Q} = (\pi, 0)$, the extended s-wave (s_{+-}) gap will be favored [31]. To be more precise, the superconducting order parameter $\Delta(\boldsymbol{k})$ of the iron-based superconductors is invariant under $k_x \to k_y$ and $k_x \to -k_x$, and changes sign from $\boldsymbol{k}$ to $\boldsymbol{k} + \boldsymbol{Q}$. The other theory relies on the orbital order associated with the structural phase transition. When the lattice distortion is suppressed, enhanced orbital fluctuations can also mediate electron pairing and result in the conventional s_{++} gap without sign changes [32]. The majority of the community lean towards the s_{+-} symmetry, but the s_{++} pairing is not ruled out. Even within the s_{+-} framework, many issues are still unresolved. For example, a nodeless s_{+-} gap may develop nodes on the electron pockets when a third hole pocket composed of the d_{xy} orbital disappears with electron doping. Furthermore, even the d-wave symmetry will possibly emerge in the heavily electron- and hole-doped systems. We will discuss some of these issues in Sec. 1.2 in the context of the theoretical models of the iron-based superconductors. How-

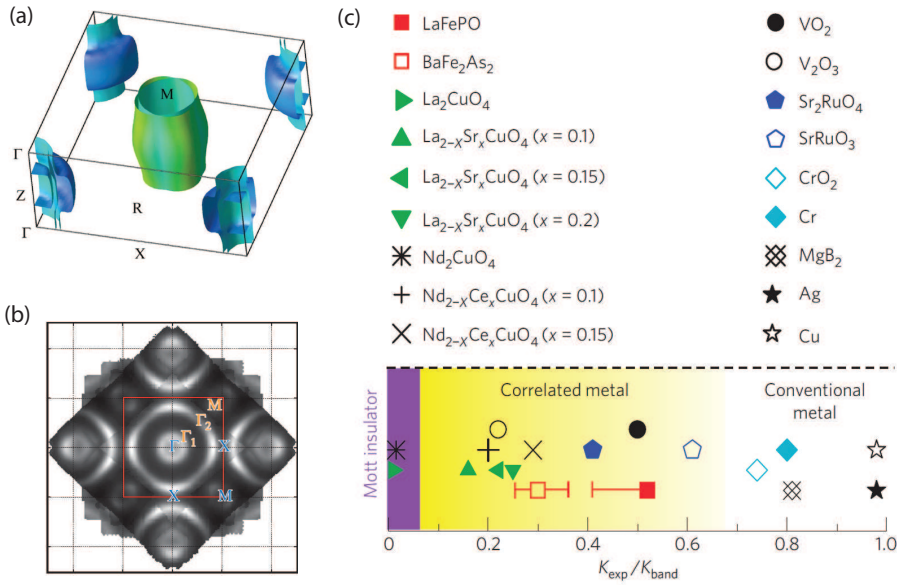

Figure 1.4: (a) Fermi surfaces in the 2-Fe BZ from LDA calculations. Here $\Gamma = (0, 0, 0)$, $Z = (0, 0, \pi)$, $X = (\pi, 0, 0)$, and $M = (\pi, \pi, 0)$. From Ref. [35]. (b) Fermi surfaces in the 2-Fe BZ from ARPES experiments. Γ_1 and Γ_2 denote the two hole pockets, while M represents the electron pockets. From Ref. [36]. (c) The ratio of the kinetic energy from the optical experiments and the kinetic energy from the band-structure calculations, $K_{\rm exp}/K_{\rm band}$, for the iron pnictides and other materials. From Ref. [37].

ever, detailed discussion about the gap symmetry and structure goes beyond the scope of this thesis. Interested readers are encouraged to consult some specific reviews [33, 34] on this issue.

1.2 Theoretical models

In this section, we will focus on the theoretical models. Because these models are also extensively used in explaining the anisotropic properties of the iron-based superconductors, which are the central themes of the thesis, it is necessary to give these models a brief introduction in advance.

Before we can construct any treatable theoretical models, there is one important question to answer. How strong is the electron correlation in the iron-based superconductors? Their metallic nature immediately tells us that the correlation effect is not as strong as in the cuprates, which are Mott insulators in their undoped state. Density functional theory (DFT) with the local density approximation (LDA) finds that the bands close to the chemical potential are mostly made up by the Fe $3d$ orbitals, and that the Fermi surfaces consist of multiple sheets [35]. As shown in Fig. 1.4(a), there are two hole cylinders around the zone center whereas two electron cylinders exist at the zone corner. A third three-dimensional hole pocket is also seen centered at the Z point. As shown

in Fig. 1.4(b), these fermi surfaces were qualitatively confirmed by the angle-resolve photoemission spectroscopy (ARPES) experiment [36]. But an overall renormalization of the band structure by a factor of 2-4 [36] needs to be imposed to match the band dispersion from LDA with that from ARPES, which suggests a nontrivial correlation effect.

More quantitative measurement of the electron correlations comes from optical conductivity experiments [37]. Such experiments extract the kinetic energy, K_{exp}, from the Drude weight. It is then compared to the kinetic energy from band-structure calculations, K_{band}. As we read from Fig. 1.4(c), the ratio $K_{\text{exp}}/K_{\text{band}}$ is close to one in conventional metals, such as Ag and Cu. In contrast, $K_{\text{exp}}/K_{\text{band}}$ almost vanishes in the parent compounds of the cuprates, La_2CuO_4 and Nd_2CuO_4. They are the prototypical Mott insulators in which the electron correlation effect dominates. Even in the doped cuprate materials, or say doped Mott insulators, a large reduction of the kinetic energy by 80% from its band-structure value is observed. This kinetic energy reduction is significantly less in weakly correlated materials. For example, MgB_2, which is a conventional phonon-mediated superconductor, and Cr, which is a spin-density-wave (SDW) antiferromagnet, only displays a reduction of 20%. In the iron pnictides, $K_{\text{exp}}/K_{\text{band}} \approx 0.3$ in $BaFe_2As_2$ and $K_{\text{exp}}/K_{\text{band}} \approx 0.5$ in LaFePO [Fig. 1.4(c)]. These values suggest that it is appropriate to categorize the iron-based superconductors as intermediately correlated metals. Another quantitative measurement is the x-ray absorption (XAS) and resonant inelastic x-ray scattering (RIXS) [38]. To obtain good agreement with theoretical calculations, it is required that the Coulomb repulsion be $U \approx 2eV$ and the Hund coupling be $J \approx 0.8eV$, which also places the iron pnictides in the regime of intermediate correlation.

As a result, both the weak-coupling and the strong-coupling theories are extensively used in the study of the iron-based superconductors. In addition, researchers have combined both aspects of weak and strong coupling and invented a hybrid model, namely the local-itinerant model. In the following we will discuss each of these theories, with emphasis on their advantages and limitations in the iron-based superconductors.

1.2.1 Weak coupling

In weak-coupling theories, because the interaction terms are treated as perturbations, band structure plays the dominant role. Therefore, the top priority is that our model can reproduce the Fermi surfaces and the band dispersions from the LDA calculations. We will write down a tight-binding Hamiltonian,

$$\mathcal{H}_K = \sum t_{ij}^{\alpha\beta} c_{i\alpha\mu}^{\dagger} c_{j\beta\mu}, \tag{1.2}$$

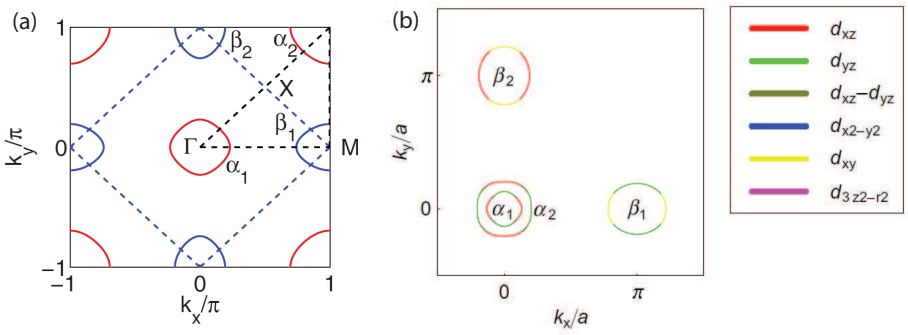

Figure 1.5: (a) Fermi surfaces of the two-orbital model in the 1-Fe BZ. The hole pockets are labeled as α_1 and α_2, whereas β_1 and β_2 are the electron pockets. The dashed square represents the true BZ with two Fe atoms per unit cell. From Ref. [41]. (b) Fermi surfaces of the five-orbital model in the 1-Fe BZ. The main orbital contribution is denoted by their corresponding colors. The filling level $n = 6$, corresponding to the parent compounds. From Ref. [47].

where $c^\dagger_{i\alpha\sigma}$ creates an electron on site i, with orbital α and spin μ. Although the As $4p$ orbitals are also included in some models [39], the majority of the theories only consider the Fe $3d$ orbitals, which dominate the bands near the Fermi energy according to the LDA calculations [35]. However, caution has to be taken when we transform $\mathcal{H}_K$ (1.2) into momentum space. The crystal momentum $\boldsymbol{k}$, defined by the translation operator $\boldsymbol{\mathcal{T}}$ of the Fe square lattice, is not a good quantum number of the system, because of the alternating positions of the As atoms. We have to enlarge our unit cell to contain two Fe atoms, and consequently double the number of the Fe $3d$ orbitals in our model. However, a more clever way is to define a pseudocrystal momentum $\tilde{\boldsymbol{k}}$ that labels the eigenstates of the operator $\mathcal{P}_z\boldsymbol{\mathcal{T}}$, where $\mathcal{P}_z$ is the reflection operator in the z direction. This pseudocrystal momentum $\tilde{\boldsymbol{k}}$ is a good quantum number of the system and gives an unambiguous way to unfold the 2-Fe BZ. We will be able to write down

$$\mathcal{H}_K = \sum \hat{\epsilon}_{\alpha\beta}(\tilde{\boldsymbol{k}}) c^\dagger_{\tilde{\boldsymbol{k}}\alpha\mu} c_{\tilde{\boldsymbol{k}}\beta\mu}. \tag{1.3}$$

Detailed discussion of this issue can be found in Ref. [40]. Due to the multi-orbital nature of the iron-based superconductors, at least two Fe $3d$ orbitals have to be included [41]. Some researchers even advocate that all five Fe $3d$ orbitals are necessary to reproduce a reasonable band structure. Interested readers may refer to the literatures for the available models, using two [41, 42, 43], three [40, 44], four [45], and five [46, 47, 48, 49, 50, 51] Fe $3d$ orbitals. As two examples, the Fermi surfaces of the two-orbital model [41] and the five-orbital model [47] are plotted in Fig. 1.5(a) and (b), respectively. For the five-orbital model, we denote the dominant orbital contributions on the Fermi surfaces by their corresponding colors in Fig. 1.5(b).

From Fig. 1.5(b), we see that the hole pockets at the zone center are connected to the two electron pockets at the zone edges approximately by the wave vector of $(\pi, 0)$ and $(0, \pi)$, respectively. This may induce a nesting instability in the system. Formally, we consider the dynamical spin susceptibility

$$\chi^s(q, q', i\omega) = \int_0^\beta \mathrm{d}\tau \langle T_\tau \boldsymbol{S}(q, \tau) \cdot \boldsymbol{S}(-q', 0)\rangle e^{i\omega\tau}, \tag{1.4}$$

and the dynamical charge susceptibility

$$\chi^c(q, q', i\omega) = \int_0^\beta \mathrm{d}\tau \langle T_\tau n(q, \tau) n(-q', 0)\rangle e^{i\omega\tau}. \tag{1.5}$$

We have defined the spin operator $\boldsymbol{S}(q, \tau) = 1/2 \sum c^\dagger_{k+q,\mu}(\tau)\boldsymbol{\sigma}_{\mu\nu} c_{k,\nu}(\tau)$ and the charge operator $n(q, \tau) = \sum c^\dagger_{k+q,\mu}(\tau)\delta_{\mu\nu} c_{k,\nu}(\tau)$, where $\boldsymbol{\sigma}$ is the Pauli matrix. For the normal state without translational symmetry breaking, the susceptibility χ is diagonal, namely only $\chi(q, q, i\omega)$ with $q = q'$ is nonzero. The noninteracting χ^s_0 and χ^c_0 are equivalent. They can be easily calculated after a unitary transformation that diagonalizes $\mathcal{H}_K$ (1.3).

Now we include the electron interactions. The simplest one is the on-site Hubbard interaction. For a multi-orbital system, it reads [52]

$$\begin{aligned} \mathcal{H}_I &= \sum_\alpha U \hat{n}_{\alpha\uparrow}\hat{n}_{\alpha\downarrow} + \sum_{\beta>\alpha}\left(V - \frac{J}{2}\right)\hat{n}_\alpha \hat{n}_\beta - \sum_{\beta>\alpha} 2J\boldsymbol{S}_\alpha \cdot \boldsymbol{S}_\beta \\ &\quad + \sum_{\beta>\alpha} J'\left(c^\dagger_{\alpha\uparrow} c^\dagger_{\alpha\downarrow} c_{\beta\downarrow} c_{\beta\uparrow} + h.c.\right), \end{aligned} \tag{1.6}$$

where U, V, J, and J' are intra- and inter-orbital Coulomb repulsion, Hund's coupling, and the pairing hopping energy, respectively. Note that the site index i has been suppressed here. If we impose that all the orbitals are degenerate and equivalent, it is required that $U = V + 2J$ and $J = J'$. However, this symmetry requirement is not usually fulfilled in real systems.

The effect of these interactions on χ^s and χ^c can be calculated using the random phase approximation (RPA). The detailed formulation for a multi-orbital system can be found in Ref. [47], [50] and [54]. As shown in Fig. 1.5(b), the RPA spin susceptibility χ^s_{RPA} displays enhanced peaks at the wave vectors close to $(\pi, 0)$ and $(0, \pi)$, due to the nesting between the hole and electron pockets. A broad feature is also found near (π, π), which arises from the scattering between the two electron pockets. In contrast, the RPA charge susceptibility χ^c_{RPA} is more than one order of magnitude smaller than χ^s_{RPA}, and shows no sharp peaks. Therefore, when we increase the interaction strength, χ^s_{RPA} will first diverge at some critical value of the interaction strength and causes a spin-density-wave (SDW) order with either $\boldsymbol{Q} = (\pi, 0)$ or $(0, \pi)$. From the viewpoint of the weak-coupling theories, the antiferromagnetic order in iron-based superconductors comes from the nesting instability between the hole and electron

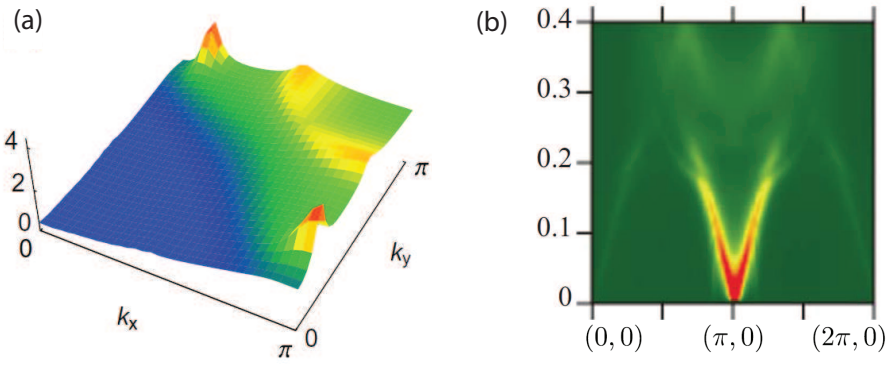

Figure 1.6: (a) RPA spin susceptibility $\chi^s_{\rm RPA}(q,\omega=0)$ for the paramagnetic phase. $\chi^s_{\rm RPA}$ peaks close to the ordering wave vector $\boldsymbol{Q}=(\pi,0)$ and $(0,\pi)$. The calculation is done for the electron-doped system with $n=6.125$, and interaction parameters are $U=V=1.65$, $J=J'=0$. From Ref. [47]. (b) The imaginary part of the RPA spin susceptibility, $\Im\chi^s_{\rm RPA}(q,\omega+i\delta)$, for the antiferromagnetic phase with the ordering wave vector $\boldsymbol{Q}=(\pi,0)$. The ordered magnetic moment $m=0.6\,\mu_B$. From Ref. [53].

Fermi surfaces.

The magnetically ordered state can be investigated using a self-consistent mean-field approach. The interaction term is decoupled in an orbital diagonal way,

$$\left\langle c^\dagger_{i\alpha\mu}c_{i\beta\nu}\right\rangle = \frac{1}{2}\left(n_\alpha+\mu m_\alpha e^{i\boldsymbol{Q}\cdot\boldsymbol{r}_i}\right)\delta_{\alpha\beta}\delta_{\mu\nu}, \tag{1.7}$$

where $\mu=\pm1$ for up and down spins, respectively. We derive the mean-field interaction term,

$$\mathcal{H}^{MF}_I = \sum_{\boldsymbol{k},\alpha,\mu}\left[\epsilon_\alpha c^\dagger_{\boldsymbol{k}\alpha\mu}c_{\boldsymbol{k}\alpha\mu}-\mu\eta_\alpha\left(c^\dagger_{\boldsymbol{k}\alpha\mu}c_{\boldsymbol{k}+\boldsymbol{Q},\alpha\mu}+h.c\right)\right]+C, \tag{1.8}$$

where

$$\epsilon_\alpha = \frac{U}{2}n_\alpha+\left(V-\frac{J}{2}\right)\sum_{\beta\neq\alpha}n_\beta, \tag{1.9}$$

$$\eta_\alpha = \frac{U}{2}m_\alpha+\frac{J}{2}\sum_{\beta\neq\alpha}m_\beta, \tag{1.10}$$

and the constant

$$C = -\frac{U}{4}\sum_\alpha\left(n_\alpha^2-m_\alpha^2\right)-\frac{2V-J}{4}\sum_{\alpha\neq\beta}n_\alpha n_\beta+\frac{J}{4}\sum_{\alpha\neq\beta}m_\alpha m_\beta. \tag{1.11}$$

The full Hamiltonian $\mathcal{H}=\mathcal{H}_K+\mathcal{H}^{MF}_I$ is quadratic, and thus can be solved with the order parameters n_α and m_α being calculated self-consistently. As many studies have shown, the $\boldsymbol{Q}=(\pi,0)$ stripe-type AFM order indeed has the lowest

energy if the interaction parameters are chosen properly [44, 45, 51].

We can further calculate the spin excitations in the AFM-ordered state using the random phase approximation. However, we should note that both $\chi(q, q, i\omega)$ and $\chi(q, q + Q, i\omega)$ become nonzero due to the presence of the AFM order. Detailed formulations can be found in Ref. [55] and [56] for the single-band case, and Ref. [53] for the multi-orbital generalization. The result from the five-orbital model is shown in Fig. 1.6(b). The excitation clearly exhibits the collective mode of spin waves around the ordering wave vector $(\pi, 0)$, and quickly dissolves into the particle-hole continuum at high energy.

The most powerful prediction of the weak-coupling theories is the symmetry and structure of the superconducting order parameters. Within the RPA formalism, the superconducting gap equation is reduced to the following eigenvalue problem [47, 57],

$$-\sum_j \oint_{C_j} \frac{\mathrm{d}k'}{2\pi} \frac{1}{v_F(k')} \Gamma_{ij}(k, k') g_\alpha(k') = \lambda_\alpha g_\alpha(k), \tag{1.12}$$

where $v_F(k)$ is the Fermi velocity. We have decomposed the superconducting order parameter $\Delta(k)$ into the amplitude Δ and the normalized structure function $g(k)$, $\Delta(k) = \Delta g(k)$. The effective pairing interaction $\Gamma_{ij}(k, k')$ scatters the Cooper pair at $(k, -k)$ on the Fermi surface C_i to $(k', -k')$ on the Fermi surface C_j. The solution with the largest eigenvalue λ_α is the leading pairing instability and has the highest transition temperature T_c. The eigenfunction $g_\alpha(k)$ determines the superconducting gap symmetry and structure.

As we see from Fig. 1.7(a), the effective pairing interaction $\Gamma(k, k', i\omega)$ quickly decays when we increase the energy scale. So the gap equations can be restricted on the Fermi surfaces as we have done in Eq. (1.12). We also find that $\Gamma(k, k', i\omega)$ mostly comes from the spin fluctuation contributions, and thus also peaks when $k - k' = Q$. Because $\Gamma(k, k')$ is positive, a sign change has to occur between $g(k)$ and $g(k + Q)$ so that a nontrivial solution to Eq. (1.12) can be found. Meanwhile, $g(k)$ is invariant under the reflection $x \to -x$ and $y \to -y$, and the C_4 rotation $x \to y$ and $y \to -x$. This is the so-called extended s-wave gap or s_{+-} gap in the literature [31]. As shown by Fig. 1.7(b) and (c), the superconducting gap does have different signs between the hole and electron pockets. However, there exists a competing order that arises from the (π, π) scattering between the two electron pockets. This scattering process disfavors the isotropic s_{+-} gap, and induces anisotropy and possibly gap nodes on the electron pockets [see Fig. 1.7(b)]. If we dope the materials with holes, a third hole pocket, which is dominated by the d_{xy} orbital, appears at (π, π). The presence of this hole pocket will enhance the scattering between the hole and electron pockets, and thus stabilize an isotropic s_{+-} gap without nodes [see Fig. 1.7(c)]. Actually the emergence of the third hole pocket at (π, π) is also related to the pnictogen height [58], which can be tuned either by applying external pressure, or by

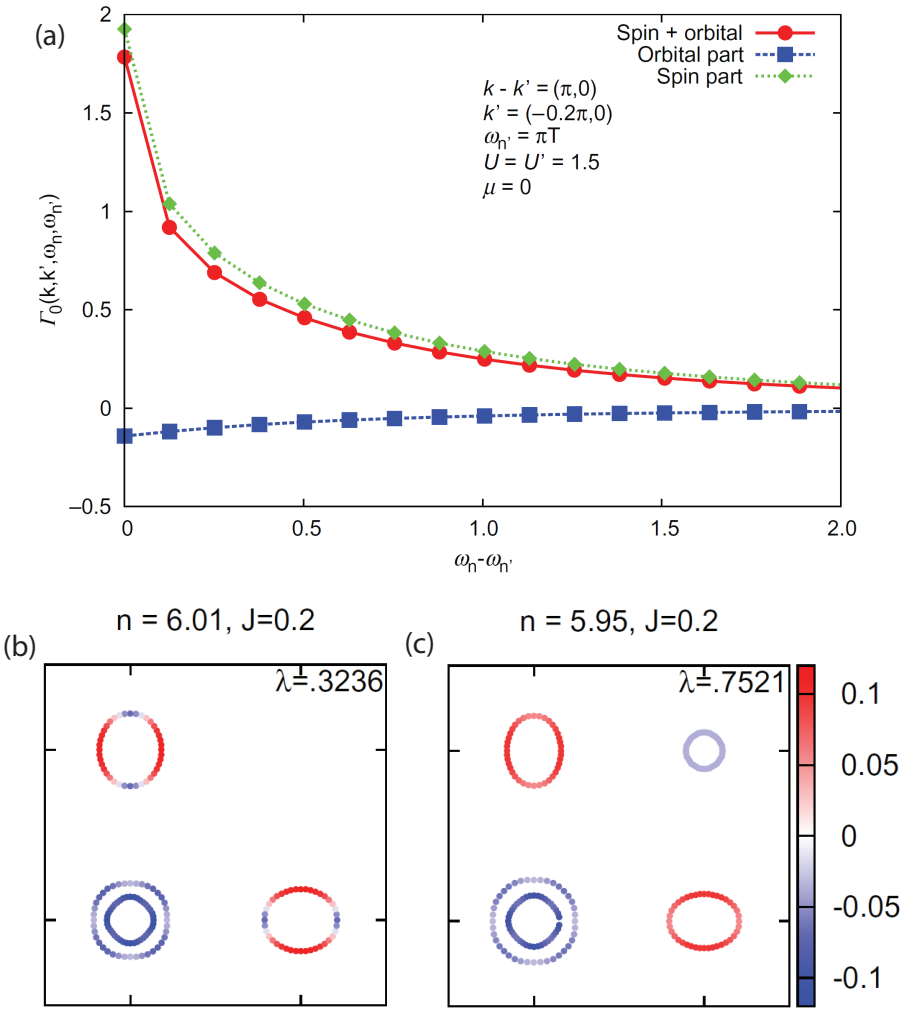

Figure 1.7: (a) The effective pairing interaction $\Gamma(k, k', \omega, \omega')$, and its spin and orbital contributions. From Ref. [47]. (b) The superconducting gap structure function $g(k)$ for the electron doping of $n = 6.01$. (c) $g(k)$ for the hole doping of $n = 5.95$. From Ref. [57].

replacing the As with the P atoms in $BaFe_2(As_{1-x}P_x)_2$.

So far, the s_{+-} gap is the leading candidate in the iron-based superconductors. Experimentally the superconducting gap observed in ARPES is nearly isotropic and nodeless [59]. On the other hand, the superconducting quantum interference device (SQUID) measurement detected a half-integer flux quantum jump [60], which strongly suggests that a π phase shift or a sign change occurs in the superconducting order parameters. Further support of the sign change comes from the appearance of the neutron resonance peak at $(\pi, 0)$ [61]. The quasiparticle interference (QPI) image measured by the scanning tunneling microscopy (STM) experiment provides another phase sensitive evidence [62].

However, recent studies have found that different iron-based superconductors may possess different pairing symmetries. For example, in heavily hole-doped

material KFe_2As_2, a nodal d-wave gap is likely to win over [63]. The nodeless d-wave superconductivity is the favorite candidate for KFe_2Se_2 [64], in which the hole pockets are absent [65]. It is a very interesting problem to see how different pairing channels compete with each other when we dope the system or modify the crystal structure of the FeAs layer. In the end, we briefly comment that the conventional s_{++} gap is also possible if the pairing interaction $\Gamma(k, k')$ becomes attractive when the orbital fluctuations make the dominant contributions [32]. The current theoretical and experimental status is summarized by several review articles [33, 34].

There are more advanced approaches that go beyond RPA. The most popular one is the functional renormalization group (FRG) [66], which was pioneered in the context of the iron-based superconductors in Ref. [67]. This technique is able to study the flow of the renormalized interactions when the energy cutoff Λ is reduced, and thus treats different instabilities on an equal footing. Although the FRG is much more unbiased than RPA, it is still a weak-coupling theory due to its perturbative nature. FRG is highly successful in the study of the iron-based superconductors. It confirms that the $(\pi, 0)$ SDW order and the s_{+-} superconductivity are the two leading instabilities of the system [68]. Researchers have applied the FRG approach to many different iron-based superconductors [69, 70, 71], and their results appear to be consistent with those from the RPA calculations.

The theories we have discussed so far are all formulated on the orbital basis. But some researchers prefer the so-called multi-band model [72],

$$H_K = \sum_{\boldsymbol{k}\mu} \epsilon_{h,\boldsymbol{k}} c^\dagger_{\boldsymbol{k}\mu} c_{\boldsymbol{k}\mu} + \epsilon_{e,\boldsymbol{k}+\boldsymbol{Q}} d^\dagger_{\boldsymbol{k}+\boldsymbol{Q},\mu} d_{\boldsymbol{k}+\boldsymbol{Q},\mu}, \tag{1.13}$$

where $c_{\boldsymbol{k}\mu}$ and $d_{\boldsymbol{k}+\boldsymbol{Q},\mu}$ are the annihilation operators on the hole and the electron bands, respectively. The hole pocket at $\Gamma = (0, 0)$ is circular, with the dispersion

$$\epsilon_{h,\boldsymbol{k}} = \epsilon_{h,0} - \frac{k_x^2 + k_y^2}{2m} - \mu, \tag{1.14}$$

whereas the electron pockets are elliptical with

$$\epsilon^{X,Y}_{e,\boldsymbol{k}+\boldsymbol{Q}} = -\epsilon_{e,0} + \frac{k_x^2}{2m_{x,y}} + \frac{k_y^2}{2m_{y,x}} - \mu. \tag{1.15}$$

Here we use the the unfolded Brillouin zone that contains one Fe atom per unit cell. So there are two electron pockets located at $X = (\pi, 0)$ and $Y = (0, \pi)$, with their dispersions $\epsilon^X_{e,\boldsymbol{k}+\boldsymbol{Q}}$ and $\epsilon^Y_{e,\boldsymbol{k}+\boldsymbol{Q}}$, respectively. We will choose $m_x > m_y$ so that the electron pockets are elongated along the correct direction.

The main advantage of this model is that the physical meaning is very evident. We can write down the magnetic interaction term,

$$\mathcal{H}_{\mathrm{AFM}} = V_{\mathrm{AFM}} \sum c^\dagger_{\boldsymbol{k}\mu} \boldsymbol{\sigma}_{\mu\nu} d_{\boldsymbol{k}+\boldsymbol{Q},\nu} \cdot d^\dagger_{\boldsymbol{k}'+\boldsymbol{Q},\mu'} \boldsymbol{\sigma}_{\mu'\nu'} c_{\boldsymbol{k}'\nu'}. \tag{1.16}$$

Without loss of generality, we choose the spin quantization axis along the direction of the magnetization. The spin-density-wave (SDW) gap is simply

$$\Delta_{\rm SDW} = \frac{V_{\rm AFM}}{2} \sum \mu \langle c^\dagger_{\boldsymbol{k}\mu} d_{\boldsymbol{k}+\boldsymbol{Q},\mu} \rangle. \tag{1.17}$$

Similarly, the inter-band pairing interaction in the singlet channel is

$$\mathcal{H}_{\rm SC} = V_{\rm SC} \sum \left(c^\dagger_{-\boldsymbol{k}\downarrow} c^\dagger_{\boldsymbol{k}\uparrow} d_{\boldsymbol{k}'+\boldsymbol{Q},\uparrow} d_{-\boldsymbol{k}'-\boldsymbol{Q},\downarrow} + h.c. \right). \tag{1.18}$$

The superconducting gaps on the hole and electron pockets are

$$\Delta_{h,\rm SC} = V_{\rm SC} \sum \langle d_{\boldsymbol{k}+\boldsymbol{Q},\uparrow} d_{-\boldsymbol{k}-\boldsymbol{Q},\downarrow} \rangle, \tag{1.19}$$

$$\Delta_{e,\rm SC} = V_{\rm SC} \sum \langle c_{\boldsymbol{k}\uparrow} c_{-\boldsymbol{k}\downarrow} \rangle, \tag{1.20}$$

respectively. We see that due to the inter-band nature of the pairing interaction, the superconducting gap on the hole pocket is determined by the electrons on the electron pocket, and vice versa. This formulation turns out to be very useful in studying competing orders, for example, the coexisting phase of the AFM order and superconductivity [73, 74, 75, 76, 77]. To zeroth order, the multi-band model is equivalent to the multi-orbital model. However, in order to study the angular dependence, we have to project the multi-orbital model onto the band basis and decompose the interaction with the leading angular harmonics [78, 79]. Therefore, the multi-orbital model is more fundamental from our point of view.

Finally, let us focus on several limitations of the weak-coupling theories. First, the nesting between the hole and electron pockets is far from perfect. Both the LDA calculations and the ARPES experiments have found that the hole pockets possess more circular shapes, whereas the electron pockets are more elliptical. Therefore, the nesting instability does not usually occur at the commensurate ordering wave vectors $\boldsymbol{Q} = (\pi, 0)$ and $(0, \pi)$, but instead at some incommensurate wave vectors [see Fig. 1.6(a)]. So the AFM order from the weak-coupling theories should be incommensurate. But neutron scattering experiments almost always observe commensurate AFM order [21]. Second, weak-coupling theories cannot explain the so-called bicollinear AFM order with $\boldsymbol{Q} = (\pi/2, \pi/2)$ in the $Fe_{1+y}Te$ materials [24, 25]. The Fermi surfaces of $Fe_{1+y}Te$ are very similar in shape with those of the iron pnictides, as the ARPES experiments have found [80]. So there is no nesting instability at $\boldsymbol{Q} = (\pi/2, \pi/2)$. Additionally, the large magnetic moment observed in $Fe_{1+y}Te$ cannot arise from weak-coupling theories. Third, as we will discuss in detail in Sec. 2.1.1, the spin excitations derived from inelastic neutron scattering (INS) experiments are better fitted by a Heisenberg model. The predicted particle-hole continuum from the weak-coupling theories is not observed in several materials [81]. Finally, ARPES almost always observed a nearly isotropic superconducting gap [59] in-

stead of the strong angular variation from the weak-coupling calculations. More recently, laser ARPES experiments found that the superconducting gap is orbital independent [82], which is not consistent with the prediction from the spin fluctuation scenario.

1.2.2 Strong coupling

Although most of the iron-based superconductors are metallic, the electron correlation is certainly not weak as manifested by the unusually high resistivity. Early dynamical mean-field theory (DMFT) combined with DFT calculations suggested that the iron pnictides are strongly correlated metals on the verge of a Mott transition [83]. On the basis of this motivation, the strong-coupling theories were put forward.

In these models, the Fe orbitals are localized due to strong electron correlations, and the virtual hopping processes give rise to the antiferromagnetic superexchanges between the local moments $\boldsymbol{S}_i$. Because the As atoms are located at the center of the Fe square, the next-nearest-neighbor (NNN) hopping may acquire similar amplitude as the nearest-neighbor (NN) hopping. Immediately, we can write down the following Heisenberg model [84],

$$\mathcal{H}_{\rm loc} = J_1 \sum_{\langle i,j \rangle} \boldsymbol{S}_i \cdot \boldsymbol{S}_j + J_2 \sum_{\langle\langle i,j \rangle\rangle} \boldsymbol{S}_i \cdot \boldsymbol{S}_j, \tag{1.21}$$

where J_1 and J_2 are the NN and NNN superexchanges, respectively. If we treat the spin $\boldsymbol{S}_i$ as a classical vector, then the $(\pi, 0)$ or $(0, \pi)$ stripe-type AFM order has the lowest energy when $J_2 > J_1/2$, whereas the (π, π) order becomes the ground state when $J_2 < J_1/2$. It is certainly difficult to calculate the exact values of the exchange constants. However, if we simply assume the hopping amplitude mediated by the As atoms is independent of the Fe-As-Fe angle, we obtain $J_2 = J_1/2$. There are two paths via different As atoms for the NN Fe atoms, whereas only one path connects the NNN Fe atoms. So the iron-based superconductors are probably in the strongly frustrated regime with $J_2 \gtrsim J_1/2$, which explains the unusually small moments observed experimentally [21].

In the magnetically ordered state with $\boldsymbol{Q} = (\pi, 0)$, the spin excitations can be readily calculated by the standard linear spin-wave theory [85, 87]. The spin $\boldsymbol{S}_i$ is represented by the Holstein-Primakoff boson a_i,

$$S_i^z = S - a_i^\dagger a_i, \quad S_i^+ = \sqrt{2S - a_i^\dagger a_i}\, a_i, \quad S_i^- = a_i^\dagger \sqrt{2S - a_i^\dagger a_i}, \tag{1.22}$$

where $S_i^\pm = S_i^x \pm i S_i^y$. To the leading order, the spin-wave Hamiltonian reads

$$\mathcal{H}_{\rm loc}^{\rm sw} = \sum_k \left[A(k) \left(a_k^\dagger a_k + a_{-k} a_{-k}^\dagger \right) + B(k) \left(a_k^\dagger a_{-k}^\dagger + a_{-k} a_k \right) \right], \tag{1.23}$$

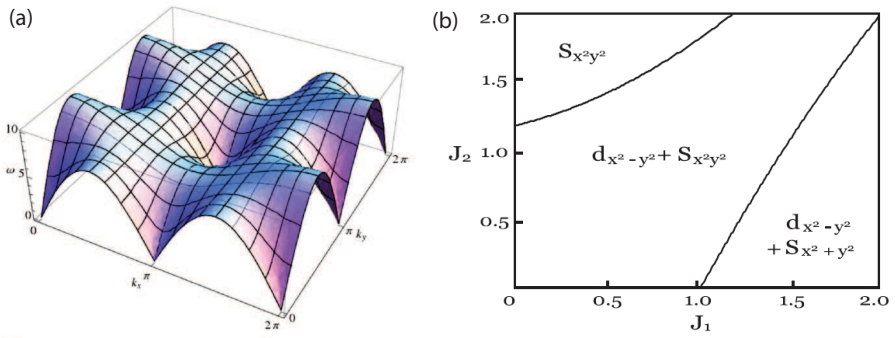

Figure 1.8: (a) Spin-wave dispersions from the J_1-J_2 model. We have set $J_1 = 1$ and $J_2 = 2$. From Ref. [85]. (b) Superconducting phase diagram of the t-J_1-J_2 model. The two-orbital model of Ref. [41] is used for the band structure. From Ref. [86].

where

$$A(k) = S(J_1 \cos k_y + 2J_2), \quad B(k) = S(J_1 \cos k_x + 2J_2 \cos k_x \cos k_y). \quad (1.24)$$

We use the Bogoliubov transformation to diagonalize $\mathcal{H}^{\rm sw}_{\rm loc}$ (1.23), yielding the spin-wave dispersion

$$\omega(k) = \sqrt{A^2(k) - B^2(k)}. \quad (1.25)$$

One immediate consequence of the spin-wave calculation is that the dispersion $\omega(k)$ is zero, not only at the ordering wave vector $\boldsymbol{Q} = (\pi, 0)$, but also at (π, π) [see Fig. 1.8(a)]. Although single-ion anisotropy and quantum fluctuations can lift this zero at (π, π), the spin-wave energy still remains a local minimum at (π, π). However, as we will see in detail in Sec. 2.1.1, the inelastic neutron scattering experiments found out that the spin-wave dispersion actually reaches a local maximum at (π, π) [81]. This contradiction causes much controversy about the strong-coupling J_1-J_2 model.

Nevertheless, let us turn to the problem of superconductivity. We consider the superexchange between the spin of orbital α at site i and the spin of orbital β at site j,

$$\mathcal{H}^{\alpha\beta}_{ij} = J^{\alpha\beta}_{ij} \left(\boldsymbol{S}_{i\alpha} \cdot \boldsymbol{S}_{j\beta} - \frac{1}{4} n_{i\alpha} n_{j\beta} \right) = -\frac{1}{2} J^{\alpha\beta}_{ij} \left(B^{\alpha\beta}_{ij} \right)^\dagger B^{\alpha\beta}_{ij}, \quad (1.26)$$

where the spin-singlet pairing operator $B^{\alpha\beta}_{ij}$ is defined as

$$B^{\alpha\beta}_{ij} = c_{i\alpha\uparrow} c_{j\beta\downarrow} - c_{i\alpha\downarrow} c_{j\beta\uparrow}. \quad (1.27)$$

It is clear that the superexchange J provides the necessary pairing interaction between the neighboring sites i and j. The treatment of the single-band problem

can be found in Ref. [88] and [89]. For the multi-orbital case, it is argued that the dominant pairing channel is from the intra-orbital exchanges [86, 90]. So the inter-orbital exchanges are neglected, $J_{ij}^{\alpha\beta} = \delta_{\alpha\beta} J_{ij}^{\alpha}$. We will further assume that for different orbitals, J_{ij}^{α} takes the same value of J_1 and J_2 between the NNs and NNNs. With the presence of the translational symmetry, we can identify four distinct pairing amplitudes, $\Delta_x^\alpha = \langle B_{i,i+x}^{\alpha\alpha} \rangle$, $\Delta_y^\alpha = \langle B_{i,i+y}^{\alpha\alpha} \rangle$, $\Delta_{x+y}^\alpha = \langle B_{i,i+x+y}^{\alpha\alpha} \rangle$, and $\Delta_{x-y}^\alpha = \langle B_{i,i+x-y}^{\alpha\alpha} \rangle$.

Without the kinetic energy, the pairing states are highly degenerate. For example, in a system with only the NN exchange J_1, we can have the $s_{x^2+y^2}$ pairing with the structure factor $g_{x^2+y^2} = \cos k_x + \cos k_y$ when $\Delta_x = \Delta_y$. In contrast, $\Delta_x = -\Delta_y$ will produce a degenerate $d_{x^2-y^2}$ pairing state with $g_{x^2-y^2} = \cos k_x - \cos k_y$. Similarly, if J_2 is the dominant energy scale, there also exist two degenerate pairing states $s_{x^2y^2}$ and d_{xy}, with the structure function $g_{x^2y^2} = \cos k_x \cos k_y$ and $g_{xy} = \sin k_x \sin k_y$. In real space, they correspond to $\Delta_{x+y} = \Delta_{x-y}$ and $\Delta_{x+y} = -\Delta_{x-y}$, respectively.

The inclusion of the kinetic energy will lift the degeneracy of the pairing states. Basically we will decouple the magnetic exchange term in the particle-particle channel, and the resulting quadratic t-J_1-J_2 Hamiltonian can be solved by a self-consistent mean-field theory. The solution that has the lowest energy is the ground state and determines the leading paring instability of the system. Various multi-orbital models have been used to capture the kinetic energy of the iron-based superconductors [86, 90, 91, 92].

In Fig. 1.8(b), we show the superconducting phase diagram of a two-orbital model at electron doping $x = 0.18$ [86]. As expected, when J_2 dominates, the $s_{x^2y^2}$ state is the leading pairing instability. Its structural factor $g_{x^2y^2} = \cos k_x \cos k_y$ changes sign from the hole pockets at $(0, 0)$ to the electron pockets at $(\pi, 0)$ and $(0, \pi)$. It is consistent with the prediction from the weak-coupling approaches. In contrast, for the J_1-dominated regime, we will favor the $d_{x^2-y^2}$ state [90] with $g_{x^2-y^2} = \cos k_x - \cos k_y$, which produces nodes at the hole pockets and changes sign between the two electron pockets. Very interestingly, there is a mixed state of $s_{x^2y^2}$ and $d_{x^2-y^2}$ pairing in the intermediate regime [see Fig. 1.8(b)], signaling the competition of J_1 and J_2. In this mixed phase, the $d_{x^2-y^2}$ order parameter changes sign between the d_{xz} and d_{yz} orbitals, whereas the order parameter of $s_{x^2y^2}$ is invariant. So the overall superconducting state still has the s-wave symmetry. The detailed discussion regarding the pairing symmetry for the two-orbital case can be found in Ref. [93]. Compared to the weak-coupling results, this mixed pairing state gives rise to the angular dependence of the superconducting order parameters from another perspective. However, due to the dominance of the NNN exchange J_2, the $s_{x^2y^2}$ gap is usually favored in the strong-coupling theories. For example in KFe_2Se_2 where the hole pocket is absent, the weak-coupling theories predict a d-wave gap [64, 69], while the t-J_1-J_2 models still lead to the $s_{x^2y^2}$ gap [91, 92].

The most apparent difficulty of the strong coupling theories is that the iron-

based superconductors are never insulators, even for the parent compounds. We are unable to justify that the low-energy spin physics can be described by a Heisenberg model. Second, because the J_1-J_2 exchange interaction governs the spin fluctuations, the superconducting gap structure becomes fixed in momentum space. The sign and amplitude of the superconducting order parameter only depend on the position of the Fermi surface. This result is not supported by the experimental observations and the weak-coupling calculations. Finally, as we have mentioned and will discuss in detail in Sec. 2.1.1, later inelastic neutron scattering experiments [81] found that the isotropic J_1-J_2 Heisenberg model cannot capture the observed spin excitations. The fitted exchange constants are highly anisotropic, with $J_{1a} \gg J_{1b}$, for the $(\pi, 0)$ magnetically ordered state. We will see later that this anisotropy of the magnetic exchanges comes naturally from the so-called Kugel-Khomskii model [94], which includes both the spin and the orbital degrees of freedom.

1.2.3 Hybrid model

Motivated by the fact that neither the weak-coupling nor the strong-coupling theories give a satisfactory description of the iron-based superconductors, some have proposed the hybrid model that combines both theories. In this so-called local-itinerant model, some d electrons become effectively localized and form the local moments, whereas some other d electrons remain itinerant, contributing to the observed metallic properties. The simultaneous presence of both localized and itinerant electrons was proposed in the early study to explain the unusually small magnetic moments [95]. However, more precise formulations of the hybrid model came later [96, 97].

As illustrated by Fig. 1.9, the full Hamiltonian consists of three parts,

$$\mathcal{H} = \mathcal{H}_{\rm loc} + \mathcal{H}_K + \mathcal{H}_{\rm H}, \tag{1.28}$$

where $\mathcal{H}_{\rm loc}$, $\mathcal{H}_K$, and $\mathcal{H}_{\rm H}$ describe the local moments, the itinerant electrons, and the couplings between the two, respectively. The local moments arise from strong electron correlations. They are the incoherent excitations away from the Fermi energy (Fig. 1.9). Recall that in the iron pnictides, the electron interaction strength is likely to sit just below the critical value to induce a Mott transition [83, 84]. These incoherent excitations are the remnants of the upper and lower Hubbard bands in a Mott insulator, although a Mott gap does not fully develop here. For simplicity, we will assume that the local moments are governed by the superexchanges J_1 and J_2 between the nearest neighbors and the next-nearest neighbors. So $\mathcal{H}_{\rm loc}$ takes the form of the J_1-J_2 Heisenberg model, as in Eq. (1.21). The itinerant electrons are the coherent excitations at the Fermi energy (Fig. 1.9). They are adiabatically connected to the noninteracting quasiparticles. So the interaction term within the itinerant electrons can be legally dropped. We use either a multi-orbital model $\mathcal{H}_K$ (1.2) or a

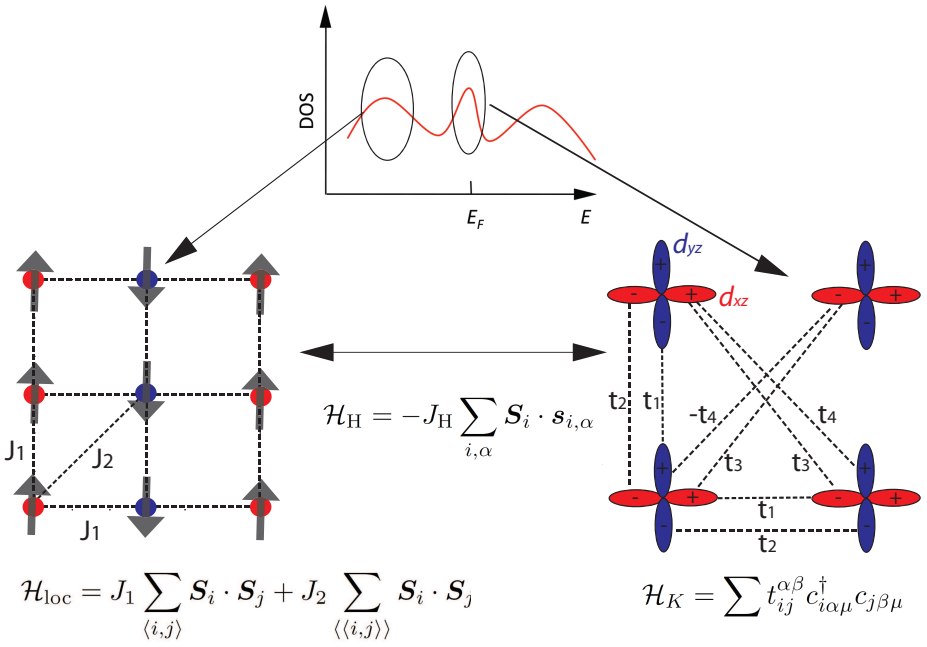

Figure 1.9: Illustration of the local-itinerant model. The local moments are described the J_1-J_2 Heisenberg model. We use a multi-orbital tight-binding Hamiltonian for the part of the itinerant electrons. The two are further coupled by a ferromagnetic Hund exchange. The illustration of the density of states is from Ref. [96].

multi-band model $\mathcal{H}_K$ (1.13) to reproduce the Fermi surfaces. As an example, Fig. 1.9 displays a two-orbital tight-binding model consisting of the d_{xz} and d_{yz} orbitals. Finally, we need to introduce the on-site Hund couplings between the local moments and the itinerant electrons.

$$\mathcal{H}_{\rm H} = -J_{\rm H} \sum_{i,\alpha} \boldsymbol{S}_i \cdot \boldsymbol{s}_{i,\alpha} \tag{1.29}$$

where $\boldsymbol{s}_{i,\alpha} = 1/2 \sum c_{i\alpha\mu}^{\dagger} \boldsymbol{\sigma}_{\mu\nu} c_{i\alpha\nu}$ is the spin of the itinerant electron at orbital α and site i, with $\boldsymbol{\sigma}$ being the Pauli matrix. We will choose $J_{\rm H} > 0$, so that the Hund coupling is ferromagnetic.

Because of its dual character, the local-itinerant model is very versatile in explaining various properties of the iron-based superconductors. The AFM order of the local moments in the J_1-J_2 model will simultaneously induce the same AFM order of the itinerant electrons. Using the RPA technique, we can calculate the dynamical susceptibility of the composite spins, consisting of both the local moments and the spins of the itinerant electrons [98]. The result at low energy displays the well-defined spin-wave excitation that is governed by the exchange interaction. When the energy becomes higher, the presence of the itinerant electrons leads to an energy-dependent damping effect. If we go above two times the AFM gap magnitude, the spin excitation is dominated by

the particle-hole continuum. These behaviors are consistent with the inelastic neutron scattering (INS) results in several materials [99, 100, 101]. The Hund coupling between the local moments and the itinerant electrons also provides the necessary pairing interaction. The s_{+-} superconducting state emerges in both the paramagnetic and antiferromagnetic phase [102].

Another interesting result from the local-itinerant model is the anisotropy of the effective exchange constants. Our work [103] is the first to address this issue and will be presented in detail in Chapter 5. The basic idea is that there exists an effective ferromagnetic exchange between the local moments due to the Hund coupling to the itinerant electrons. Its competition with the superexchanges J_1 and J_2 will stabilize the $(\pi, 0)$ magnetic order. Furthermore, a ferro-orbital order of the itinerant electrons can spontaneously arise. It produces very anisotropic corrections to the spin interactions along the two in-plane directions. In the appropriate parameter regime, we can even tune the exchange along the y direction, J_{1y}, to be ferromagnetic, corresponding to the unfrustrated magnetism observed by the INS experiment [81, 100]. Using the same idea based on the competition between double exchange and superexchange, researchers have proposed [104] that the local-itinerant model can unify different magnetic orders in the iron-based superconductors.

The biggest shortcoming of the local-itinerant model is that it artificially separates the localized and the itinerant electrons. Such a separation is probably unphysical, as the AFM order and superconductivity may arise from the same electrons [76, 77]. Second, as we will see in Chapter 3, the local moment also has an orbital degree of freedom, and is more appropriately described by the Kugel-Khomskii model, instead of the Heisenberg model. Third, the itinerant electrons should be defined only around the Fermi energy. However, the multi-orbital model used here comes from the fitting over several eV, and may not accurately capture the low-energy physics. Finally, an orbital independent Hund coupling is also unrealistic.

Chapter 2

"Nematic" order in iron-based superconductors

The term "nematic" comes from the studies of the classical liquid crystals. In its original meaning, the nematic phase breaks a *continuous* rotational symmetry, but remains invariant under other symmetry operations, such as inversion and translation. However, in the presence of a lattice, the underlying symmetry of the system becomes discrete. So the nematic order actually breaks a *discrete* rotational symmetry, with the resulting ground state being two-fold degenerate. As we have learned in Chapter 1, the iron-based superconductors can exhibit the structural phase transition in the absence of the long-range magnetic order. This orthorhombic phase sandwiched between T_S and T_N is exactly the nematic phase we have just defined. This lattice C_4 symmetry breaking is driven by the electron degrees of freedom, namely the electron nematic order [105]. The electron nematic phase, one of the electron liquid crystal phases [106], is abundant in strongly correlated electron systems, such as the high Landau level quantum hall system, cuprates, bilayer ruthenates, and also the iron-based superconductors we considered here (for a review, see Ref. [107]).

In this chapter, we will talk about both the experimental and theoretical aspects of the electron nematic order in the iron-based superconductors. Sec. 2.1 will introduce a plethora of the experiments that found strong evidences of the in-plane electronic and magnetic anisotropy. This section serves as the experimental motivation of the thesis. In Sec. 2.2, two different origins of the electron nematic order will be discussed. We will argue that the orbital order, instead of the spin-nematic order, is the effective cause of the nematicity in the iron-based superconductors.

2.1 Experimental evidence of the in-plane anisotropy

From the symmetry point of view, the electron nematic order and the crystal structural distortion break the same lattice C_4 rotational symmetry, and thus will have the same onset temperature in a Landau-Ginzburg theory. So it is always ambiguous to distinguish which one of the two is the underlying cause of the symmetry breaking. However, one critical observation here is that the lattice distortion is too small to account for the large electronic anisotropy

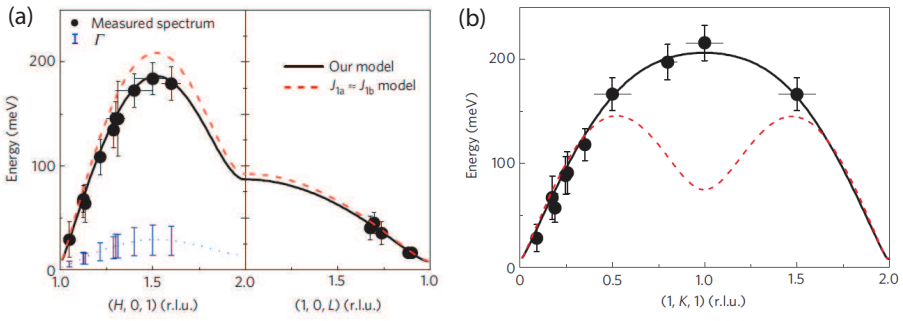

Figure 2.1: Spin-wave dispersion along the high-symmetry directions in $CaFe_2As_2$. The filled circles are from the INS experiment. The black solid and the red dashed lines are the fitting results by the anisotropic and isotropic Heisenberg models, respectively. The fitting parameters are $SJ_{1a} = 49.9 \pm 9.9$, $SJ_{1b} = -5.7 \pm 4.5$, $SJ_2 = 18.9 \pm 3.4$, $SJ_c = 5.3 \pm 1.3$ meV for the anisotropic model, and $SJ_{1a} = 27$, $SJ_{1b} = 25$, $SJ_2 = 36$, $SJ_c = 5.3$ meV for the isotropic model. The length of the blue vertical bars in (a) represents the momentum dependence of the spin-wave damping Γ. From Ref. [81].

seen experimentally. Consequently, in our point of view, the electron nematic order is the main symmetry breaking mechanism, whereas the structural phase transition simply follows. In this section, we will list a series of the experiments that found the electronic anisotropy in the iron-based superconductors. Some of them are summarized in a recent review article [108].

2.1.1 Inelastic neutron scattering (INS)

Generally the INS experiments measure the dynamical spin correlation function $\chi^s(q, \omega)$. As we have shown in Chapter 1, this quantity can be calculated by either the RPA approach in the weak-coupling theories, or the linear spin-wave theory in the strong-coupling Heisenberg models. So by fitting the INS experimental results with the existing theories, we will be able to extract important parameters in our theory. However, the multi-orbital band structure complicates the RPA-type spin susceptibility. Furthermore, the presence of the particle-hole continuum at high energy makes the analysis even more difficult. So far no direct fitting has been done using the RPA spin correlation function. We are restricted to the fitting results of the Heisenberg models.

INS is arguably the first experiment to discover the in-plane anisotropy. Early experiments carried out at low energy [109] already hinted that the underlying magnetic exchange is highly anisotropic, with $J_{1a} \gg J_{1b}$. We have used J_{1a} and J_{1b} to represent the exchange couplings between the nearest neighbors along the AFM x direction and the FM y direction, respectively. But more conclusive results are from the later INS experiment of $CaFe_2As_2$ that covers the entire spectrum [81]. We can read from Fig. 2.1(b) that the spin-wave energy at (π, π) does not go to zero as predicted by the isotropic J_1-J_2 model, but instead reaches a maximum. Obviously, nearly isotropic exchange constants fail to de-

scribe the experimental results (red dashed line in Fig. 2.1). The best fitting can be only achieved using the anisotropic Heisenberg model (black solid line in Fig. 2.1). Not only do we have $J_{1a} \gg J_{1b}$, but it is also required that J_{1b} be slightly ferromagnetic. In contrast to the early claim of frustrated magnetism, the INS experiments reveal that an unfrustrated spin model underlies the iron pnictides. More recently, the INS experiments were pushed into the paramagnetic (PM) phase [100]. When we go above the Néel temperature T_N, the spin-wave excitation becomes gapped at the ordering wave vector as expected, whereas the high energy excitation at the zone boundary remains almost the same. This result tells us that the magnetic exchanges are still anisotropic in the PM phase.

However, we need to be careful here. Across the structural phase transition, the crystal does not distort uniformly, but forms dense twin domains in which the lattice constant is longer in either the x or y direction. Consequently, in the magnetically ordered state, there are almost equal amounts of the $(\pi, 0)$ and $(0, \pi)$ order, associated with the domains of $a > b$ and $a < b$, respectively. So the spin excitation measured by the INS experiment comes from both types of the magnetic orders, and is thus C_4 symmetric. However, the fitting can still be carried out. All we need to do is to calculate $\chi(q_x, q_y, \omega)$ from some Heisenberg model, and take the average of $\chi(q_x, q_y, \omega)$ and its 90^o rotation counterpart, $\chi(q_y, q_x, \omega)$. In this sense, the anisotropy of the exchange constants observed in the tetragonal phase above T_N, does not represent a nematic order. Instead, it signals the nematic fluctuation, which leads to the magnetic anisotropy within its correlation length.

2.1.2 Scanning tunneling microscopy (STM)

STM measures the local tunneling current I from a sample at a certain bias voltage V. By doing a derivative, one can obtain the local conductance $g(r, E)$, which is related to the local density of states. Its Fourier transform $g(q, E)$, which is named the quasiparticle interference (QPI) image, provides important information of the system, such as the dispersion of the quasiparticles, the symmetry and structure of the superconducting gap. Detailed review of the STM study in the iron-based superconductors can be found in Ref. [110].

Because STM is a local probe, its measurement will not be affected by the formation of the domains. As shown by the local conductance $g(r, E)$ image in Fig. 2.2(a), a clear domain wall is formed along the diagonal of the image. The lower right region has the magnetic order at $\boldsymbol{Q} = (\pi, 0)$, with the spins ferromagnetically aligned along the y direction, whereas the upper left region is characterized by the $(0, \pi)$ magnetic order. By a careful examination of the $g(r, E)$ image, we can observe some unidirectional structures within each domain. This C_4 symmetry breaking is more evident if we perform a Fourier transform of $g(r, E)$ and plot the resulting QPI image $g(q, E)$ [see the inset

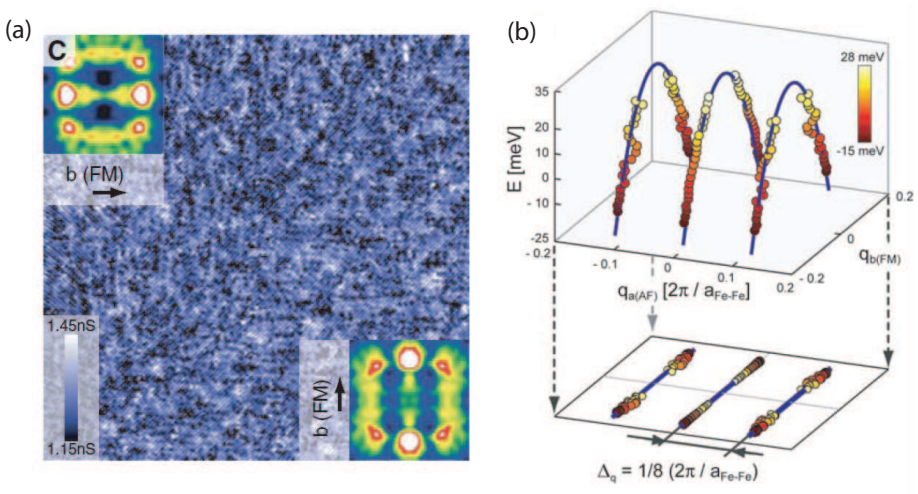

Figure 2.2: (a) The local conductance image $g(r, E)$ of $Ca(Fe_{1-x}Co_x)_2As_x$ ($x = 0.03$). The domain wall is seen along the diagonal. Inset displays its Fourier transform, namely the QPI image $g(q, E)$, which rotates by 90^o across the twin boundary. Both images are taken at $E = -10$ meV. (b) The dispersion of the QPI pattern. Circles represent the peaks extracted from each QPI image $g(q, E)$. Blue lines are the parabolic fit. QPI pattern shows a hole-like dispersion, which is only dispersive along the FM direction. The center peaks are separated from the side peaks by a wave vector of $2\pi/8$. From Ref. [111].

of Fig. 2.2(a)]. By varying the tunneling energy E, we find that the peak of $g(q, E)$ only moves along the ferromagnetic y direction for the $(\pi, 0)$ ordered region [Fig. 2.2(b)]. The distance between the main peak and the two side peaks along the AFM x direction remains almost the same at $2\pi/8$, which reminds us of the 1/8 anomaly in the cuprate superconductors. Both the band structures from the LDA [112] and the mean-field [113] theories in the AFM phase have been used to calculate the QPI image. But neither of them can reproduce this nearly one-dimensional QPI pattern with the 1/8 modulation. It is still an open question to identify the nontrivial electronic order that contributes to this peculiar QPI image. One possible solution is that the scattering center has a dimer structure[1].

We should note that it is incorrect to use the term "nematic" to describe the C_4 symmetry breaking observed here. The STM experiment is done at low temperature, where the long-range AFM order already sets in. This stripe-type AFM order is characterized by the ordering wave vector $\boldsymbol{Q} = (\pi, 0)$, with the spins being antiparallel along the x direction and parallel along y, and thus breaks the lattice C_4 symmetry. However, another symmetry, namely the translational symmetry along the x direction, is also broken by the AFM order. Therefore, according to the terminology of the classical liquid crystals [106], we should name such a phase "smectic" instead of "nematic".

Later STM experiments [114, 115] also confirmed this in-plane anisotropy

[1] M. P. Allan and J. C. Davis, private communications.

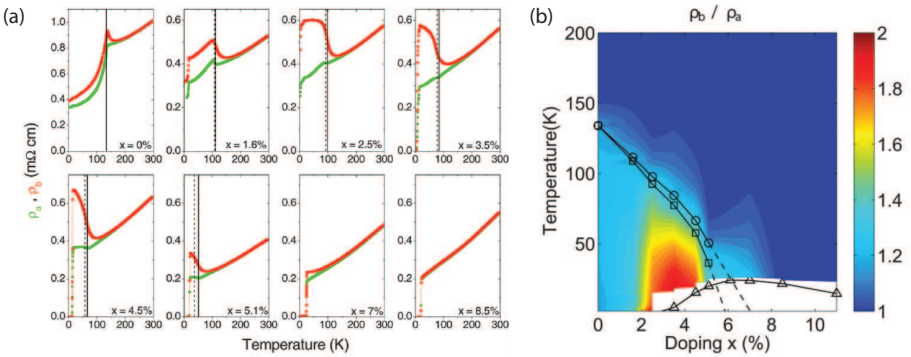

Figure 2.3: (a) Temperature dependence of the in-plane resistivity ρ_a and ρ_b of the detwinned $Ba(Fe_{1-x}Co_x)_2As_2$ crystals for various doping levels from $x = 0$ to $x = 0.085$. The vertical solid and dashed lines mark the structural and magnetic transition temperatures T_S and T_N of the unstressed samples, respectively. (b) The in-plane resistivity ratio ρ_b/ρ_a, as a function of temperature T and doping x. The structural, magnetic, and superconducting transition temperatures are also shown. From Ref. [119].

in various iron-based superconductors, suggesting the universality of this C_4 symmetry breaking. Here we would like to emphasize one particular experiment [115] on FeSe materials. As we have mentioned earlier, FeSe is a superconductor with a transition temperature $T_c = 8\,\mathrm{K}$ at ambient pressure [16]. A structural phase transition from tetragonal to orthorhombic occurs at 90 K [28], but no long-range magnetic order is observed down to zero temperature, which makes FeSe an ideal system for the study of nematic order. By either applying a magnetic field or depositing additional Se atoms, experimentalists can suppress superconductivity locally. The induced vortex core and the QPI image both show very strong anisotropy [115]. It is an outstanding question to understand the interplay between nematic order and superconductivity [116, 117].

2.1.3 Resistivity measurement

As discussed earlier, the formation of the dense twin domains usually prevents the bulk measurements from detecting the intrinsic anisotropy in the iron-based superconductors. This anisotropy will remain hidden unless we can develop a proper technique to detwin the crystal. In early attempts, an in-plane magnetic field is applied [118], which leads to a moderate change of the relative twin populations. The real breakthrough comes from the mechanic method that can almost fully detwin the crystal [119]. In these experiments, a uniaxial stress is applied to the crystal along one Fe-Fe direction. If it is compressive [119], the shorter b axis will be favored along the stress direction upon the structural phase transition, whereas the tensile stress [120] will prefer the longer a axis.

In Fig. 2.3(a), the resistivity along the two in-plane directions, ρ_a and ρ_b, are plotted as functions of temperature T for various doping levels x [119]. The

resistivity anomaly is still seen around the structural and magnetic transition temperature T_S and T_N of the unstressed samples. It may suggest that the applied uniaxial stress is a weak symmetry breaking field, and does not affect the transition temperature. In Fig. 2.3(b), the ratio ρ_b/ρ_a is plotted across the entire phase diagram. We would like to point out two important features of these figures.

First, the resistivity is always higher along the FM b direction. However, simple argument that the scattering from spin fluctuations is stronger along the AFM a direction will lead to a higher resistivity along a. Furthermore, according to the previous STM result [111], the quasiparticles are only dispersive along the FM b direction, and thus higher resistivity should also be expected along the AFM a direction. So what causes the higher resistivity along the FM b direction? In one theory, it comes from the Drude weight difference between the two in-plane directions, due to the Fermi surface reconstruction by the AFM order. Indeed, a simple mean-field theory calculation found higher Drude weight and thus lower resistivity along the AFM a direction [121]. On the other hand, another theory advocates that the electron transport is dominated by the *hot spots* from the spin fluctuations [122]. The positions of these hot spots, relying on the shape of the hole and electron pockets, determine the higher resistivity direction. While the former theory is more straightforward, only the latter one can explain the puzzling result that in hole-doped $Ba_{1-x}K_xFe_2As_2$, resistivity anisotropy is vanishingly small [123], possibly with slightly higher resistivity along the AFM a direction [124].

Second, the resistivity anisotropy sets in above the structural phase transition. One simple explanation is that the applied uniaxial stress already breaks the crystal C_4 symmetry and turns the sharp transition into a broad crossover. The induced resistivity anisotropy signals a large nematic susceptibility. However, some recent x-ray [125] and neutron scattering [126] experiments suggested that applying the uniaxial stress effectively raises the Néel temperature T_N, and thus the in-plane anisotropy is simply due to the onset of the long-range magnetic order. We note here that in $Ba(Fe_{1-x}Co_x)_2As_2$, the structural phase transition, which is separated from the magnetic transition, is of the second-order type. So the critical temperature T_S is more susceptible to the external field. In contrast, for $CaFe_2As_2$ and $SrFe_2As_2$, in which the structural and magnetic transitions are simultaneous and first order, the resistivity anisotropy is only observed below T_S [127].

2.1.4 Optical conductivity

Optical conductivity $\sigma(\omega)$ measures the current-current correlation function. It provides information of the system on the energy scale of the incoming photons. In the context of the iron-based superconductors, it has been used to extract the magnitude of the AFM order [128], although the multi-band character compli-

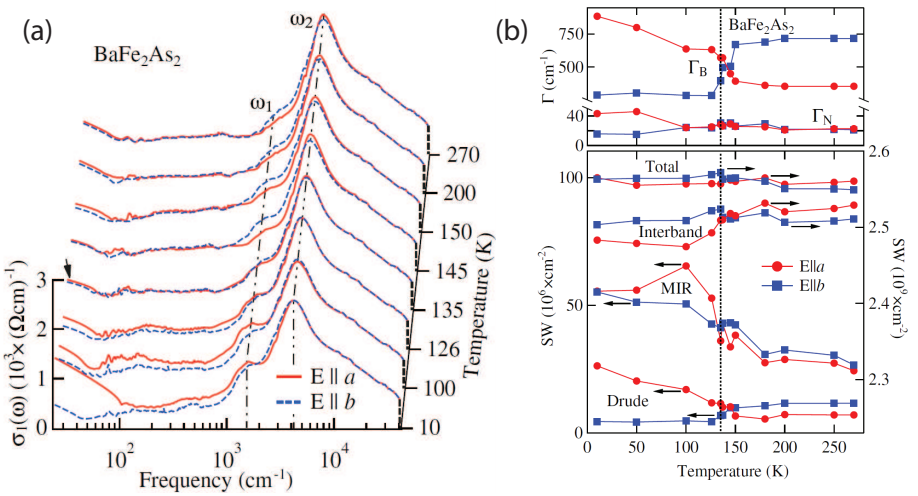

Figure 2.4: (a) Optical conductivity $\sigma(\omega)$ of the detwinned $BaFe_2As_2$ along the two in-plane directions at various temperatures. ω_1 and ω_2 represent two characteristic frequencies. (b) Analysis of the optical conductivity. (Upper panel) Temperature dependence of the scattering rate. Γ_B and Γ_N are the scattering rates of the broad and the narrow Drude parts, respectively. (Lower panel) Temperature dependence of the spectral weight from the Drude, mid-infrared (MIR) and interband contributions, respectively. From Ref. [129].

cates the analysis. Because it is also a bulk measurement, we can only observe the anisotropy in optical conductivity in detwinned crystals.

Detailed experimental results can be found in Ref. [129], [130], and [131]. Their results are mostly consistent with each other. In Fig. 2.4(a), the two in-plane optical conductivity $\sigma_{aa}(\omega)$ and $\sigma_{bb}(\omega)$ in detwinned $BaFe_2As_2$ are plotted for temperatures from 10 K to 270 K. As with the resistivity, the anisotropy of the optical conductivity turns on above the structural and magnetic transitions because of the applied uniaxial stress. We can identify two peak features associated with the frequency ω_1 and ω_2, respectively. The shoulder at ω_1 comes from the onset of the magnetic order, and gradually increases when we go deeper into the AFM phase. Basically, the AFM order partially opens up a gap at the Fermi energy, and shifts part of the spectral weight from low energy to high energy. On the other hand, the peak at ω_2 originates from the interband transitions. It barely changes with the temperature.

We can gain more insights by decomposing the optical conductivity into various parts. As shown by the lower panel of Fig. 2.4(b), the optical conductivity consists of three major components, the Drude term, the mid-infrared (MIR) term, and the high-energy interband contribution. We will focus on the Drude term, which can be further decomposed into broad and narrow parts. From Fig. 2.4(b), we see that above the magnetostructural transition, the Drude weight is larger along the FM b direction. So it is the larger scattering rate along b that contributes to a higher resistivity along b. However, below the magne-

tostructural transition, the scattering rate becomes larger along the AFM a direction instead, possibly due to magnetic fluctuations. But the Drude weight also becomes larger along a, which overcomes the scattering rate difference. So we still end up with a higher resistivity along b. So from this analysis of the optical conductivity, the anisotropy of the resistivity has two distinct origins across the magnetostructural transition. Both the Drude weight [121] and the scattering rate [122] play important roles here. As we will show in Chapter 4, orbital order is another key ingredient [132, 133] in understanding the results from transport experiments.

2.1.5 Angle-resolved photoemission spectroscopy (ARPES)

In general, one can write the ARPES intensity as [134]

$$I(k,\omega) = |M^k_{f,i}|^2 f(\omega) A(k,\omega) \tag{2.1}$$

where k and ω are the in-plane momentum and the energy of the electron. $M^k_{f,i}$ is the matrix element that depends on the energy and polarization of the incoming photon, and the momentum of the outgoing electron. $f(\omega) = 1/\left(\exp\left(\omega/k_BT\right)+1\right)$ is the Fermi-Dirac distribution function. $A(k,\omega)$ is the spectral function, defined as the imaginary part of the retarded Green function,

$$A(k,\omega) = -\frac{1}{\pi}\Im\left[\mathcal{G}(k,\omega+i\delta)\right]. \tag{2.2}$$

For a noninteracting system, $A(k,\omega) = \delta(\omega-\epsilon_k)$. Generally this δ-function will be broadened to a Lorentzian line shape due to scattering processes. So the ARPES experiments provide direct measurement of the electron dispersion ϵ_k. Another advantage of ARPES comes from the matrix element $M^k_{f,i}$. Tuning the polarization of the incoming light suppresses some electron orbitals as a result of the selection rules. We can make use of this feature to investigate the orbital components, which turns out to be a convenient way to study a multi-orbital system, such as the iron-based superconductors.

Evidences of the in-plane anisotropy have been found by early ARPES experiments on twinned crystals [135, 136]. Experimentalists used a laser spot that is small enough to be comparable to the typical domain size. Thus one particular domain makes the dominant contribution so that the C_4 symmetry breaking can be observed. It is shown that upon the onset of the $(\pi,0)$ AFM order, an orbital-dependent Fermi surface reconstruction occurs with the d_{xz} orbitals dominating the states near the Fermi energy [135]. This result is consistent with theoretical predictions from mean-field theory [137].

However, ARPES experiments performed on detwinned crystals give us more important insights [138]. In Fig. 2.5, the electron dispersion of detwinned $BaFe_2As_2$ is plotted along the two in-plane directions, Γ-X and Γ-Y, respec-

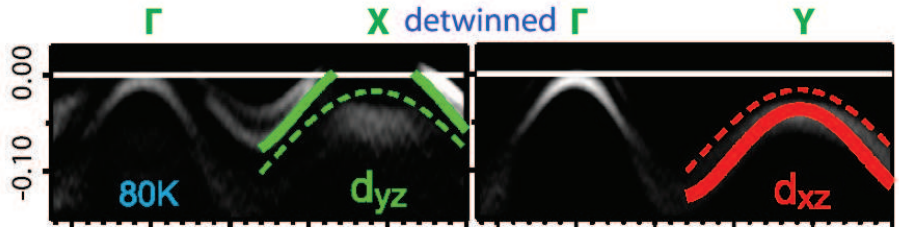

Figure 2.5: Orbitally polarized dispersions along Γ-X and Γ-Y lines at 80 K in detwinned $BaFe_2As_2$, derived from the ARPES measurement. Due to the polarization of the incoming photon, the band at X is mostly composed of the Fe d_{yz} orbital, whereas the d_{xz} orbital dominates the band at Y. From Ref. [138].

tively. In experimental setup, the polarization of the incoming photon selects the orbitals that are odd under reflection with respect to the incident plane. So we are able to detect only the d_{yz} and d_{xy} orbitals along Γ-X, whereas only the d_{xz} and d_{xy} orbitals are active along Γ-Y. The splitting between the bands at X and Y signals a possible energy difference between the d_{xz} and d_{yz} orbitals. As we will see in Chapter 4, this energy splitting term, combined with the mean-field AFM order, is able to reproduce the band dispersion observed here.

Again because of the applied uniaxial stress, the band splitting is seen above the structural transition temperature T_S. By comparing the ARPES results on twinned and detwinned samples, researchers found the splitting even occurs above T_S in twinned crystals [138]. But it does not represent a nematic order, but may arise from short-range orbital or magnetic orders. Recently, researchers have performed ARPES experiments on detwinned NaFeAs [139, 140], in which the structural and the magnetic transitions are well separated. They found that the Fermi surfaces of NaFeAs undergo a C_4 symmetry breaking between T_S and T_N, and that the distorted hole and electron pockets have better nesting conditions. This result suggests an interesting interplay between the nematic and the $(\pi, 0)$ AFM order.

2.1.6 Other experiments

The in-plane electronic anisotropy also manifests itself in other experiments, for example, point contact spectroscopy (PCS). In these experiments, one measures the differential conductance $G(V) = dI/dV$ of a point contact junction between two different materials. In the ballistic regime, we have

$$G(V) = \int \frac{\mathrm{d}^3\boldsymbol{k}}{(2\pi)^3} v_\perp(\boldsymbol{k}) \delta\left(\epsilon_{\boldsymbol{k}} - V\right) \tag{2.3}$$

where $v_\perp(\boldsymbol{k}) = \partial\epsilon_{\boldsymbol{k}}/\partial k_\perp$ is the velocity in the normal direction. As a result, $G(V)$ contains the information about the system's density of states (DOS). As

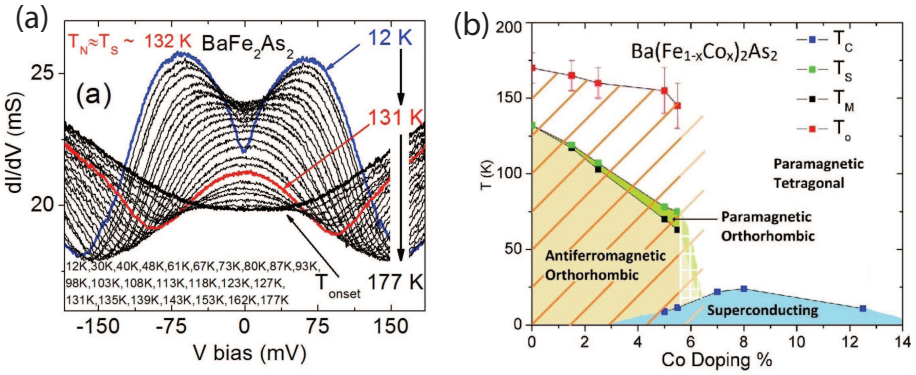

Figure 2.6: (a) Differential conductance $G(V)$ for $BaFe_2As_2$. The red curve is taken at the magnetostructural transition temperature $T_S = T_N = 132\,\mathrm{K}$. The zero-bias conductance enhancement is observed well above T_S. Well below T_N, a double-peak structure develops. (b) The phase diagram of $Ba(Fe_{1-x}Co_x)_2As_2$ from the point contact spectroscopy. The phase below T_o has strong nematic (orbital) fluctuations, which cause the zero-bias conductance enhancement. From Ref. [142]

shown by Fig. 2.6(a), there exists an enhancement of $G(V)$ at $V = 0$ well above the magnetostructural transition [141, 142]. This zero-bias conductance enhancement is intimately related to non-Fermi liquid behavior caused by the nematic fluctuations, or equivalently the orbital fluctuations above T_S [143]. In Fig. 2.6(b), we show the onset temperature of the orbital fluctuations, T_o. Interestingly, in the overdoped samples where no structural transition occurs, the orbital fluctuations also vanish. It will be appealing if the evidences of the nematic or orbital fluctuations can be found in other experimental probes.

However, recent torque magnetometry measurements[2] on $BaFe_2(As_{1-x}P_x)_2$ told a different story. By rotating the in-plane magnetic field, experimentalists found that the magnetic torque displays a two-fold oscillation, which signals a C_4 symmetry breaking. Surprisingly, the onset temperature of this two-fold oscillation, T^*, is well above the structural transition temperature T_S. Using a Landau-Ginzburg theory, they concluded that T^* indeed marks the true onset temperature of the nematic order. The lattice distortion also occurs at T^* due to the symmetry breaking. But its magnitude is too small to be experimentally detectable until T_S, at which the lattice distortion undergoes a discontinuous jump. Similar to our earlier argument, the symmetry breaking above T_S can be caused by the applied in-plane magnetic field. But it is also possible that the smallness of the sample size used in this experiment helps to reveal the hidden nematic order. We will have to wait until other experiments can provide more definite evidence.

[2]S. Kasahara and Y. Matsuda, private communications.

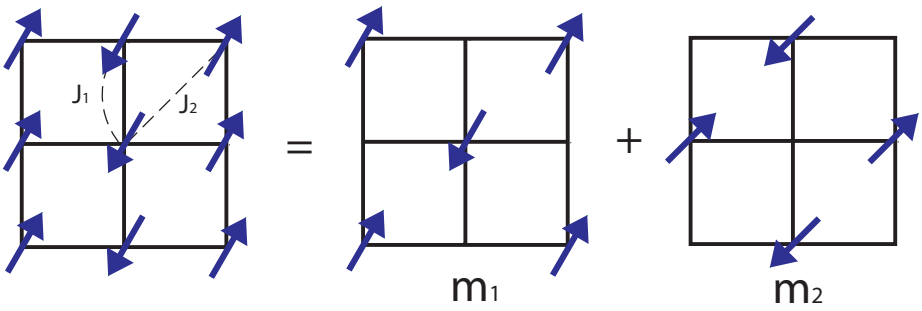

Figure 2.7: Illustration of the Ising-nematic order from the J_1-J_2 model. The original square lattice is broken into two interpenetrating sublattices. On each sublattice, the spins are antiparallel with their nearest neighbors, with the staggered magnetization defined as $\boldsymbol{m}_1$ and $\boldsymbol{m}_2$. Classically the angle θ between $\boldsymbol{m}_1$ and $\boldsymbol{m}_2$ is arbitrary. Fluctuations lift the degeneracy, resulting in $\theta = 0$ or π, corresponding to the ordering wave vector $\boldsymbol{Q} = (\pi, 0)$ or $(0, \pi)$.

2.2 Origin of the nematic order

Having discussed the experimental side, now let us turn to the theories of nematic order in the iron-based superconductors. In short, existing theories can be categorized into two distinct types. In one theory, nematic order comes from spin fluctuations, which offers a natural explanation of the proximity of the structural and the magnetic transitions. In contrast, the other theory ascribes the C_4 symmetry breaking to orbital order, which can spontaneously arise in a multi-orbital system, such as the iron-based superconductors. We will discuss these two types of theories in Sec. 2.2.1 and Sec. 2.2.2, respectively.

2.2.1 Spin fluctuation

As we have learned in Sec. 1.2.2, the J_1-J_2 Heisenberg model gives a strong-coupling account of the $(\pi, 0)$ antiferromagnetic order. Furthermore, we will demonstrate here that the structural phase transition may arise from the Ising-nematic order in the J_1-J_2 model [144, 145, 146]. It is known that in the classical limit, the stripe-type $(\pi, 0)$ or $(0, \pi)$ magnetic order will win over the (π, π) AFM order if the $J_2 > J_1/2$. We should also notice that in this regime, the $(\pi, 0)$ and $(0, \pi)$ AFM order are not the only two classical ground states. As illustrated by Fig. 2.7, the original square lattice can be broken into two interpenetrating sublattices. On each sublattice, there exists an AFM order, with the spins between the nearest neighbors being antiparallel. We will define the staggered magnetization on each sublattice as $\boldsymbol{m}_1$ and $\boldsymbol{m}_2$, respectively. If the spins are treated as the classical vectors, it can be easily verified that the ground state energy is independent of the angle θ between $\boldsymbol{m}_1$ and $\boldsymbol{m}_2$. Thus the classical ground state manifold is $S^2 \bigotimes S^2$. However, if we take the quantum or thermal fluctuations into account, this infinite ground state degeneracy will be greatly lifted. The angle θ between $\boldsymbol{m}_1$ and $\boldsymbol{m}_2$ can only take discrete values of 0 and π,

corresponding to the $(\pi, 0)$ and $(0, \pi)$ AFM order in the original square lattice. The ground state manifold is reduced to $S^2 \bigotimes Z_2$. This is the so-called *order from disorder* mechanism [147, 148].

Formally, we can perform a gradient expansion and derive the following Hamiltonian [144, 145, 146]

$$\mathcal{H} = \int \mathrm{d}^2 \boldsymbol{r} J_2 \left(|\boldsymbol{\nabla} \boldsymbol{m}_1|^2 + |\boldsymbol{\nabla} \boldsymbol{m}_2|^2 \right) + J_1 \boldsymbol{m}_1 \cdot \partial_x \partial_y \boldsymbol{m}_2 - K \left(\boldsymbol{m}_1 \cdot \boldsymbol{m}_2 \right)^2, \quad (2.4)$$

where $K \sim J_1^2 / J_2$, arising from fluctuations. Because $K > 0$, in order to minimize the energy, it is required that $\boldsymbol{m}_1$ and $\boldsymbol{m}_2$ are either parallel or antiparallel. To describe such a Z_2 order, we further introduce a Hubbard-Stratonovich field σ, which couples to $\boldsymbol{m}_1 \cdot \boldsymbol{m}_2$,

$$\mathcal{L}' = -\sigma \left(\boldsymbol{m}_1 \cdot \boldsymbol{m}_2 \right) + \frac{1}{4K} \sigma^2. \quad (2.5)$$

The Ising order parameter $\sigma = \pm 1$ corresponds to the $(\pi, 0)$ and $(0, \pi)$ AFM order, respectively.

Very interestingly, for a pure two-dimensional system, there exists a finite-temperature Ising transition to an Ising ordered state with nonzero expectation value of σ, $\langle \sigma \rangle \neq 0$. However, according to the Mermin-Wagner theorem [149], no continuous symmetry breaking can occur at finite temperature. Thus $\langle \boldsymbol{m}_1 \rangle = \langle \boldsymbol{m}_2 \rangle = 0$ unless T goes to zero. Therefore, we find a phase in which the lattice C_4 symmetry is broken by a finite $\langle \sigma \rangle$, without the onset of the long-range AFM $O(3)$ order. This is exactly the nematic phase we have defined earlier.

Certainly the real system is never pure two dimensional. We will introduce the magnetic exchange J_z along the c axis to represent the three-dimensional coupling. As shown in Fig. 2.8, as J_z increases, the Ising-nematic and the $O(3)$ AFM transitions start to merge together. It qualitatively explains why these two transitions are separate in some materials, while being coincident in others. Researchers have also studied the effects of doping and pressure, and found some consistency with experiments [150, 151].

Obviously the most apparent problem here is that the J_1-J_2 model cannot explain the magnetic excitations measured by the INS experiments (see Sec. 2.1.1). The biquadratic exchange arising from fluctuations has an energy scale $K \sim 0.01 J_2$ [145], which is too small to account for the observed magnetic anisotropy. To solve the problem, researchers have directly included the biquadratic term in the bare Hamiltonian and proposed the so-called J_1-J_2-K model [152],

$$\mathcal{H}_{\mathrm{loc}} = J_1 \sum_{\langle i,j \rangle} \boldsymbol{S}_i \cdot \boldsymbol{S}_j + J_2 \sum_{\langle\langle i,j \rangle\rangle} \boldsymbol{S}_i \cdot \boldsymbol{S}_j + K \sum_{\langle i,j \rangle} \left(\boldsymbol{S}_i \cdot \boldsymbol{S}_j \right)^2 \quad (2.6)$$

where K is the bare biquadratic couplings between the spins on the nearest neighbor sites. In such a model, the effective exchange interactions between the

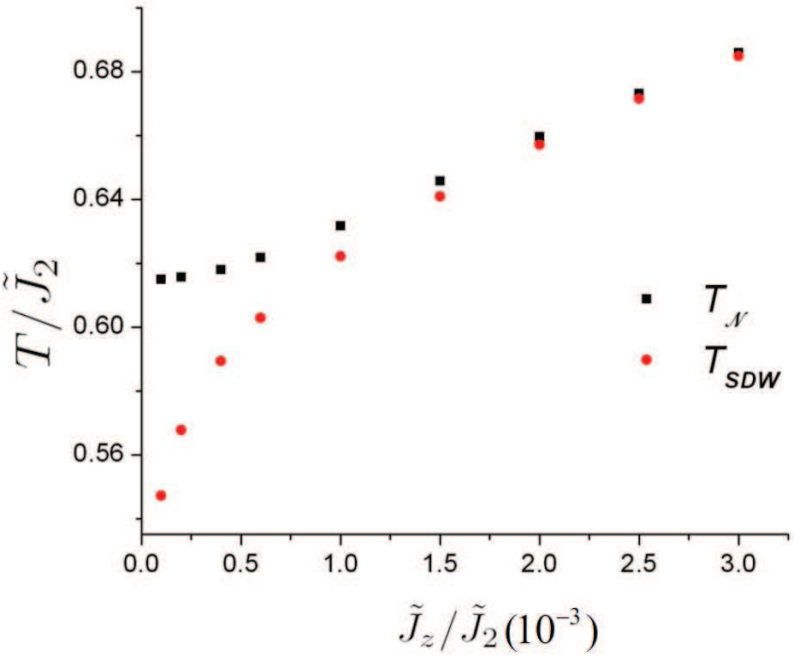

Figure 2.8: The critical temperature of the Ising-nematic transition and the antiferromagnetic transition, $T_{\mathcal{N}}$ and $T_{\rm SDW}$, as a function of the magnetic coupling along the z direction, J_z. From Ref. [145].

nearest neighbors are renormalized by the K term. The calculated spin excitations are consistent with the experiments in both the magnetically ordered phase [152] and the paramagnetic phase [153, 154]. It is argued that the extension of this model can provide a unified description of the magnetism in both iron pnictides and iron chalcogenides [155]. Theoretically, we can motivate this biquadratic K term by doing a strong-coupling expansion to the fourth order. However, other four-spin terms, such as the ring exchange term, should also appear. But they are neglected without any justification. It is also unclear why the biquadratic K term between the NNN spins is not considered.

Besides the above strong-coupling theories, the Ising-nematic order can be also formulated using the weak-coupling approach [156]. We will make use of the multi-band model $\mathcal{H}_K$ (1.13), and explicitly consider one hole pocket at $\Gamma = (0, 0)$ and two electron pockets at $X = (\pi, 0)$ and $Y = (0, \pi)$, respectively. The magnetic interaction $\mathcal{H}_{\rm AFM}$ (1.16) occurs between the hole pocket and both of the electron pockets. The first step is to introduce two bosonic fields,

$$\boldsymbol{\Delta}_X \sim \sum c^\dagger_{\boldsymbol{k}\mu} \boldsymbol{\sigma}_{\mu\nu} d_{X,\boldsymbol{k}+\boldsymbol{Q},\nu}, \tag{2.7}$$

$$\boldsymbol{\Delta}_Y \sim \sum c^\dagger_{\boldsymbol{k}\mu} \boldsymbol{\sigma}_{\mu\nu} d_{Y,\boldsymbol{k}+\boldsymbol{Q},\nu}, \tag{2.8}$$

which represent two competing AFM orders with $\boldsymbol{Q} = (\pi, 0)$ and $\boldsymbol{Q} = (0, \pi)$,

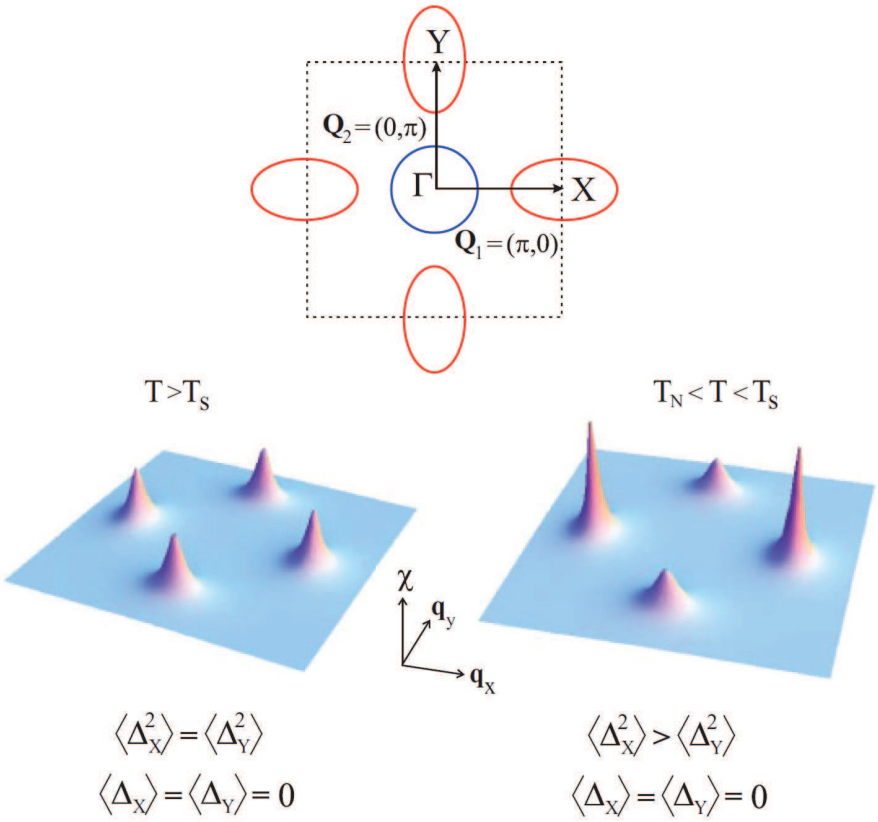

Figure 2.9: (Upper panel) The band structure in the 1-Fe BZ. We have a circular hole pocket at Γ and two electron pockets at X and Y. (Lower panel) Magnetic fluctuations for different temperatures. Above the structural transition temperature T_S, the two ordering wave vectors $\boldsymbol{Q} = (\pi, 0)$ and $\boldsymbol{Q} = (0, \pi)$ are equivalent with $\langle \boldsymbol{\Delta}_X^2 \rangle = \langle \boldsymbol{\Delta}_Y^2 \rangle$. Below T_S but still above the Néel temperature T_N, fluctuations at one wave vector become stronger, $\langle \boldsymbol{\Delta}_X^2 \rangle > \langle \boldsymbol{\Delta}_Y^2 \rangle$. So the C_4 rotational symmetry is broken without the long-range magnetic order, $\langle \boldsymbol{\Delta}_X \rangle = \langle \boldsymbol{\Delta}_Y \rangle = 0$. From Ref. [156].

respectively (Fig. 2.9). We will do the standard Hubbard-Stratonovich transformation to decouple the AFM interaction term $\mathcal{H}_{\text{AFM}}$ (1.16). By integrating out the fermionic fields, we write down the effective action of $\boldsymbol{\Delta}_X$ and $\boldsymbol{\Delta}_Y$ up to the fourth order [156, 157],

$$S_{\text{eff}}\left[\boldsymbol{\Delta}_X, \boldsymbol{\Delta}_Y\right] = r_0 \left(\boldsymbol{\Delta}_X^2 + \boldsymbol{\Delta}_Y^2\right) + \frac{u}{2}\left(\boldsymbol{\Delta}_X^2 + \boldsymbol{\Delta}_Y^2\right)^2 - \frac{g}{2}\left(\boldsymbol{\Delta}_X^2 - \boldsymbol{\Delta}_Y^2\right)^2. \quad (2.9)$$

If the nesting condition is perfect, namely $m = m_x = m_y$ and $\epsilon_{h,0} = \epsilon_{e,0}$ [see Eq. (1.14) and (1.15)], it is found that $g = 0$. Therefore, below the Néel temperature T_N, any solution that satisfies $\langle \boldsymbol{\Delta}_X \rangle^2 + \langle \boldsymbol{\Delta}_Y \rangle^2 = -r_0/u$ will minimize S_{eff}. Both the AFM orders with $\boldsymbol{Q} = (\pi, 0)$ and $\boldsymbol{Q} = (0, \pi)$ can coexist in our system. However, the nesting is never perfect in real systems, leading to a positive g. So we will have a configuration with either $\langle \boldsymbol{\Delta}_X \rangle \neq 0$ or $\langle \boldsymbol{\Delta}_Y \rangle \neq 0$,

but both cannot be nonzero simultaneously. It is analogous to the Z_2 order in the aforementioned J_1-J_2 model.

Now the question is whether this Z_2 transition can occur before the $O(3)$ symmetry breaking. The answer is yes. As illustrated by Fig. 2.9, at high temperatures, the spin fluctuations are equally strong at the two competing ordering wave vectors $\boldsymbol{Q} = (\pi, 0)$ and $\boldsymbol{Q} = (0, \pi)$. Once we go across the structural phase transition temperature T_S, the magnetic fluctuations become stronger at one wave vector, say $\boldsymbol{Q} = (\pi, 0)$. Then we will have $\langle \boldsymbol{\Delta}_X^2 \rangle > \langle \boldsymbol{\Delta}_Y^2 \rangle$, which breaks the C_4 lattice rotational symmetry. However, the long-range magnetic order at $\boldsymbol{Q} = (\pi, 0)$, which corresponds to $\langle \boldsymbol{\Delta}_X \rangle \neq 0$ and $\langle \boldsymbol{\Delta}_Y \rangle = 0$, only occurs at a lower temperature T_N.

Formally, we can introduce two new Hubbard-Stratonovich fields ψ and ϕ, which are coupled to the fluctuations $\boldsymbol{\Delta}_X^2 + \boldsymbol{\Delta}_Y^2$ and $\boldsymbol{\Delta}_X^2 - \boldsymbol{\Delta}_Y^2$, respectively. We notice that ψ always has a nonzero expectation value and describes Gaussian fluctuations. On the other hand, if the ϕ field obtains a nonzero expectation value, the system will undergo an Ising-nematic transition. We can derive the effective action of ψ and ϕ, $S_{\text{eff}}[\psi, \phi]$, by integrating out the $\boldsymbol{\Delta}_X$ and $\boldsymbol{\Delta}_Y$ fields. The stationary solutions of ψ and ϕ can be found by minimizing $S_{\text{eff}}[\psi, \phi]$. Detailed calculations are in Ref. [156]. The results are very similar to those from the previous J_1-J_2 model. When the nematic coupling strength g/u is large, the structural and the magnetic transitions are separate, with both being second order. In the opposite limit that g/u is small, the system only exhibits one first-order transition. Distinct from the strong-coupling results is the new phase for the intermediate values of g/u. In this phase, the system first undergoes a second-order nematic transition and then at a lower temperature, a first-order magnetic transition. This behavior is consistent with the latest experimental results on $Ba(Fe_{1-x}Co_x)_2As_2$ [26, 27].

Finally we briefly comment on the equivalence between these two theories. Indeed their starting points are exactly opposite. One is built from a local moment model governed by the exchanges J_1 and J_2, whereas the other relies on the SDW instability between the hole and electron pockets. But most importantly, they share the same ground state manifold of $S^2 \bigotimes Z_2$. The Z_2 Ising-nematic order can be spontaneously broken, without the onset of an $O(3)$ type magnetic order. Actually, with the identification that $\boldsymbol{\Delta}_X = \boldsymbol{m}_1 + \boldsymbol{m}_2$ and $\boldsymbol{\Delta}_Y = \boldsymbol{m}_1 - \boldsymbol{m}_2$, we see that the nematic order parameters in these two theories are equivalent,

$$\boldsymbol{\Delta}_X^2 - \boldsymbol{\Delta}_Y^2 \sim \boldsymbol{m}_1 \cdot \boldsymbol{m}_2. \tag{2.10}$$

2.2.2 Orbital order

In the preceding section, we saw that nematic order can occur because the spin fluctuations select a preferable direction above the Néel temperature, T_N. In

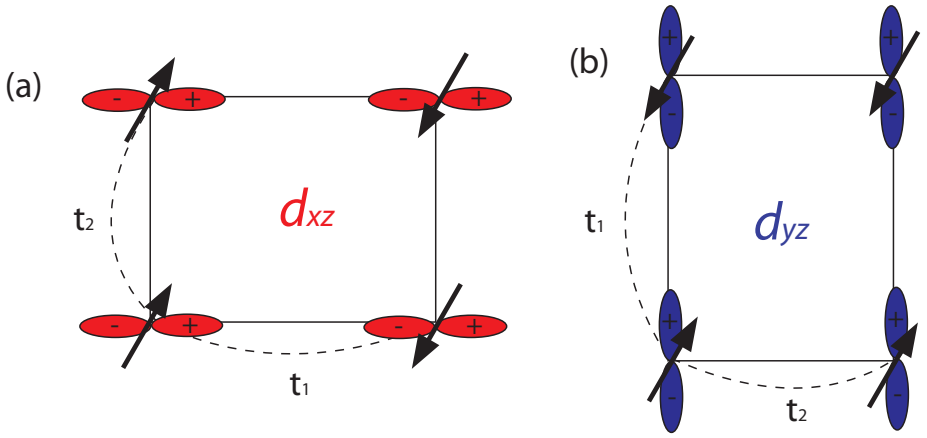

Figure 2.10: Orbital order, and the resulting magnetic order with the anisotropic exchange constants. (a) The d_{xz} orbital order and the $\boldsymbol{Q} = (\pi, 0)$ AFM order. t_1 and t_2 are the hopping amplitudes along the x and y directions, respectively. (b) The d_{yz} orbital order and the $\boldsymbol{Q} = (0, \pi)$ AFM order.

this section, we would like to discuss another possible origin of nematic order, namely orbital order. This is a natural scenario in a multi-orbital system, such as the iron-based superconductors.

From the strong-coupling point of view, the one-band Hubbard model at half filling can be reduced to the Heisenberg model when $U \gg t$. But the same strong-coupling expansion for the multi-orbital Hubbard model does not only involve the spin degrees of freedom, but also the orbital degrees of freedom. The resulting low-energy Hamiltonian is the so-called Kugel-Khomskii model [94]. The physics of the Kugel-Khomskii model and its application to the iron-based superconductors [158] are the main contents of Chapter 3, where our contribution [159] will be presented in Sec. 3.2.

But the basic idea is actually quite simple. For simplicity, let us consider a system consisting of only two $3d$ orbitals, d_{xz} and d_{yz}. We note that d_{xz} and d_{yz} are the only two $3d$ orbitals that break the lattice C_4 rotational symmetry locally. Above the structural phase transition temperature T_S, each site can be equally populated with the d_{xz} and d_{yz} orbitals. The C_4 symmetry is preserved and the lattice is tetragonal. When the temperature goes below T_S, without loss of generality, we assume that the system prefers to be occupied by the d_{xz} orbital [Fig. 2.10(a)]. This inequivalence between the d_{xz} and d_{yz} orbitals breaks the C_4 rotational symmetry and induces a structural distortion. We further consider the magnetic superexchanges from the virtual hopping processes with the hopping amplitudes t_1 and t_2 along the x and y directions, respectively. Immediately we have the exchange constants $J_{1a} = 4t_1^2/U$ and $J_{1b} = 4t_2^2/U$, where U is the intra-orbital Coulomb repulsion. Due to the spatial anisotropy of the d_{xz} orbital, it is assumed that $t_1 \gg t_2$ and consequently $J_{1a} \gg J_{1b}$, which leads to the $\boldsymbol{Q} = (\pi, 0)$ AFM order [Fig. 2.10(a)], if the NNN exchange J_2 satisfies $J_2 > J_{1b}/2$. The onset of magnetic order can only occur after orbital

order has already set in. Therefore the Néel temperature cannot be higher than the structural transition temperature, $T_N \leq T_S$. Similarly, for the d_{yz} orbitally ordered state, we will have $J_{1a} \ll J_{1b}$ and the $\boldsymbol{Q} = (0, \pi)$ AFM order [Fig. 2.10(b)]. We see that the anisotropy of the exchange constants comes from the orbital order that breaks the C_4 rotational symmetry.

Similar to the theories of the spin fluctuations, orbital order can be also formulated from the weak-coupling limit. It is related to the Pomeranchuk instability [160]. Formally, we consider the interaction between two electrons on the Fermi surface with momenta $\boldsymbol{k}_1$ and $\boldsymbol{k}_2$. The interaction can be written in both the charge and the spin channels,

$$f_{\alpha\beta,\gamma\delta}(\boldsymbol{k}_1, \boldsymbol{k}_2) = f^s(\boldsymbol{k}_1, \boldsymbol{k}_2)\delta_{\alpha\beta}\delta_{\gamma\delta} + f^a(\boldsymbol{k}_1, \boldsymbol{k}_2)\boldsymbol{\sigma}_{\alpha\beta} \cdot \boldsymbol{\sigma}_{\gamma\delta}. \tag{2.11}$$

We further decompose each interaction by its angular momentum, and define the Landau parameter $F_l^{s,a} = N_0 f_l^{s,a}$, where l is the angular momentum and N_0 is the density of states at Fermi energy. In the seminal work of Pomeranchuk [160], he considered an arbitrary deformation of the Fermi surface [see Fig. 2.11(a)] and asked the question whether the system is stable against these deformations. After careful calculations, he found that the changes of the kinetic and the interaction energies are

$$\Delta E_K \sim \left(\delta n_l^{s,a}\right)^2, \quad \Delta E_I \sim \frac{F_l^{s,a}}{2l+1}\left(\delta n_l^{s,a}\right)^2, \tag{2.12}$$

where $\delta n_l^{s,a}$ is the component of the deformation with angular momentum l, in the charge and spin channel. In order to have the Fermi surface being stable against the deformations, it is required that

$$F_l^{s,a} > -(2l+1). \tag{2.13}$$

If this criterion is not satisfied, a possible Fermi surface deformation can occur. The most common example is Stoner ferromagnetism from the s-wave spin interaction F_0^a, as shown by Fig. 2.11(b). Nematic order corresponds to the instability in the d-wave charge channel F_2^s [see Fig. 2.11(c) for the illustration].

Examining the Fermi surfaces of the iron-based superconductors [Fig. 1.5(b)], we find that the dominant orbital component on the Fermi surfaces changes between d_{xz} and d_{yz} by a 90^o rotation. Because of the difference in the intra-orbital and inter-orbital electron interactions, the Landau parameter F_2^s is greatly enhanced. The resulting nematic order is equivalent to the orbital order in the multi-orbital systems. This argument is behind the multi-orbital theoretical work [161, 162] explaining nematic order in the bilayer ruthenates. In the iron-based superconductors, self-consistent mean-field calculations do not produce the orbital order in the absence of the magnetic order [51, 137, 163]. Due to the simultaneous onset of the AFM order, we cannot associate this orbital or-

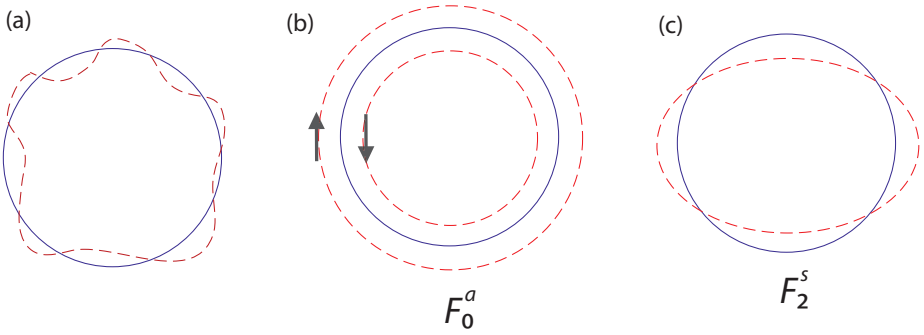

Figure 2.11: (a) An arbitrary Fermi surface deformation. (b) Ferromagnetic order from the spin interaction in the s-wave channel. (c) Nematic order from the charge interaction in the d-wave channel.

der with the nematic order. Nevertheless, the appearance of the orbital order above the Néel temperature T_N has strong experimental support. So we will phenomenologically include an energy splitting term between the Fe d_{xz} and d_{yz} orbitals, and investigate its experimental consequences. The details of our work [133] will be presented in Chapter 4.

Chapter 3

Orbital order from strong coupling

3.1 Preliminary: Kugel-Khomskii model

The idea of orbital order originates from the seminal work of Kugel and Khmoskii [94]. They note that some transition metal compounds are characterized by a partially filled band with orbital degeneracy. Interactions can lift this orbital degeneracy, and induce orbital order with the corresponding lattice distortion. In this section, we will use $KCuF_3$ as an example and introduce the theory of orbital order, with the emphasis on the Kugel-Khomskii model. We should note that these theories were developed for insulators. In contrast, the iron-based superconductors are metals in their normal state. However, due to the fact that some $3d$ electrons are effectively localized, we can still apply these models to the iron-based superconductors.

In $KCuF_3$, each Cu atom is surrounded by six F atoms in an octahedral setting (see Fig. 3.3 for an illustration). Under the cubic crystal field, the five Cu $3d$ orbitals are split into two groups. The e_g subgroup at higher energy consists of the $d_{x^2-y^2}$ and $d_{3z^2-r^2}$ orbitals, while the d_{xy}, d_{xz}, and d_{yz} orbitals make up the t_{2g} subgroup at lower energy [see Fig. 3.1(a)]. We have a total of nine electrons occupying these five orbitals. So there exists a single hole in the two e_g orbitals. With the orbital degeneracy being preserved, the single hole can occupy any state that is a linear combination of the $d_{x^2-y^2}$ and $d_{3z^2-r^2}$ orbitals. Formally, we can parameterize the hole state by

$$|\theta\rangle = \cos\left(\frac{\theta}{2}\right)|z\rangle + \sin\left(\frac{\theta}{2}\right)|x\rangle, \tag{3.1}$$

where the orbital states are defined as

$$|z\rangle = \left(3z^2 - r^2\right)/\sqrt{6}, \quad |x\rangle = \left(x^2 - y^2\right)/\sqrt{2}. \tag{3.2}$$

Due to the structure of this two-fold degeneracy, an orbital pseudospin operator $\boldsymbol{T}$ with $T = 1/2$ can be introduced to represent the two orbital states, with

$$|z\rangle = \begin{pmatrix} 1 \\ 0 \end{pmatrix}, \quad |x\rangle = \begin{pmatrix} 0 \\ 1 \end{pmatrix}. \tag{3.3}$$

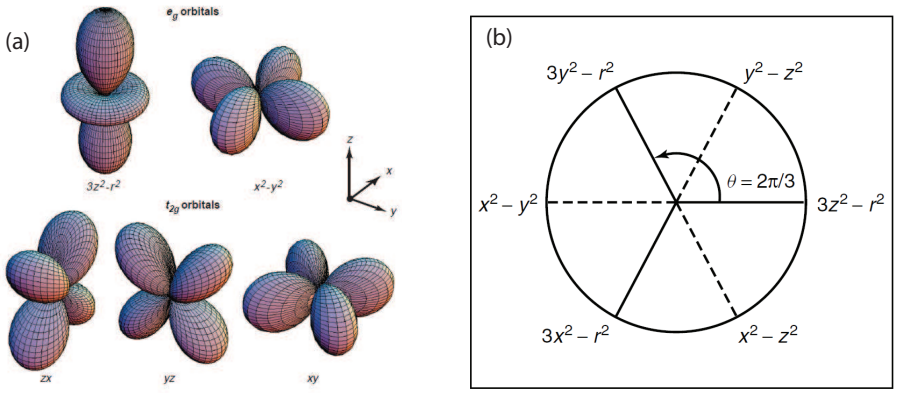

Figure 3.1: (a) The cubic crystal field lifts the degeneracy of the $3d$ orbitals. The e_g orbitals ($d_{x^2-y^2}$ and $d_{3z^2-r^2}$) have a higher energy than the t_{2g} orbitals (d_{xy}, d_{xz}, and d_{yz}). From Ref. [164]. (b) Schematic representation of the orbital states obtained by the linear combination of the two e_g orbitals. From Ref. [165].

In Fig. 3.1(b), we show various orbital states that can be obtained by varying the mixing angle θ.

According to Kugel and Khomskii [94], this orbital degeneracy can be lifted by the interactions. In a lattice system, there are generally three types of these interactions. The first is the electron-phonon interaction, which couples the lattice displacements with the occupation numbers of the orbitals. The second type is the quadrupole-quadrupole interaction, due to the quadrupole moment of the d orbitals. For these two types of interactions, we can directly integrate out the lattice variables and derive the effective Hamiltonian in terms of the orbital pseudospin operators $\boldsymbol{T}$. The general form is written as,

$$\mathcal{H}\left(\boldsymbol{T}_i, \boldsymbol{T}_j\right) = \sum_{\langle i,j \rangle} J_{ij}^{zz} T_i^z T_j^z + J_{ij}^{xx} T_i^x T_j^x + J_{ij}^{yy} T_i^y T_j^y + J_{ij}^{zx} \left(T_i^z T_j^x + T_i^x T_j^z\right), \quad (3.4)$$

where the "exchange" constants J_{ij}^{zz}, J_{ij}^{xx}, and J_{ij}^{yy} can all take different values, and the off-diagonal "exchange" J_{ij}^{zx} is generally nonzero. So unlike the real spin $\boldsymbol{S}$, the Hamiltonian of the orbital pseudospin $\boldsymbol{T}$ is not $SU(2)$ invariant. It has been shown that $\mathcal{H}\left(\boldsymbol{T}_i, \boldsymbol{T}_j\right)$ (3.4) takes the form,

$$\mathcal{H}^a = \sum_{\langle i,j \rangle} J^a \left(-\frac{1}{2} T_i^z + \frac{\sqrt{3}}{2} T_i^x\right)\left(-\frac{1}{2} T_j^z + \frac{\sqrt{3}}{2} T_j^x\right), \quad (3.5)$$

$$\mathcal{H}^b = \sum_{\langle i,j \rangle} J^b \left(\frac{1}{2} T_i^z + \frac{\sqrt{3}}{2} T_i^x\right)\left(\frac{1}{2} T_j^z + \frac{\sqrt{3}}{2} T_j^x\right), \quad (3.6)$$

$$\mathcal{H}^c = \sum_{\langle i,j \rangle} J^c T_i^z T_j^z, \quad (3.7)$$

along the three crystal axes, a, b and c, respectively. We notice that the interaction depends on the direction of the bond (i, j). Furthermore, the orbital

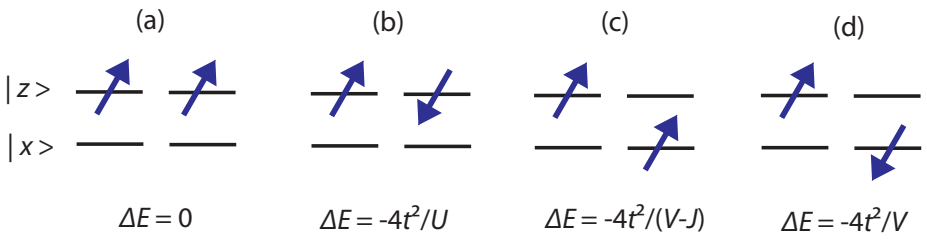

Figure 3.2: Illustration of the Goodenough-Kanamori rule. We consider the superexchanges of the e_g orbitals along the c axis, where only the hopping of the $d_{3z^2-r^2}$ orbital is allowed. The energy of each orbital and spin configuration is calculated by second-order perturbation theories. U, V, and J are the intra- and inter-orbital Coulomb repulsion, and the Hund coupling, respectively.

pseudospin $\boldsymbol{T}$ is reduced to an Ising variable along each crystal axis.

The last type of the interaction in an orbital degenerate system is the exchange interaction. Unlike the first two interactions, which can be expressed exclusively by the orbital pseudospins, the exchange interaction also involves the spin degrees of freedom. In many systems, it makes the dominant contribution to the orbital and spin orders. We will introduce this spin-orbital superexchange model, namely the Kugel-Khomskii model in the remainder of this section.

We will first present the arguments behind the Goodenough-Kanamori rule [166, 167] to show how orbital and spin orders are coupled to one another. As an example, we consider the superexchange of the holes at two neighboring sites along the c axis in $KCuF_3$. Because the $d_{x^2-y^2}$ orbital is highly two dimensional, only the hopping amplitude between the $d_{3z^2-r^2}$ orbital is nonzero and we define it as t. We need to consider four distinct orbital and spin configurations on the two sites, as illustrated in Fig. 3.2. The energies of these states can be easily calculated by the second-order perturbation theory. If both sites are occupied by the $d_{3z^2-r^2}$ orbital [Fig. 3.2(a) and (b)], the exchange is strongly antiferromagnetic (AFM). The effective spin-only model is

$$\mathcal{H}\left(\boldsymbol{S}_i, \boldsymbol{S}_j\right) = \frac{4t^2}{U} \sum_{\langle i,j \rangle} \boldsymbol{S}_i \cdot \boldsymbol{S}_j. \tag{3.8}$$

where U is the intra-orbital Coulomb repulsion. In contrast, if different orbitals occupy the two sites [Fig. 3.2(c) and (d)], the exchange becomes weakly ferromagnetic (FM), with

$$\mathcal{H}\left(\boldsymbol{S}_i, \boldsymbol{S}_j\right) = \left(\frac{4t^2}{V} - \frac{4t^2}{V-J}\right) \sum_{\langle i,j \rangle} \boldsymbol{S}_i \cdot \boldsymbol{S}_j \approx -\frac{4t^2 J}{V^2} \sum_{\langle i,j \rangle} \boldsymbol{S}_i \cdot \boldsymbol{S}_j, \tag{3.9}$$

in the limit that the Hund coupling J is much smaller than the inter-orbital Coulomb repulsion V. Our results can be summarized by the Goodenough-Kanamori rule: (1) If there is a strong overlap between the two occupied or-

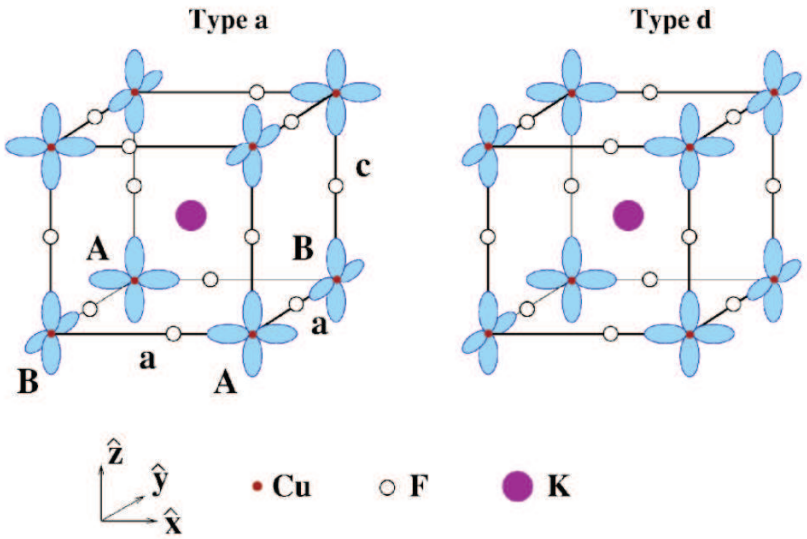

Figure 3.3: The atomic structure and the orbital order of $KCuF_3$. In the ab plane, there is an alternating configuration of the $d_{x^2-z^2}$ and $d_{y^2-z^2}$ orbitals. Along the c axis, the orbitals in the ab plane are stacked either antiferromagnetically (type a on the left), or ferromagnetically (type d on the right). From Ref. [168].

bitals, the superexchange between them is strongly AFM; (2) If a large overlap occurs between a filled orbital and a vacant orbital, we have a weakly FM superexchange. So we see that the spin interaction depends on the orbital configuration in the system.

As shown in Fig. 3.3, there exist two types of the orbital order in $KCuF_3$. For both of them, the $d_{x^2-z^2}$ and the $d_{y^2-z^2}$ orbitals alternate with each other between the nearest neighbors in the ab plane. Applying the argument of Goodenough-Kanamori, we predict that the spins will form an FM order in the ab plane. Along the c axis, the orbitals can be aligned either antiferromagnetically (type a) or ferromagnetically (type d). Both types possess a large overlap of the occupied orbitals along the c axis, leading to the spin AFM order. This A-type spin order, which is characterized by the FM ab planes being stacked antiferromagnetically along the c axis, indeed occurs in $KCuF_3$.

Now let us formally derive the Kugel-Khomskii model from a second-order strong-coupling expansion of the multi-orbital Hubbard model. We will still use $KCuF_3$ as the example. In the hole basis, the virtual hopping process leading to the superexchanges is $d^1d^1 \rightarrow d^2d^0 \rightarrow d^1d^1$. As a first step, we need to find the multiplet structure of the intermediate d^2 state. The standard on-site Hubbard interaction $\mathcal{H}_I$ (1.6) can be easily diagonalized in the d^2 configuration. Following the convention used in Ref. [169], we have

(i) the triplet

$$|^3A_2\rangle = \begin{cases} |z\uparrow, x\uparrow\rangle \\ \frac{1}{\sqrt{2}}\left(|z\uparrow, x\downarrow\rangle + |z\downarrow, x\uparrow\rangle\right) \\ |z\downarrow, x\downarrow\rangle \end{cases}, \tag{3.10}$$

with the energy eigenvalue

$$E\left(^3A_2\right) = V - J, \tag{3.11}$$

(ii) the interorbital singlet

$$|^1E_\epsilon\rangle = \frac{1}{\sqrt{2}}\left(|z\uparrow, x\downarrow\rangle - |z\downarrow, x\uparrow\rangle\right), \tag{3.12}$$

with eigenvalue

$$E\left(^1E_\epsilon\right) = V + J, \tag{3.13}$$

(iii) the bonding singlet

$$|^1E_\theta\rangle = \frac{1}{\sqrt{2}}\left(|z\uparrow, z\downarrow\rangle - |x\uparrow, x\downarrow\rangle\right), \tag{3.14}$$

with eigenvalue

$$E\left(^1E_\theta\right) = U - J', \tag{3.15}$$

and (iv) the antibonding singlet

$$|^1A_1\rangle = \frac{1}{\sqrt{2}}\left(|z\uparrow, z\downarrow\rangle + |x\uparrow, x\downarrow\rangle\right), \tag{3.16}$$

with eigenvalue

$$E\left(^1A_1\right) = U + J'. \tag{3.17}$$

Now we consider second-order perturbations from the kinetic energy $\mathcal{H}_K$. The general form of the Kugel-Khomskii model along a given bond (i, j) can be written as [158]

$$\mathcal{H}_{KK}^{(i,j)} = -\sum_{\tau_i,\tau_j}\sum_{s_i,s_j} J^{(i,j)}_{\tau_i,\tau_j,s_i,s_j} A^{(i,j)}_{\tau_i,\tau_j}(\boldsymbol{T}_i, \boldsymbol{T}_j) \times B_{s_i,s_j}(\boldsymbol{S}_i, \boldsymbol{S}_j), \tag{3.18}$$

where $\boldsymbol{S}$ and $\boldsymbol{T}$ are the $S = 1/2$ spin and the $T = 1/2$ orbital pseudospin operators, respectively. The superexchange J is proportional to t^2/E, where E is the excitation energy of the intermediate d^2 state.

The spin part $B_{s_i,s_j}(\boldsymbol{S}_i, \boldsymbol{S}_j)$ can be directly obtained by group theory techniques. Namely they will be the projection operators on the intermediate total

spin states,

$$B_{1,0}(\boldsymbol{S}_i, \boldsymbol{S}_j) = \frac{3}{4} + \boldsymbol{S}_i \cdot \boldsymbol{S}_j, \tag{3.19}$$

$$B_{0,0}(\boldsymbol{S}_i, \boldsymbol{S}_j) = \frac{1}{4} - \boldsymbol{S}_i \cdot \boldsymbol{S}_j. \tag{3.20}$$

The remainder depends on the exact virtual hopping processes. In general, we can write $\mathcal{H}_{KK}^{(i,j)}$ as a sum of each intermediate d^2 state,

$$\begin{aligned}\mathcal{H}_{KK}^{(i,j)} = & -\left(\boldsymbol{S}_i \cdot \boldsymbol{S}_j + \frac{3}{4}\right) \frac{1}{E\left({}^3A_2\right)} Q_{\left({}^3A_2\right)}\left(\boldsymbol{T}_i, \boldsymbol{T}_j\right) \\ & + \left(\boldsymbol{S}_i \cdot \boldsymbol{S}_j - \frac{1}{4}\right) \left\{ \frac{1}{E\left({}^1E_\epsilon\right)} Q_{\left({}^1E_\epsilon\right)}\left(\boldsymbol{T}_i, \boldsymbol{T}_j\right) \right. \\ & \left. + \frac{1}{E\left({}^1E_\theta\right)} Q_{\left({}^1E_\theta\right)}\left(\boldsymbol{T}_i, \boldsymbol{T}_j\right) + \frac{1}{E\left({}^1A_1\right)} Q_{\left({}^1A_1\right)}\left(\boldsymbol{T}_i, \boldsymbol{T}_j\right) \right\}. \end{aligned} \tag{3.21}$$

For simplicity, let us first consider the virtual hopping processes along the c axis. The only nonzero hopping amplitude is the one between the two neighboring $d_{3z^2-r^2}$ orbitals. Consequently we can express the initial and final states using the projection operators P_{iz} and P_{ix} on the $d_{3z^2-r^2}$ and $d_{x^2-y^2}$ orbitals. We have defined P_{iz} and P_{ix} as

$$P_{iz} = \frac{1}{2} + T_i^z, \tag{3.22}$$

$$P_{ix} = \frac{1}{2} - T_i^z. \tag{3.23}$$

Straightforward calculations yield along the c axis,

$$Q_{\left({}^3A_2\right)} = Q_{\left({}^1E_\epsilon\right)} = t^2 \left(P_{iz}P_{jx} + P_{ix}P_{jz}\right), \tag{3.24}$$

$$Q_{\left({}^1E_\theta\right)} = Q_{\left({}^1A_1\right)} = 2t^2 P_{iz}P_{jz}. \tag{3.25}$$

Along the a and b axes, the hopping Hamiltonian is more complicated. We can still express the initial and final states in terms of the orbital pseudospin operators $\boldsymbol{T}$, and proceed to write down all the contributing virtual processes. But a more clever approach is to perform a unitary transformation into a new orbital basis, where the hopping occurs only within one of two orbitals, namely the $d_{3x^2-r^2}$ orbital along the a axis and $d_{3y^2-r^2}$ along b. The explicit results can be found in Ref. [169]. It should be noted that our notations are slightly different. However, most importantly, we find that strong anisotropy usually occurs in the orbital space and that the exchange interactions of the orbital pseudospins are not $O(3)$ invariant.

So far we have discussed the interaction terms that are responsible for the breaking of the orbital degeneracy. There are three types of interactions, the electron-phonon, quadrupole-quadrupole, and exchange interactions. In terms of the orbital pseudospin operator $\boldsymbol{T}$, all three interactions are not $SU(2)$ invari-

ant. In many cases, the orbital pseudospin $\boldsymbol{T}$ is effectively reduced to an Ising variable T^z. Therefore, similar to the argument presented in Sec. 2.2, this Z_2 type Ising or orbital order can set in without breaking the spin $O(3)$ invariance. In our example $KCuF_3$, orbital order does occur at a temperature that is much higher than the Néel temperature T_N [170].

In the iron-based superconductors, we consider the two-orbital model consisting of the Fe d_{xz} and d_{yz} orbitals. The above consideration and formulation can be simply extended. We identify the Z_2 Ising order as the ferro-orbital order of either the d_{xz} or the d_{yz} orbital. This ferro-orbital order breaks the C_4 symmetry and induces the structural distortion. It is exactly the nematic order we have defined in Chapter 2.

The application of the Kugel-Khomskii model to the iron-based superconductors was pioneered by Ref. [158]. They considered the t_{2g} state, with the half filled d_{xy} orbital and the quarterly filled degenerate d_{xz} and d_{yz} orbitals. Their work is based on the low-spin $S = 1$ multiplet structure in d^6 configuration. However, the physics is simpler in the d_{xz} and d_{yz} two-orbital model at quarter filling. Although this model is inconsistent with the multiplet structure consideration, we find experimental support from the integrated spectral weight in recent inelastic neutron scattering experiments [171]. We were the first to propose this ferro-orbital order of the d_{xz} and d_{yz} orbitals causes the structural phase transition in the iron-based superconductors [159]. Our work will be presented in the following section, with an explicit calculation of the quadrupole-quadrupole interaction. Similar theories were also devised by others using Wannier orbitals constructed from LDA calculations [172]. Numerical simulations of the spin-orbital model give further support to our theory [173, 174].

3.2 Orbital order, structural phase transition and resistivity anomaly[1]

We attribute the structural phase transition (SPT) in the parent compounds of the iron pnictides to orbital ordering. Due to the anisotropy of the d_{xz} and d_{yz} orbitals in the xy plane, a ferro-orbital ordering makes the orthorhombic structure more energetically favorable, thus inducing the SPT. In this orbital-ordered system, the sites with orbitals that do not order have higher energies. Scattering of the itinerant electrons by these localized two-level systems causes a resistivity anomaly upon the onset of the SPT. The proposed orbital ordering also leads to the stripe-like antiferromagnetism and anisotropy of the magnetic exchanges. This model is quantitatively consistent with available experimental observations.

[1] This section is from Ref. [159].

3.2.1 Introduction

The structural phase transition (SPT) from tetragonal to orthorhombic symmetry around 150 K [175] is a ubiquitous feature in the parent compounds of the iron-based superconductors. Coincident with this transition is a resistivity anomaly (RA) [176] in which the resistivity turns up slightly before a sharp drop at exactly the onset temperature of the SPT, T_S. For the 1111-family, at a lower temperature, $T_{\rm SDW}$, a stripe-like antiferromagnetic spin density wave (SDW) forms [21] on the distorted lattice of Fe atoms, with the spins being parallel along the shorter axis and antiparallel along the longer axis. However, for the 122-family, the SDW develops at the same temperature as does the SPT, $T_{\rm SDW} = T_S$ [22]. In the 122-family [23], a single first-order transition obtains instead of two separate second-order transitions in the 1111-family. Upon doping, superconductivity (SC) occurs leading to a cessation of the SPT, RA and SDW [19, 177]. Hence, all of these three phenomena should be closely related and share a universal mechanism. However, most theoretical work only focuses on the connections between the SDW and SC. The importance of the SPT and RA is somehow underestimated. The main objective of this section is to explain the origin of the SPT and RA.

A common view [145, 146, 178, 179] is that the SPT is driven by the onset of the stripe-like antiferromagnetism. Both first principles calculations [178, 179] and Landau-Ginzburg modelings [145, 146] have been used in this context. The fact that the two transitions are decoupled in the 1111-family is a limitation of this approach. Further, since the origin of the SPT in their scenario is spin based, the onset temperature should be sensitive to an external magnetic field. However, experiments have shown that varying the magnetic field leads to no change in the onset temperature of the SPT [176].

In this section, we develop a microscopic theory of the SPT without involving the spin degrees of freedom. On our account, uneven occupations of the d_{xz} and d_{yz} orbitals make the orthorhombic crystal structure more energetically favorable, thus inducing the SPT. The operative mechanism driving this ferro-orbital-ordering transition is the lifting of the degeneracy between the d_{xz} and d_{yz} orbitals by the inter-site Coulomb repulsions. However, it should be noted that other important factors, such as spin-orbital interactions [94] and couplings to the displacements of ligand atoms (As), also contribute to this process. In fact, spin-orbital physics appears to lie at the heart of orbital ordering in the manganites [164]. While such physics is undoubtedly present in the pnictides [158, 180], quantifying it would require a first-principles calculation of the relevant parameters. However, as our goal is to propose a simple mechanism that explains both the SPT and the resistivity anomaly, we focus on a more easily quantifiable approach to orbital ordering based instead on the Coulomb repulsion. Indeed, what our work indicates is that there is a rich set of models which can lead to orbital ordering in the pnictides. Our model is

sufficiently simple and general that warrant its being taken seriously. The key insight gained from this study is not the detailed microscopic mechanism for this orbital-ordering-induced SPT, which is rather standard [164], but its direct consequence - a resistivity anomaly, which can be captured by our model in quantitative agreement with the experimental results [see Fig. 3.6(b)]. Furthermore, the stripe-like SDW and recently discovered anisotropy [81] of the magnetic exchanges naturally arise in our theory.

3.2.2 Orbital ordering

As emphasized by pioneering earlier work [158], the orbital degrees of freedom are important in the iron pnictides, which are intrinsically multi-orbital systems. For the Fe atom located at the center of the tetrahedron of four neighboring As atoms, five d orbitals are split into two groups, t_{2g} (d_{xy}, d_{xz}, d_{yz}) and e_g ($d_{x^2-y^2}$, $d_{3z^2-r^2}$). Three of the five orbitals, d_{xy}, $d_{x^2-y^2}$ and $d_{3z^2-r^2}$ are rotationally symmetric in the xy plane. So they are unlikely to have any effect on the SPT which is asymmetric in the xy plane. Then the only two possible candidates are the d_{xz} and d_{yz} orbitals. We propose the following mechanism for the SPT, assuming these two orbitals are localized. At high temperature $T > T_S$, d_{xz} and d_{yz} orbitals are degenerate, with equal numbers of electrons on both. A possible configuration is shown in Fig. 3.4(a), in which a square lattice is preferred. At low temperature, $T < T_S$, there is a majority of either d_{xz} or d_{yz}. For d_{yz} orbitals, the Coulomb repulsion of two neighboring sites is stronger along the y-direction than along the x-direction, which leads to a rectangular lattice with $a < b$ as shown in Fig. 3.4(b), where a and b are unit lengths in the x and y direction, respectively. Similarly, when d_{xz} dominates, the system will form the configuration of Fig. 3.4(c), which is degenerate with (b) by a rotation of 90 degrees.

To demonstrate the viability of this mechanism, we need to compare the energies of configuration (a) and (b) in Fig. 3.4. For simplicity, only the nearest-neighbor Coulomb repulsions are considered,

$$U = \int d\boldsymbol{r}\, d\boldsymbol{r'} \frac{e^2}{|\boldsymbol{r}-\boldsymbol{r'}|} \left|\psi_\alpha(\boldsymbol{r}-\boldsymbol{R}_i)\right|^2 \left|\psi_\beta(\boldsymbol{r'}-\boldsymbol{R}_j)\right|^2 \tag{3.26}$$

where $\psi_\alpha(\boldsymbol{r}-\boldsymbol{R}_i)$ is the wave function of the α ($\alpha = d_{xz}, d_{yz}$) orbital electron at site $\boldsymbol{R}_i$. This integral can be evaluated by an importance-sampling Monte-Carlo method. In configuration (a), we choose $a = b = a_0 = 2.85$ Å, which is the typical experimental value [175] for the 1111-family. For configuration (b), we define the lattice distortion δ as $a = a_0 - \delta$, and set $b = a_0^2/a$ to keep the area of a unit cell constant. We calculate the relative energy difference

$$\Delta(\delta) = \frac{U_b(\delta) - U_a}{U_a} \tag{3.27}$$

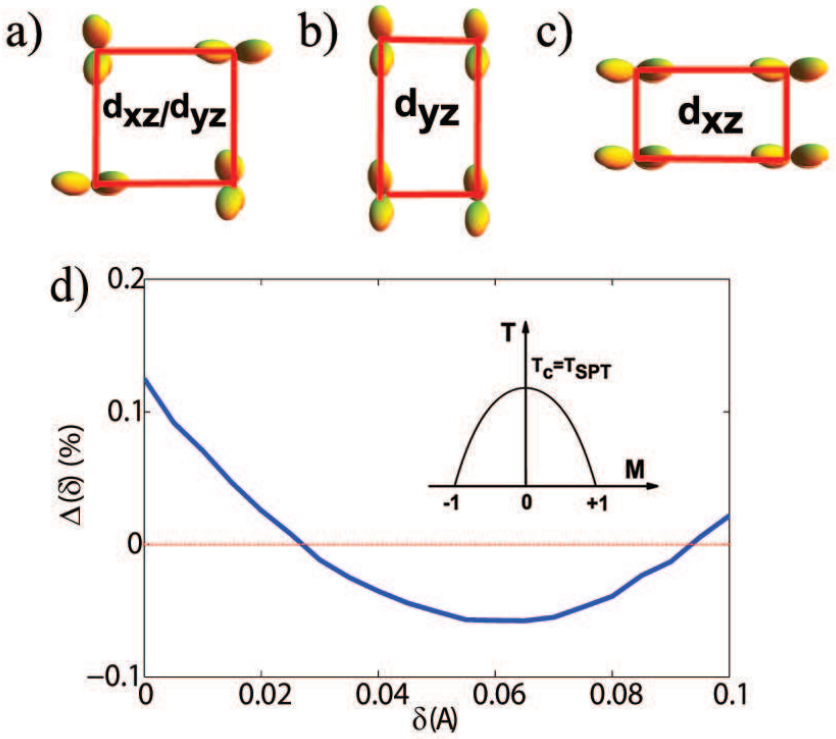

Figure 3.4: (a) Equal numbers of d_{xz} and d_{yz} with a square lattice configuration. (b) Entirely d_{yz} state with $a < b$. (c) Entirely d_{xz} state with $a > b$. d) Relative energy difference Δ between configurations (a) and (b), or (c), as a function of lattice distortion δ. (Inset: an Ising-type transition where the order parameter M is defined as the difference between the numbers of occupied d_{xz} and d_{yz} orbitals.)

as a function of δ, where U_a and U_b are energies of configurations (a) and (b) respectively. The results are shown in Fig. 3.4(d). For a lattice distortion 0.03 Å$< \delta <$ 0.09 Å, the rectangular lattice (b) or (c) is more energetically favorable. It is noted that this value is larger than the experimentally observed distortion of about 0.01 Å[175]. However, the localized states are probably neither d_{xz} nor d_{yz}, but some combinations of the d orbitals, or even involve hybridization with As p orbitals [95]. Thus the precise value of the distortion length can be smaller by taking these factors into account. As already mentioned, other possibilities may also induce this ferro-orbital ordering and the subsequent SPT. For example, Krüger *et. al* [158] derived a Kugel-Khomskii spin-orbital model and the resultant phase diagram does contain the same orbital configuration as proposed here. However, constructing the complete microscopic Hamiltonian that incorporates all the important physical processes requires a detailed knowledge of the relevant coupling parameters, which is currently unavailable. Thus the key point of our study is to put forth a simplified picture based on the

coupling only to the Coulomb interaction in which the rectangular lattice with ferro-orbital ordering emerges spontaneously at low temperature because of its lower energy.

Our model allows us to make the following conclusion. Upon the onset of the phase transition, a lattice distortion breaks the degeneracy between d_{xz} and d_{yz}. By occupying either one of these two orbitals, the system forms a ferro-orbital-ordered state and lowers its energy. It is this orbital-driven Jahn-Teller effect that induces the SPT. Defining $M_i = \pm 1$ for site i occupied by d_{xz} and d_{yz} orbitals respectively, we can write down an effective Ising-type Hamiltonian for the SPT

$$H_S = -J_S \sum_{\langle i,j \rangle} M_i M_j \tag{3.28}$$

where J_S should be on the order of the transition temperature, T_S. So the SPT belongs to the Ising universality class, as shown in the inset of Fig. 3.4(d), where the order parameter M is defined as $M = \sum_i M_i/N$.

Recently, angle-resolved photoemission experiments using a linear-polarized laser beam [135] show that at low temperature, the Fermi surface at the Brillouin zone center is dominated by a single d_{xz} or d_{yz} orbital, depending on the distortions. In their subsequent local-density approximation (LDA) calculations [135], it is found that the density of states of the d_{yz} orbitals with a lattice configuration of $a < b$ displays a peak around $0.5\,e$V from the chemical potential, which is just the localized state predicted in our SPT model. A recent optical measurement [181] also suggests evidences of the orbital ordering.

3.2.3 Resistivity anomaly

The ferro-orbital-ordering-driven SPT mechanism has an important consequence, namely the resistivity anomaly. The essential physics is that of a Kondo problem. The scattering of the itinerant electrons off two otherwise degenerate orbitals, d_{xz} and d_{yz}, will be suppressed by the gap opening, which results in a sharp drop of the resistivity upon the onset of the SPT.

Above T_S, the two d_{xz} and d_{yz} orbitals are degenerate. Below T_S, the occupancy of the electrons in d_{xz} and d_{yz} orbitals becomes unbalanced as a result of the distortion of the crystal to configuration (c) [or (b)] in Fig. 3.4. Thus, the electrons that remain in the d_{yz} (or d_{xz}) orbitals will have a higher energy and hence can lower their energy by jumping onto d_{xz} (or d_{yz}) orbitals. This process can be described by a localized two-level system. The classical analog, namely a double-well potential, is shown in Fig. 3.5(a). The corresponding Hamiltonian is given by

$$\begin{aligned} H_{\rm TLS} &= \lambda_{\rm ps} \sum_{\alpha} a_\alpha^\dagger a_\alpha + \frac{1}{2}\Delta \sum_{\alpha\beta} a_\alpha^\dagger \sigma_{\alpha\beta}^z a_\beta \\ &\quad + \frac{1}{2}\Delta_0 \sum_{\alpha\beta} a_\alpha^\dagger \sigma_{\alpha\beta}^x a_\beta \end{aligned} \tag{3.29}$$

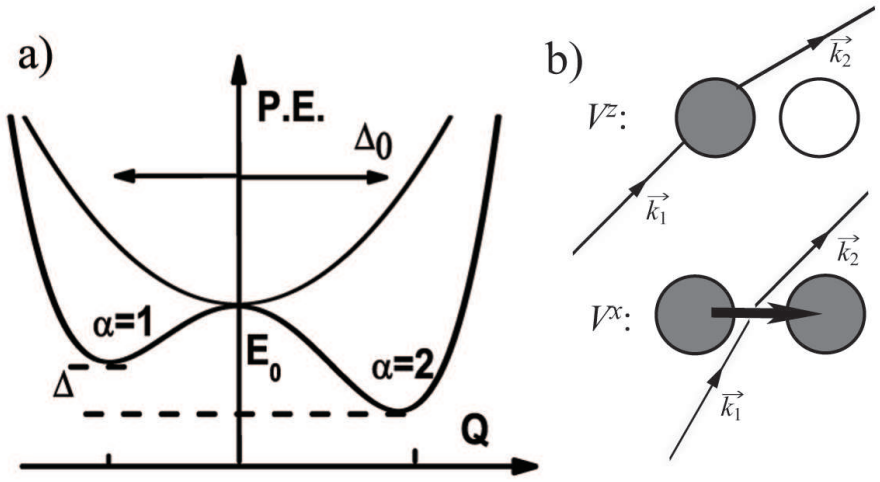

Figure 3.5: (a) A schematic of a double-well potential, as the classical analog of the two-level system. (b) Two types of scattering processes between the itinerant electrons and the localized states. V^z: diagonal scattering; and V^x: off-diagonal scattering.

where $a^\dagger_\alpha$ (a_α) creates (annihilates) an electron on orbital α and $\sigma^i_{\alpha\beta}$ is a Pauli matrix. We will choose an appropriate fictitious energy $\lambda_{\rm ps}$ to prevent the system from double occupancy. Δ is the energy splitting between the two levels and Δ_0 is the tunneling rate, as shown in Fig. 3.5(a). By a rotation of the spin axis, this system can be diagonalized and the gap between the two eigenstates is $E = \sqrt{\Delta_0^2 + \Delta^2}$.

As the parent compounds are actually metallic, there should be itinerant electrons present besides these localized states. These two can be coupled as in the framework of the localized-itinerant dichotomous models [95, 96, 97, 182]. The starting Hamiltonian is [183, 184, 185]

$$H = H_e + H_{\rm TLS} + V \tag{3.30}$$

$$H_e = \sum_{k\sigma} E_k c^\dagger_{k\sigma} c_{k\sigma} \tag{3.31}$$

$$V = \sum_i \sum_{k_1\sigma_1, k_2\sigma_2} \sum_{\alpha\beta} c^\dagger_{k_2\sigma_2} V^i_{k_2k_1} c_{k_1\sigma_1}\ a^\dagger_\alpha \sigma^i_{\alpha\beta} a_\beta, \tag{3.32}$$

where H_e, $H_{\rm TLS}$ and V represent the Hamiltonians for the itinerant electrons, the single two-level system and the interactions between the two, respectively. There are two kinds of scattering processes as shown in Fig. 3.5(b). One is the diagonal scattering described by the V^z term, where the localized state remains on the same level. The other is the off-diagonal scattering initiated by the V^x term, where the localized state jumps onto the other level. V^y is in fact zero, as it breaks time-reversal symmetry. However, it should be noted that $V^y = 0$ does not hold for the renormalized vertex, since higher order terms are not necessarily

local. We will also assume $V^z \gg V^x$ as proposed previously [183, 184, 185].

In fact, this system is very similar to the Kondo model, with the two orbitals d_{xz} and d_{yz} representing the up and down-spin states on the magnetic impurity. We are going to perform a similar scaling analysis following Ref. [183, 184, 185]. We define the dimensionless couplings $v^i_{k_1k_2} = V^i_{k_1k_2}N_0$ where N_0 is the density of states at the Fermi level. Reducing the bandwidth from D_0 to D and evaluating the vertex corrections up to the leading order, we have the scaling equations

$$\frac{\partial v^s_{\alpha\beta}(u)}{\partial u} = -2i\sum_{ij}\sum_{\gamma}\epsilon^{ijs}v^i_{\alpha\gamma}(u)v^j_{\gamma\beta}(u) \tag{3.33}$$

where $v^i_{\alpha\beta}$ are defined as $v^i_{k_1k_2} = \sum f^\dagger_\alpha(\hat{k_1})v_{\alpha\beta}f_\beta(\hat{k_2})$, with $f_\alpha(\hat{k})$ being a complete set of spherical harmonics, $f_\alpha(\hat{k}) = i^l Y^m_l(\theta_k, \phi_k)$, ϵ^{ijs} is the Levi-Civita symbol and $u = \ln(D/D_0)$. We can express $v^i_{\alpha\beta}$ using the Pauli matrices as $v^i_{\alpha\beta} = v^i\sigma^i_{\alpha\beta}$. Then the above scaling equations will be reduced to a set of coupled equations involving v^x, v^y and v^z. These equations can be solved by separating u into two regimes: (a) $v^y < v^x \ll v^z$ and (b) $v^y \simeq v^x < v^z$. In regime (a), the solutions are

$$v^x(u) = v^x(0)\cosh\left[4v^z(0)u\right] \tag{3.34}$$

$$v^y(u) = v^x(0)\sinh\left[4v^z(0)u\right] \tag{3.35}$$

$$v^z(u) = v^z(0). \tag{3.36}$$

In regime (b), we have

$$\left[v^z(u)\right]^2 - \left[v^x(u)\right]^2 = v_0^2, \tag{3.37}$$

where v_0 is scale invariant and $v^z(u)$ satisfies

$$u = -\frac{1}{4v^z(u)} + \ln\left[\frac{D_0}{k_{\rm B}T_{\rm K}}\right] \tag{3.38}$$

with the Kondo temperature $T_{\rm K}$ identified as

$$k_{\rm B}T_{\rm K} = D_0\left[\frac{v^x(0)}{4v^z(0)}\right]^{1/4v^z(0)}. \tag{3.39}$$

Using the parameters $v^z(0) = 0.33$, $v^x(0)/v^z(0) = 0.001$, $v^y(0) = 0$ and $D_0 = 665\,{\rm K}$ [186], we obtained the scaling flows of v^x, v^y and v^z shown in Fig. 3.6(a), for $E = 0\,{\rm K}$. The corresponding Kondo temperature is $T_{\rm K} = 1.24\,{\rm K}$. Reducing the bandwidth D, the system goes from weak to strong coupling. The resistivity due to the scattering of the two-level system can be calculated based on these renormalized vertices as in Ref. [186]. At high temperature, we have two degenerate levels, d_{xz} and d_{yz}. When the temperature is reduced, the scattering

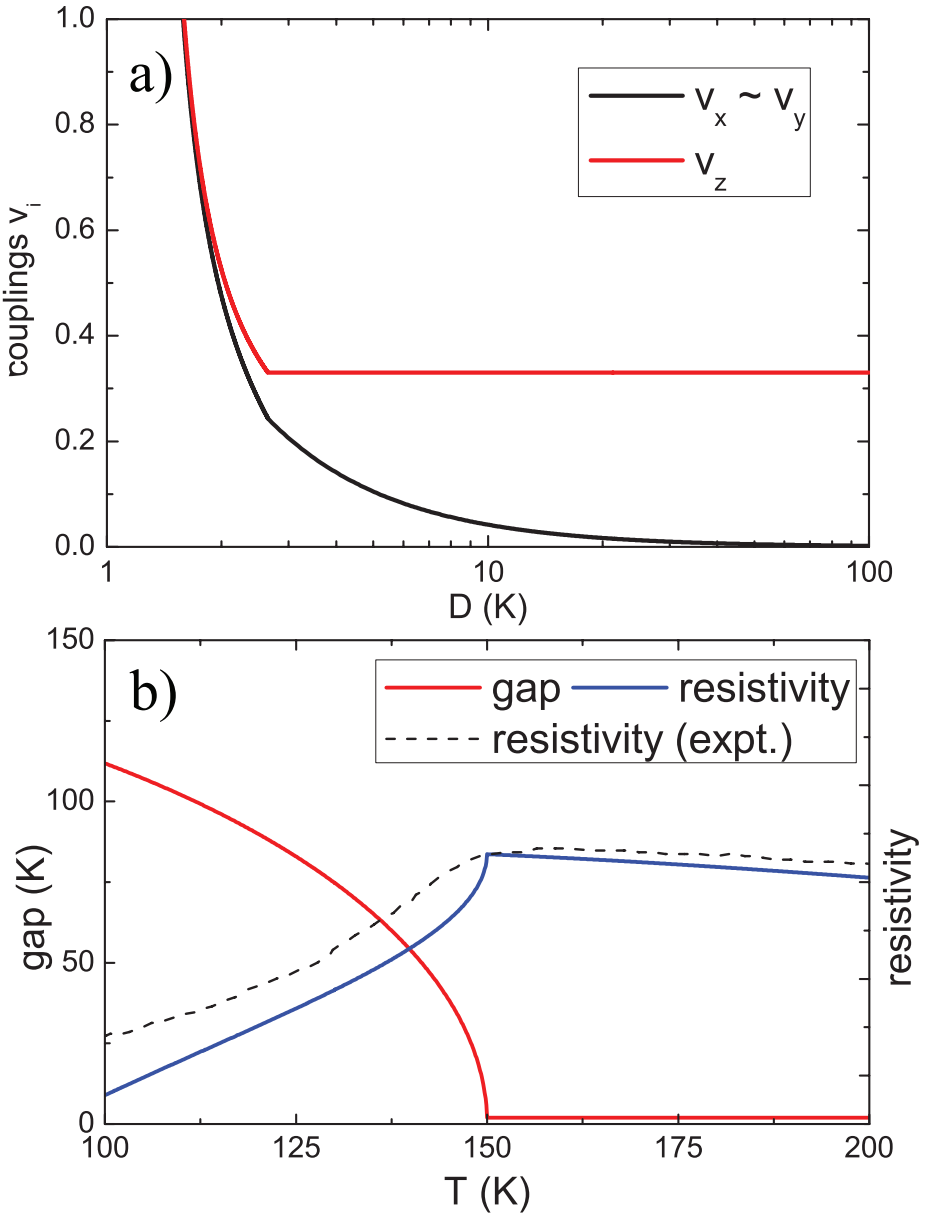

Figure 3.6: (a) Scaling of the coupling constants v^i with respect to bandwidth D. (b) Energy gap and resistivity as a function of temperature T. (The experimental data of resistivity are extracted from Ref. [176].) Setting the resistivity at $T = 150K$ of our model equal to that of the experiment was the only fitting parameter.

from the states closer to the chemical potential increases, leading to a resistivity upturn of $\log T$ [187] as in the Kondo model. However, upon the onset of the SPT, a gap opens between the two levels. If the bandwidth D is less than the gap E, the off-diagonal scattering is not allowed, since there are no states for the electrons to be scattered into. As a consequence, the scaling terminates at $D = E$. The electrons within the bandwidth E will no longer contribute to the resistivity. This is the mechanism behind the resistivity anomaly. Our result is shown in Fig. 3.6(b), which is in good qualitative agreement with experiment. We set the tunneling rate $\Delta_0 = 2\,\mathrm{K}$, and the energy splitting takes the form

$$\Delta(T) = \Delta(0)\sqrt{1 - \left(\frac{T}{T_S}\right)^2} \tag{3.40}$$

where $\Delta(0) = T_S = 150\,\mathrm{K}$ when $T < T_S$. It should be noted that the overall behavior of the scaling flows and the resistivity are independent of the chosen parameters. This represents the explanation of the RA for the iron pnictides.

3.2.4 Orbital driven magnetism

Our model also offers a natural solution to the observed stripe-like antiferromagnetism. Before the SPT, we have an orbitally disordered state, in which the neighboring sites are occupied probabilistically by different orbitals. The resultant lack of overlap gives rise to a vanishing of any antiferromagnetic spin exchange and as a consequence no spin order. After the SPT, either d_{xz} or d_{yz} orbitals will dominate. Without loss of generality, we suppose that most sites are occupied by d_{yz}, as shown in Fig. 3.4(b). Due to the larger overlap of the wave functions on neighboring sites in the y-direction than that in the x-direction, the hopping integral t_b should be larger than t_a. For the nearest-neighbor spin exchange, $J_1 \sim t^2/U$, we have that $J_{1a} < J_{1b}$. So the spins on the longer axis have a stronger tendency to be aligned oppositely. The spin configuration AFM2(b) in Fig. 3.7 is not favored. As has been suggested [84, 178], we can further introduce a next-nearest-neighbor exchange J_2. If $J_2 > J_{1a}/2$, which is very likely for a relatively small J_{1a} [158], AFM2(a) will have a lower energy than AFM1, as shown in Fig. 3.7, and emerge as the ground state at low temperature, which has already been confirmed by the experiments [21]. In contrast with other theories in which the SPT is induced by the spin degrees of freedoms, on this account, the formation of the SDW is actually a result of the ferro-orbital ordering accompanying the SPT.

In fact, we are able to construct a universal Hamiltonian describing both the

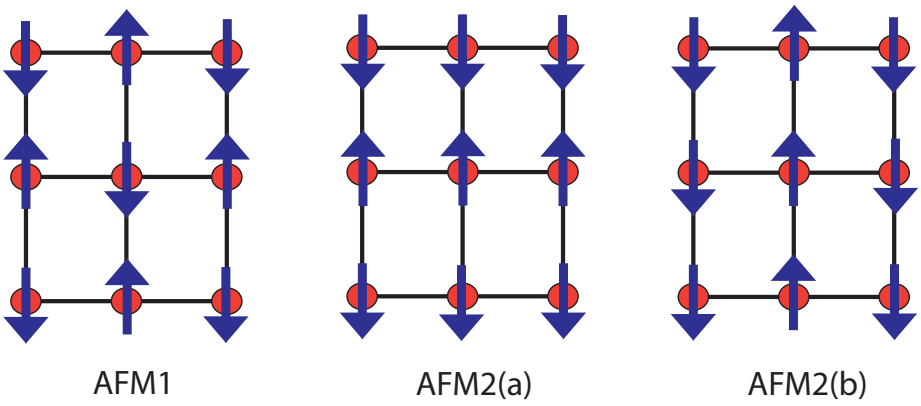

Figure 3.7: Different possible spin configurations on a distorted lattice with $a < b$, which corresponds to the case that d_{yz} is the majority orbital.

SPT and SDW, with a spin-orbital coupling model [158, 164, 180],

$$\begin{aligned} H_{\mathrm{SO}} &= J_S \sum_{\langle i,j\rangle} M_i M_j + \sum_{\langle\langle i,j\rangle\rangle} J_2\left(M_i, M_j\right) \boldsymbol{S}_i \cdot \boldsymbol{S}_j \\ &+ \sum_i J_{1x}\left(M_i, M_{i+\hat{x}}\right) \boldsymbol{S}_i \cdot \boldsymbol{S}_{i+\hat{x}} \\ &+ \sum_i J_{1y}\left(M_i, M_{i+\hat{y}}\right) \boldsymbol{S}_i \cdot \boldsymbol{S}_{i+\hat{y}} \end{aligned} \tag{3.41}$$

where the spin exchanges are given by

$$J_{1x}\left(M_i, M_j\right) = \delta_{M_i, M_j}\left(J_{1b}\delta_{M_i,1} + J_{1a}\delta_{M_i,-1}\right) \tag{3.42}$$

$$J_{1y}\left(M_i, M_j\right) = \delta_{M_i, M_j}\left(J_{1a}\delta_{M_i,1} + J_{1b}\delta_{M_i,-1}\right) \tag{3.43}$$

$$J_2\left(M_i, M_j\right) = \delta_{M_i, M_j} J_2 \tag{3.44}$$

where M_i, representing the orbital degrees of freedom, is defined to be ± 1 for d_{xz} and d_{yz} respectively, as in Sec. 3.2.2. Clearly, in this model, the spin order will not occur until the formation of the ferro-orbital ordering at T_S, which is on the order of J_S. Below T_S, the spin degrees of freedom can be described by an anisotropic Heisenberg model, whose transition temperature to the spin-ordered state, T_H, would depend on the spin exchanges, J_{1a}, J_{1b} and J_2. If $T_H < T_S$, we would have two separate second-order transitions, $T_{\mathrm{SDW}} = T_H < T_S$, as in the case of the 1111-family. For the 122-family, which has a shorter Fe-Fe bond length, it is expected this would enhance the spin exchange J, likely leading to $T_H > T_S$. But the SDW will not form before the SPT, since there is no spin exchange until the SPT obtains. So there is only one first-order transition, $T_{\mathrm{SDW}} = T_S$.

Furthermore, this anisotropic Heisenberg model has also been proposed on experimental grounds [81] to fit the spin-wave spectrum seen in the inelastic neutron scattering data. Our theory gives a direct explanation for the observed

anisotropy of magnetic exchanges. Note their results [81] do rely on a negative J_1^a, which is not obtained by our simple model. However, this difficulty can be overcomed by introducing a Hund coupling between these localized spins and itinerant electrons,

$$H_K = -\frac{J_{\rm H}}{2} \sum_{i,\nu\nu'} \boldsymbol{S}_i \cdot c_{i\nu}^\dagger \boldsymbol{\sigma}_{\nu\nu'} c_{i\nu'} \tag{3.45}$$

where $\boldsymbol{\sigma}_{\nu\nu'}$ are the Pauli matrices. The hopping of the itinerant electrons with this Hund coupling will give rise to an effective ferromagnetic coupling [188, 189, 190] between neighboring spins. After taking this into account, we will eventually have the spins on the shorter axis coupled ferromagnetically. The full details of this model are the subject of a future study.

3.2.5 Final remarks

To conclude, we have proposed that the SPT and RA in the iron pnictides are due to the opening of a gap between two otherwise degenerate orbitals. While our mechanism for the structural phase transition is a standard Jahn-Teller distortion driven by a minimization of the Coulomb repulsion, the key point of this section is that the resulting simple two-level system can resolve the previously unexplained resistivity anomaly. The mechanism proposed here is independent of an applied magnetic field as is seen experimentally [176]. Only in a ferro-orbital-ordered state after the SPT does the stripe-like SDW form. This is the reason why these three phenomena, SPT, RA and SDW, are closely related and almost always coincide with one another. In doped materials, extra electrons or holes will break the uneven occupations of d_{xz} and d_{yz}, thus diminishing the Jahn-Teller effect. So the SPT, RA and SDW will all become less pronounced and shift to lower temperature, eventually vanishing at some critical doping. These are all observed experimentally, lending credence to our model.

After this work was posted on arXiv, several similar papers [172, 191] appeared, based on the same orbital physics we utilized here, which supports our theory that the orbital ordering is the driving mechanism for the SPT, RA and SDW.

Chapter 4

Orbital order from weak coupling[1]

Recent experimental developments in the iron pnictides have unambiguously demonstrated the existence of in-plane electronic anisotropy in the absence of the long-range magnetic order. Such anisotropy can arise from orbital ordering, which is described by an energy splitting between the two otherwise degenerate d_{xz} and d_{yz} orbitals. Including this phenomenological orbital order into a five-orbital Hubbard model, we obtain the mean-field solutions where the magnetic order is determined self-consistently. Despite sensitivity of the resulting states to the input parameters, we find that a weak orbital order that places the d_{yz} orbital slightly higher in energy than the d_{xz} orbital combined with intermediate on-site interactions produces band dispersions that are compatible with the photoemission results. In this regime, the stripe antiferromagnetic order is further stabilized and the resistivity displays the observed anisotropy. We also calculate the optical conductivity and show that it agrees with the temperature evolution of the anisotropy seen experimentally.

4.1 Introduction

In-plane anisotropy plays a prominent role in iron-based superconductors. For example, inelastic neutron scattering (INS) first established that the exchange constant along the ferromagnetic y-direction, J_{1y}, is not only much smaller than the one in the antiferromagnetic x-direction, J_{1x}, but actually slightly negative [81], suggesting an unfrustrated spin model underlies the magnetism. Angle-resolved photoemission spectroscopy (ARPES) also observed a dramatic orbital-dependent Fermi surface reconstruction upon the magneto-structural phase transition [135, 136]. However, due to the fact that the crystals used in such experiments spontaneously form dense domains, the signals from the two diagonal phases were mixed in these early experiments. Hence, it was crucial that scanning tunneling microscopy (STM) detected a quasi-one-dimensional interference pattern [111], thus confirming that the anisotropy arises entirely from a single domain. Helping to complete the story were the breakthrough experiments in which a uniaxial stress was applied to almost fully detwin the crystals [119]. This technique revealed an in-plane anisotropy in both the dc

[1] This chapter is from Ref. [133].

[119, 120, 123, 192] and ac [129, 130, 131] conductivities. Consistent with this transport anisotropy are the band dispersions derived from ARPES measurements on detwinned samples [138].

The observed anisotropies (for a review, see Ref. [108]) have distinct origins in terms of the local-itinerant electron dichotomy [95, 96, 97]. On the one hand, INS measures the spin excitations that arise predominantly from local moments. Although a structural transition precedes or coincides with the onset of the antiferromagnetic order, its magnitude is too small to account for the strong anisotropy. In this context, several theories [158, 159, 172, 173] adopted a Kugel-Khomskii [94] model with orbital dependent superexchanges and proposed that ferro-orbital order stabilizes the $(\pi, 0)$ magnetic order, leading naturally to anisotropic spin couplings. In an alternative approach [103, 104], the local moments, which are governed by an isotropic J_1-J_2 Heisenberg model, are coupled with the itinerant electrons of the two degenerate d_{xz} and d_{yz} orbitals by the Hund exchange. From the double-exchange mechanism, a ferro-orbital order in the itinerant band leads to different corrections to the spin-wave excitations along two diagonal directions, resulting in an anisotropic spin-only model.

On the other hand, the detected anisotropy could simply signify that the itinerant electrons also undergo a phase transition that breaks the C_4 rotational symmetry, which is no surprise since the symmetry is already broken by the underlying $(\pi, 0)$ antiferromagnetism. Although this electronic anisotropy does persist above the Néel temperature, T_N, and the structural transition temperature, T_S, in some experiments [119, 120, 123, 129, 130, 131, 138, 192]. it should be noted that the applied uniaxial stress unfortunately turns the sharp transition into a broad crossover. In this sense, recent INS measurements [100] that observed a spin nematic order in the paramagnetic phase have taught us something new - the magnetic anisotropy, and the possible electronic anisotropy, can exist in the absence of the $(\pi, 0)$ antiferromagnetism and even the structural distortion. This 'nematic' order is indeed confirmed by the band splitting above T_S observed by the latest ARPES experiments on twinned samples [138], and recently hinted by the conductance enhancement in point contact spectroscopy [141].

One theoretical proposal that is in accord with some of the current experimental observations is the J_1-J_2 Heisenberg model,[84] in which an Ising order can occur without long-range magnetic order [145, 146], according to the 'order from disorder without order' mechanism [144]. However, the unfrustrated magnetism observed by INS [81, 100] suggests that the correct physical model lies elsewhere. Another possible candidate is a Kugel-Khomskii spin-orbital model [158] that might support a phase which possesses some orbital order that breaks the C_4 rotational symmetry, but no long-range magnetic order. Besides these strong-coupling approaches, there are other theoretical proposals that attribute the nematic order to interaction-induced instability of the itinerant electrons

[68, 156, 193].

Our particular view which we have enunciated elsewhere [103, 159] is that orbital order (rather than any intrinsic tendency of the electrons to orient themselves inhomogeneously) lies at the heart of the anisotropies and the observed structural and magnetic transitions. Certainly, it is now common [106] to refer to any phase that breaks C_4 symmetry as an electron nematic even when such a phase is lattice or orbitally induced. This view has been scrutinized sharply by recent experiments [194] on the the cuprate superconductor $Bi_2Sr_2Ca_{n-1}Cu_nO_{2n+4+x}$ which indicate that many of the anisotropies that have been viewed as evidence for an electron nematic phase actually originate from lattice effects in the BiO layer. This experiment certainly indicates that caution rather than a rush to nematize is warranted. For the pnictides, the origin of the anisotropies will remain open in the absence of a clear experiment that is able to discern their efficient cause. Consequently, our usage of the term nematic here strictly entails the orbital order which necessarily breaks the equivalence between the canonical x and y axes.

In this chapter, we will not focus on the origin of this 'nematic' order (in the sense defined above), but rather investigate its experimental consequences, by modeling it phenomenologically as an energy-splitting term between the Fe d_{xz} and d_{yz} orbitals. This type of orbital nematic order has been studied previously [132], but only in the context of an orbital-independent magnetic order, which is insufficient to capture the complicated electronic structure. To this end, we will start with the multi-orbital model that explicitly includes this orbital nematic order and solve the mean-field Hamiltonian using a self-consistent procedure. In this approach, the magnetic order on different orbitals will be determined more realistically by the band structure and the interaction strength. Moreover, we will be able to address how the orbital and magnetic orders interplay with one another. To reach agreement with photoemission experiments [138], we find that the d_{xz} orbital is placed lower in energy than d_{yz}, and that this orbital order strengthens the stripe antiferromagnetism. The orbital and magnetic order together reconstruct the band structure and result in the anisotropy at both the low-temperature antiferromagnetic and the high-temperature paramagnetic phase. These findings suggest that orbital order plays the central role in the electronic structure of the iron-based superconductors.

This chapter is organized as follows. The general formalism of the multi-orbital model is described in Sec. 4.2. We introduce the orbital nematic order in Sec. 4.3 and calculate its experimental consequences that are relevant for anisotropy in the paramagnetic phase. Sec. 4.4 presents the complicated electronic structure arising from both the orbital and magnetic orders. It is shown that both of them are indispensable components that lead to anisotropies observed by many experiments in the magnetically ordered state. Implications of our findings are discussed in the last section.

4.2 Multi-orbital model

The multi-orbital Hamiltonian we start with is usually defined within an extended Brillouin zone that only contains one Fe atom per unit cell. The kinetic energy contribution is written as

$$\mathcal{H}_K = \sum_{\alpha\beta} \sum_{\tilde{\boldsymbol{k}}\mu} \hat{\xi}_{\alpha\beta}(\tilde{\boldsymbol{k}}) c^{\dagger}_{\tilde{\boldsymbol{k}}\alpha\mu} c_{\tilde{\boldsymbol{k}}\beta\mu}, \tag{4.1}$$

where $c^{\dagger}_{\tilde{\boldsymbol{k}}\alpha\mu}$ creates an electron of momentum $\tilde{\boldsymbol{k}}$ on orbital α with spin μ ($\mu = \uparrow, \downarrow$). We note here $\tilde{\boldsymbol{k}}$ is not the crystal momentum, $\boldsymbol{k}$, defined by the translation operator $\mathcal{T}_i$ of the Fe lattice unit vector e_i ($i = x, y, z$): $\mathcal{T}_i|\boldsymbol{k}\rangle = e^{ik_i}|\boldsymbol{k}\rangle$. Rather, it is the operator $\mathcal{P}_z\mathcal{T}_i$, where $\mathcal{P}_z$ is the reflection operator in the z-direction, instead of $\mathcal{T}_i$, that leaves the Fe-As lattice invariant. Thus $\tilde{\boldsymbol{k}}$ actually labels the eigenstates of $\mathcal{P}_z\mathcal{T}_i$: $\mathcal{P}_z\mathcal{T}_i|\tilde{\boldsymbol{k}}\rangle = e^{i\tilde{k}_i}|\tilde{\boldsymbol{k}}\rangle$ and yields an unambiguous way to unfold the real Brillouin zone with two Fe atoms per unit cell. This important distinction between $\tilde{\boldsymbol{k}}$ and $\boldsymbol{k}$ was previously discussed in detail by Ref. [40]. In principle, we need to fold back the band dispersions that are obtained by the diagonalization of $\mathcal{H}_K$(4.1), and fit them to the local-density-approximation (LDA) calculations by tuning the tight-binding hopping parameters. This has been done in many studies, using two [41, 42, 43], three [40, 44], four [45], or five [46, 47, 48, 49, 50, 51] Fe d-orbitals. In order to make our calculations more realistic, we only focus on the five-orbital model, particularly the one of Ref. [50], which is based on a three-dimensional fitting to the LDA band structures of $BaFe_2As_2$, the material on which most of the experiments are performed.

It is helpful for us to return to real space where $\mathcal{H}_K$(4.1) takes the form $\mathcal{H}_K = \sum t^{\alpha\beta}_{ij} c^{\dagger}_{i\alpha\mu} c_{j\beta\mu}$, where $t^{\alpha\beta}_{ij}$ is the hopping amplitude with i, j denoting the index of the site. As discussed, the operator $\mathcal{P}_z\mathcal{T}_i$ leaves $\mathcal{H}_K$ invariant. Under $\mathcal{P}_z\mathcal{T}_i$, we have $c_{i\alpha\mu} \to \chi_\alpha c_{i+e_i,\alpha\mu}$ where $\chi_\alpha = 1$ for $\alpha = d_{xy}$, $d_{x^2-y^2}$, or $d_{3z^2-r^2}$ and $\chi_\alpha = -1$ for $\alpha = d_{xz}$ or d_{yz}. Thus, it is required that $t^{\alpha\beta}_{ij} = t^{\alpha\beta}_{i-j}$ for $\chi_\alpha\chi_\beta = 1$, whereas $t^{\alpha\beta}_{ij} = e^{i\boldsymbol{K}\cdot\boldsymbol{r}_i} t^{\alpha\beta}_{i-j}$ for $\chi_\alpha\chi_\beta = -1$, where $\boldsymbol{K} = (\pi, \pi, \pi)$ and $t^{\alpha\beta}_{i-j}$ only depends on $\boldsymbol{r}_i - \boldsymbol{r}_j$. We immediately noticed that in the crystal momentum space, the electron operators of the d_{xz} and d_{yz} orbitals at $\boldsymbol{k}$ are coupled with those of d_{xy}, $d_{x^2-y^2}$, and $d_{3z^2-r^2}$ at $\boldsymbol{k} + \boldsymbol{K}$. As a result, we define the pseudocrystal momentum $\tilde{\boldsymbol{k}}$ as follows, $c_{\tilde{\boldsymbol{k}}\alpha\mu} = c_{\boldsymbol{k}\alpha\mu}$ for $\alpha = d_{xz}$ or d_{yz} and $c_{\tilde{\boldsymbol{k}}\alpha\mu} = c_{\boldsymbol{k}+\boldsymbol{K},\alpha\mu}$ for $\alpha = d_{xy}$, $d_{x^2-y^2}$, or $d_{3z^2-r^2}$ [40, 45, 48]. It is in this pseudocrystal momentum $\tilde{\boldsymbol{k}}$ space that the kinetic energy $\mathcal{H}_K$ takes the diagonal form of $\mathcal{H}_K$ (4.1).

The distinction between $\tilde{\boldsymbol{k}}$ and $\boldsymbol{k}$ has immediate consequences for the interpretation of the ARPES measurements. The momentum probed by ARPES is not $\tilde{\boldsymbol{k}}$, but $\boldsymbol{k}$. Because the crystal momentum $\boldsymbol{k}$ is not a good quantum number of $\mathcal{H}_K$ (4.1), ARPES detects both bands with momentum $\tilde{\boldsymbol{k}}$ and $\tilde{\boldsymbol{k}} + \boldsymbol{K}$, corresponding to folding the Brillouin zone with one Fe atom per unit cell by a wave vector $\boldsymbol{K} = (\pi, \pi, \pi)$. This observation is consistent with the fact that the

real unit cell including the As atoms consists of two Fe atoms. However, the relative intensity of each band measured by ARPES depends on the strengths of hybridizations between $\boldsymbol{k}$ and $\boldsymbol{k}+\boldsymbol{K}$.

Formally the Green function in terms of $\tilde{\boldsymbol{k}}$ is defined as

$$\hat{\mathcal{G}}_{\alpha\beta}(\tilde{\boldsymbol{k}},\tau) = -\left\langle T_\tau c_{\tilde{\boldsymbol{k}}\alpha\mu}(\tau) c^\dagger_{\tilde{\boldsymbol{k}}\beta\mu}(0)\right\rangle, \tag{4.2}$$

with its Fourier transform satisfying $\hat{\mathcal{G}}^{-1}(\tilde{\boldsymbol{k}},\omega) = \omega\hat{I} - \hat{\xi}(\tilde{\boldsymbol{k}})$. We can simply write down the spectral function

$$A(\tilde{\boldsymbol{k}},\omega) = -\frac{1}{\pi}\Im\left[\mathrm{tr}\,\hat{\mathcal{G}}(\tilde{\boldsymbol{k}},\omega+i\delta)\right]. \tag{4.3}$$

However what is really measured by ARPES is not $A(\tilde{\boldsymbol{k}},\omega)$, but

$$\begin{aligned} A(\boldsymbol{k},\omega) &= -\frac{1}{\pi}\Im\left[\sum_{\chi_\alpha=-1}\hat{\mathcal{G}}_{\alpha\alpha}(\tilde{\boldsymbol{k}},\omega+i\delta)\right. \\ &\quad \left. + \sum_{\chi_\alpha=1}\hat{\mathcal{G}}_{\alpha\alpha}(\tilde{\boldsymbol{k}}+\boldsymbol{K},\omega+i\delta)\right]. \end{aligned} \tag{4.4}$$

It is this function on which we will focus.

In Fig. 4.1(a) and (b), we plot $A(\tilde{\boldsymbol{k}},\omega=0)$, depicting the Fermi surfaces in the plane of $\tilde{k}_z = 0$ and $\tilde{k}_z = \pi$, respectively. Those of $A(\boldsymbol{k},\omega=0)$ are shown in Fig. 4.1(c) and (d). The frequency ω is defined with respect to the chemical potential μ, which is determined by the electron filling level $n = 6$, dictated by the Fe valence in the parent compounds. In addition, all the energy scales have an implicit unit of eV in the whole chapter. Comparing these graphs, we find that $A(\boldsymbol{k},\omega)$ displays a more complicated structure due to the folding of Brillouin zone. From now on we will only focus on $A(\boldsymbol{k},\omega)$, which is measured by ARPES in our direct comparison with experiments. Furthermore in Fig. 4.2(a), $A(\boldsymbol{k},\omega)$ is plotted along the line X-Γ-X with $X = (\pi,0,0)$ and $\Gamma = (0,0,0)$, to represent the band dispersions probed by unpolarized ARPES. Experimentally the orbital character can be investigated by tuning the polarization of the incoming light. For example, using a polarization perpendicular to the incident plane only selects those orbitals that are odd under $\mathcal{P}_y$ (d_{yz} and d_{xy}) along the line of X-Γ-X. We plot these orbital-polarized dispersions in Fig. 4.2(b), which shows qualitative agreement with experiments [138]. Since the C_4 rotational symmetry is respected, the dispersions are exactly the same along the crystal momentum line Y-Γ-Y where $Y = (0,\pi,0)$, with no splitting between the bands at X and Y.

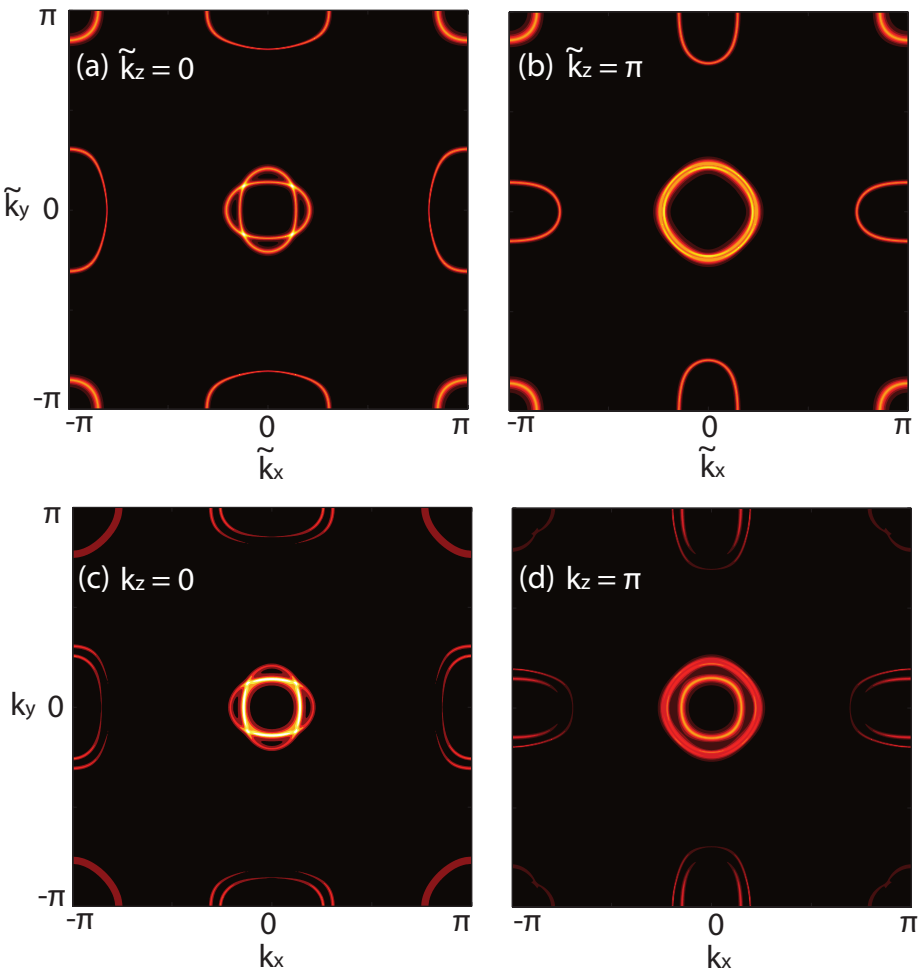

Figure 4.1: Fermi surfaces in terms of (a,b) the pseudocrystal momentum $\tilde{\boldsymbol{k}}$ and (c,d) the crystal momentum $\boldsymbol{k}$. We plot the Fermi surfaces in the xy-plane and set the z-component in each figure to (a) $\tilde{k}_z = 0$, (b) $\tilde{k}_z = \pi$, (c) $k_z = 0$, and (d) $k_z = \pi$. We represent the values of the spectral function $A(k, \omega)$ by the color scale, which is used consistently for all the figures in this chapter.

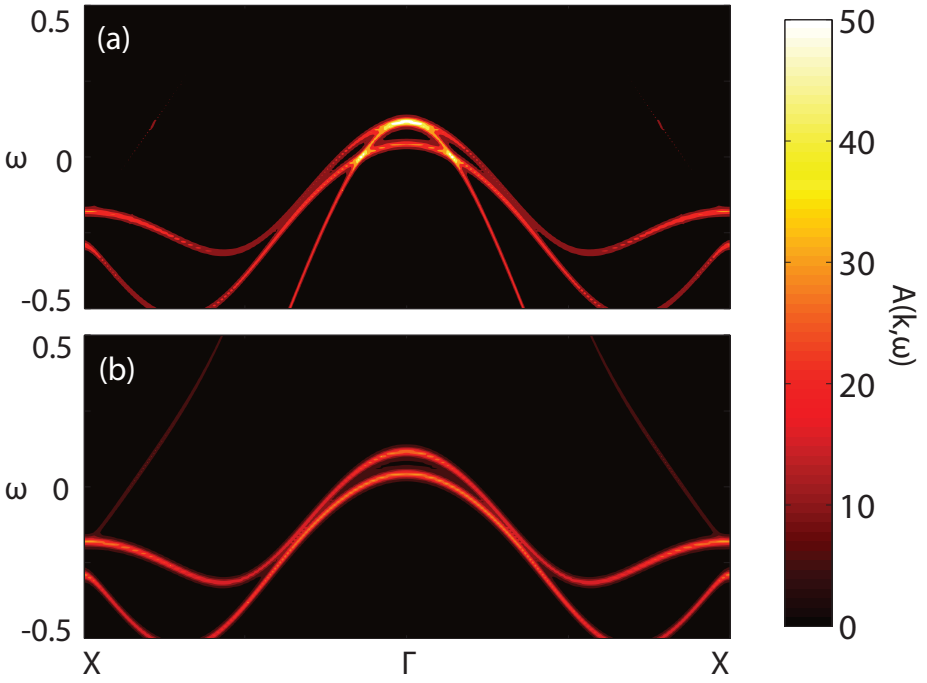

Figure 4.2: (a) Unpolarized dispersions and (b) polarized dispersions along the crystal momentum line of X-Γ-X. In (b) only the components of the d_{yz} and d_{xy} orbitals are shown.

4.3 Orbital nematic order

As discussed in Sec. 4.1, electronic anisotropy has been confirmed by recent experiments [100, 138] to persist above the magneto-structural transition. Our take on this is that this effect is due entirely to orbital ordering. To test out this hypothesis, we introduce the orbital nematic order as an energy-splitting term between the d_{xz} and d_{yz} orbitals,

$$\mathcal{H}_N = \sum_{i\alpha\mu} \Delta_\alpha c^\dagger_{i\alpha\mu} c_{i\alpha\mu}, \tag{4.5}$$

where $\Delta_\alpha = \pm\Delta$ for $\alpha = d_{xz}$ and d_{yz}, respectively, and $\Delta_\alpha = 0$ for the other three orbitals. In principle, all the five orbitals should be involved in this nematic order. But we will only consider the d_{xz} and d_{yz} orbitals due to their spatial anisotropy, whereas the other three orbitals are dropped because they are C_4 rotationally symmetric. It needs to be emphasized that $\mathcal{H}_N$ (4.5) represents an electron nematic order which occurs without the onset of the long-range stripe antiferromagnetism. We find that in order to produce results that are consistent with ARPES measurements [138], the orbital nematic order parameter Δ is required to have a small negative value, which leads to a higher energy of d_{yz} relative to d_{xz}. For the purpose of illustration, we choose $\Delta = -0.08$, and plot the resulting Fermi surfaces and polarized dispersions in Fig. 4.3.

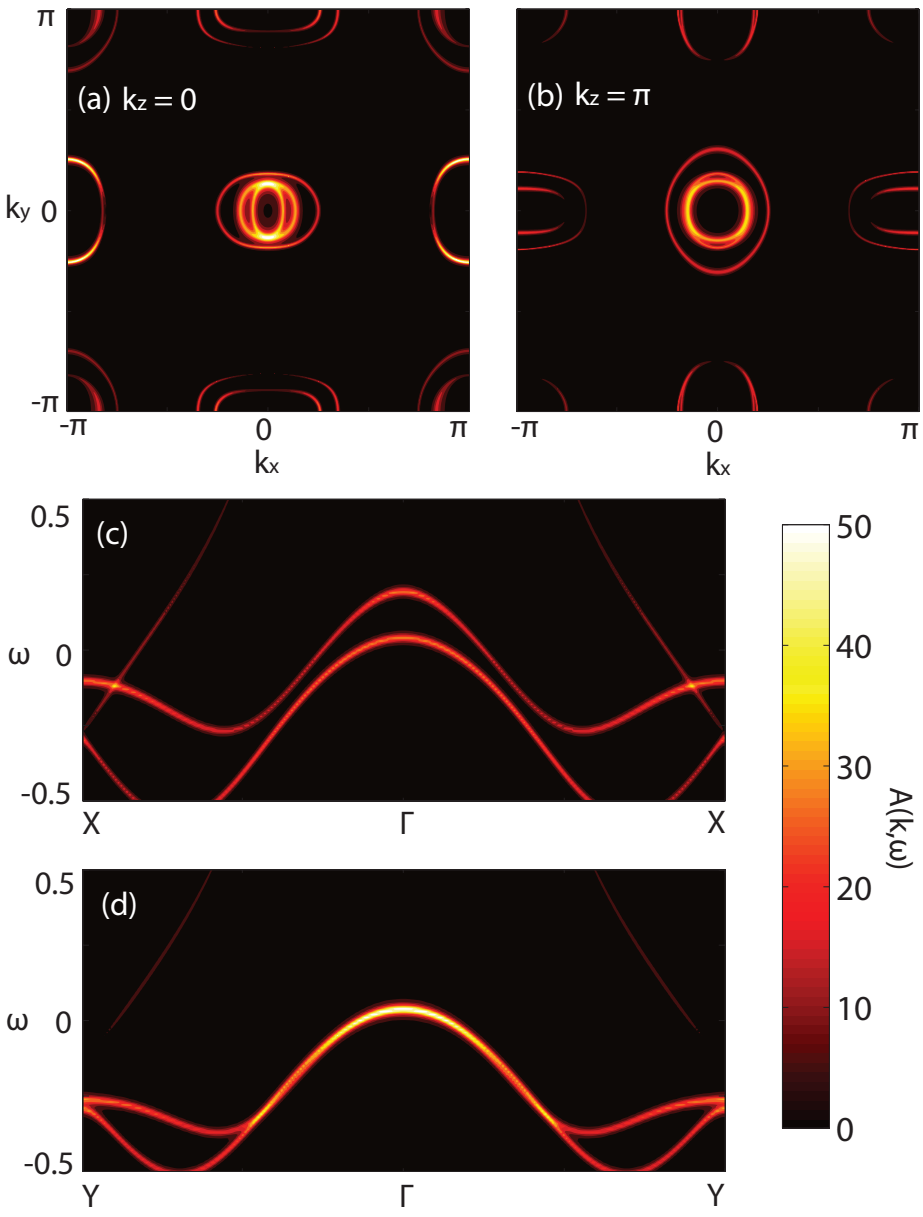

Figure 4.3: (Color online) Fermi surfaces in the plane for (a) $k_z = 0$ and (b) $k_z = \pi$. Polarized dispersions along the line of (c) X-Γ-X and (d) Y-Γ-Y. We have set the orbital nematic order parameter $\Delta = -0.08$, explicitly breaking C_4 symmetry.

From Fig. 4.3(a) and (b), we notice that the hole pockets at the zone center are deformed into elliptical shapes that are elongated along the x- and y-direction in the plane of $k_z = 0$ and $k_z = \pi$, respectively. The apparent breaking of C_4 symmetry is indeed a direct consequence of $\mathcal{H}_N$ (4.5) that is explicitly introduced by hand. However, this orbital order does have a physically reasonable origin which can be explained as follows. From a weak-coupling point of view, the observed magnetic order with wave vector $\boldsymbol{q} = (\pi, 0, \pi)$ arises from the nesting instability between the hole pockets centered at $\tilde{\boldsymbol{k}} = (0, 0, \tilde{k}_z)$ and the electron pockets at $\tilde{\boldsymbol{k}} = (\pi, 0, \tilde{k}_z + \pi)$. But the nesting is not perfect, because the hole pockets are more circular, whereas the electron pockets are more elliptical [see Fig. 4.1(a) and (b)]. By the inclusion of $\mathcal{H}_N$ (4.5) with a small negative Δ, the hole pockets are deformed into ellipses whereas the electron pockets are relatively less affected, thus resulting in a better nesting condition between the two by the wave vector $\boldsymbol{q}$ [see Fig. 4.3(a) and (b)]. Consequently, this type of orbital order will naturally arise in the system and provide further stabilization of the antiferromagnetism. Our result is consistent with the Pomeranchuk instability from the functional renormalization-group studies [68].

The polarized dispersions along the x- and y-direction are displayed in Fig. 4.3(c) and (d), respectively. It needs to be emphasized that only the spectral functions of d_{yz} and d_{xy} orbitals are shown in Fig. 4.3(c) whereas we only plot those of d_{xz} and d_{xy} in Fig. 4.3(d), which are exactly what are measured by the polarized ARPES setup [138]. Indeed a small negative Δ, which lifts d_{yz} higher than d_{xz} in energy, produces splitting between the bands at X and Y, in agreement with experimental observations.

To further examine the validity of the orbital order term $\mathcal{H}_N$ (4.5), we turn to its experimental consequences in transport measurements by calculating the optical conductivity $\sigma_{xx}(\omega)$ and $\sigma_{yy}(\omega)$ along the x- and y-direction, respectively. When $\Delta = 0$, σ_{xx} and σ_{yy} are completely equivalent [Fig. 4.4(a)], preserving the C_4 symmetry. We see a sharp Drude peak accompanied by some high-energy features due to inter-band transitions. If a small negative $\Delta = -0.08$ is turned on, $\sigma(\omega)$ along two diagonal directions become distinct and a low-energy sub-peak emerges around $\omega_1 \approx 0.2$, where σ_{yy} has a value larger than σ_{xx} as depicted in Fig. 4.4(b). We also notice that around the high-energy peak at $\omega_2 \approx 0.7$, σ_{xx} is dominant instead. These results are in good agreement with experiments [130] performed above T_N in the detwinned samples.

We also compare the Drude weight of σ_{xx} and σ_{yy} and plot their ratio as a function of Δ. As shown in the inset of Fig. 4.4(a), when the energy splitting Δ gets larger, $\sigma_{xx}(0)/\sigma_{yy}(0)$ almost monotonically decreases, resulting in a larger Drude weight along the y-direction. If we naively assume proportionality between the Drude weight and the dc conductivity, this result contradicts experimental findings in which the antiferromagnetic x-direction always has a higher conductivity [119] than the ferromagnetic y-direction. However, as pointed out by optical measurements [130], the Drude weight does obtain a higher value

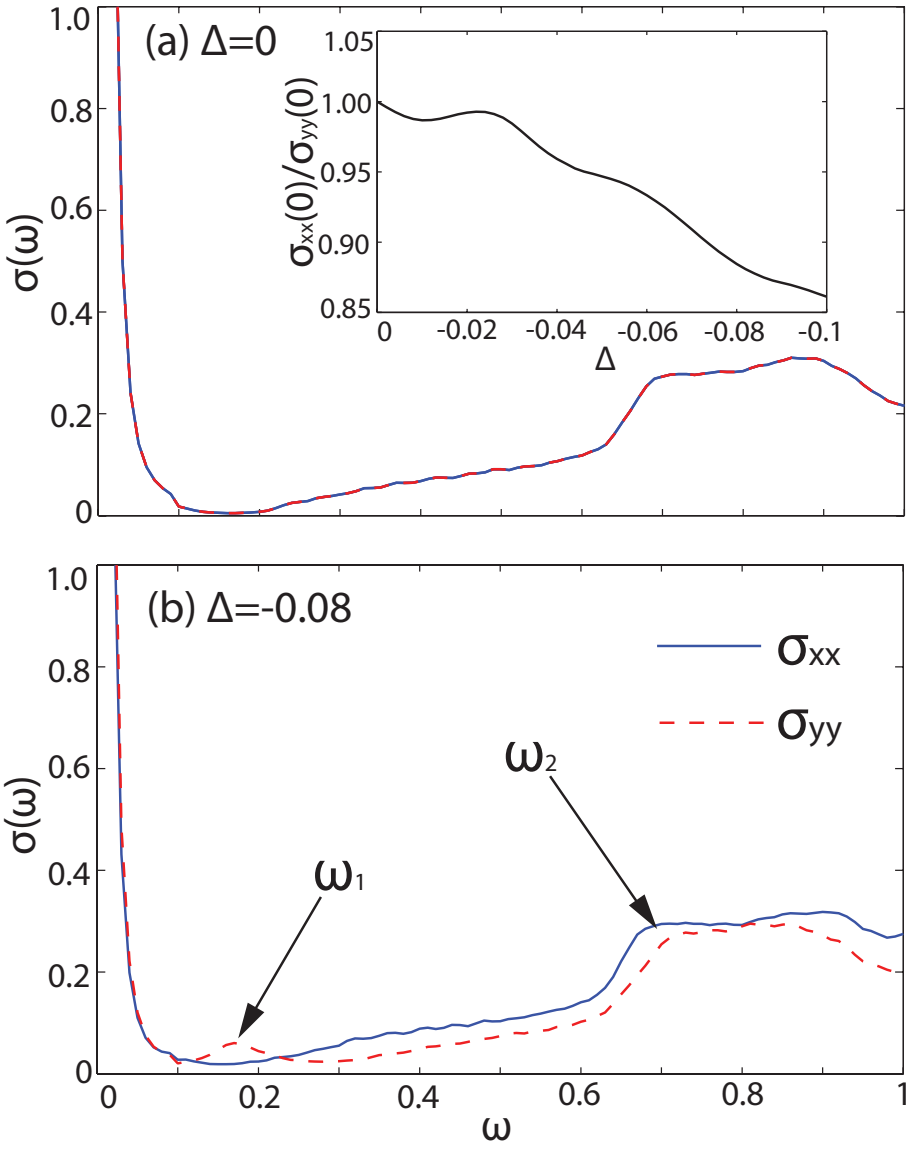

Figure 4.4: Optical conductivity σ_{xx} and σ_{yy} as a function of the frequency ω for the orbital nematic order parameter (a) $\Delta = 0$ and (b) $\Delta = -0.08$. The inset of (a) displays the ratio of the Drude weight, $\sigma_{xx}(0)/\sigma_{yy}(0)$, as a function of Δ. $\sigma(\omega)$ is plotted in an arbitrary unit, which is kept the same in this chapter. The two arrows in (b) denote the two characteristic frequencies $\omega_1 \approx 0.2$ and $\omega_2 \approx 0.7$ where $\sigma(\omega)$ exhibits a peak structure.

along the y-direction, and it is the scattering rate difference that dictates the higher conductivity along the x-direction. In this regard, to obtain the correct anisotropy of the dc conductivity, we need to take into account some anisotropic scattering mechanism, for example, a short-range $(\pi, 0, \pi)$ magnetic order which is supported by the recent INS experiment [100]. Indeed this correct anisotropy of the scattering rate is obtained by a recent theory [122] that considers scattering by anisotropic spin fluctuations in the paramagnetic phase. It should also be mentioned that our result of the Drude weight agrees with earlier studies [132] based on the same form of the orbital order but using a different five-orbital tight-binding model [47].

In conclusion, our study shows that orbital order plays an important role in modifying the electronic structure as well as $\sigma_{xx}(0)/\sigma_{yy}(0)$, the ratio of the Drude weights above the onset temperature for long-range magnetic order. In this way, we have separated the physics that results from magnetic as opposed to orbital order.

4.4 Magnetic order

Now we set out to include magnetic order. At the mean-field level, magnetic order can be described by

$$\mathcal{H}_{AF} = \sum_{\alpha\beta} M_{\alpha\beta} \sum_{i} e^{i\boldsymbol{q}\cdot\boldsymbol{r}_i} \sigma^z_{\mu\nu} c^\dagger_{i\alpha\mu} c_{i\beta\nu} \tag{4.6}$$

for a multi-orbital system, where we have chosen the ordering wave vector $\boldsymbol{q} = (\pi, 0, \pi)$ and the spins are assumed to point along the S^z direction, with σ^z being the Pauli matrix. For a five-orbital system, the order parameters $M_{\alpha\beta}$ form a 5×5 Hermitian matrix, with a total of 25 independent real variables. However, as discussed in Ref. [42], the $(\pi, 0, \pi)$ magnetically ordered state is invariant under the inversion $\mathcal{I}$ around any Fe site, reflections $\mathcal{P}_x$, $\mathcal{P}_y$, and $\mathcal{P}_z$ along the x, y, and z directions, respectively, and effective time reversal $\mathcal{TR}'$, which is a combination of time reversal and spin reversal, $\mathcal{TR}' = \mathcal{TR} \circ \mathcal{SR}$. Under these symmetries in our five-orbital system, only six parameters acquire non-zero real values: $M_{\alpha\alpha}$ ($\alpha = d_{xz}, d_{yz}, d_{xy}, d_{x^2-y^2}, d_{3z^2-r^2}$) and $M_{\alpha\beta} = M_{\beta\alpha}$ ($\alpha = d_{x^2-y^2}$, $\beta = d_{3z^2-r^2}$). Hence, magnetic order obtains almost exclusively within the same orbitals, with the only exception being the orbital-off-diagonal term between the $d_{x^2-y^2}$ and $d_{3z^2-r^2}$ orbitals.

Following these discussions, we consider the on-site interaction of a multi-

orbital Hubbard model,

$$\begin{aligned}\mathcal{H}_I &= \frac{U}{2}\sum_{i,\alpha,\mu\neq\nu}\hat{n}_{i\alpha\mu}\hat{n}_{i\alpha\nu}+\frac{V}{2}\sum_{i,\alpha\neq\beta,\mu\nu}\hat{n}_{i\alpha\mu}\hat{n}_{i\beta\nu}\\ &+\frac{J}{2}\sum_{i,\alpha\neq\beta,\mu\nu}c^{\dagger}_{i\alpha\mu}c^{\dagger}_{i\beta\nu}c_{i\alpha\nu}c_{i\beta\mu}\\ &+\frac{J'}{2}\sum_{i,\alpha\neq\beta,\mu\neq\nu}c^{\dagger}_{i\alpha\mu}c^{\dagger}_{i\alpha\nu}c_{i\beta\nu}c_{i\beta\mu}, \end{aligned} \tag{4.7}$$

where $\hat{n}_{i\alpha\mu}=c^{\dagger}_{i\alpha\mu}c_{i\alpha\mu}$. We still assume $U=V+2J$ and $J=J'$, which is not necessarily valid as the orbitals used here only share the same symmetry but do not have exactly the identical form of the atomic d-orbitals. We make use of the standard mean-field decoupling,

$$\left\langle c^{\dagger}_{i\alpha\mu}c_{i\beta\nu}\right\rangle=\frac{1}{2}\left(n_\alpha+\mu m_\alpha e^{i\boldsymbol{q}\cdot\boldsymbol{r}_i}\right)\delta_{\alpha\beta}\delta_{\mu\nu}, \tag{4.8}$$

where $\mu=\pm1$ for up and down spins, respectively. As shown by LDA calculations [50], the Fermi surfaces are mostly composed of the t_{2g} orbitals (d_{xz}, d_{yz}, and d_{xy}). Thus we can safely ignore the orbital-off-diagonal magnetic order between $d_{x^2-y^2}$ and $d_{3z^2-r^2}$, and use the above orbital-diagonal decoupling which captures five of the total six non-zero mean-field antiferromagnetic order parameters.

By contrast, we point out that in Ref. [46], the orbitals are defined along the axes of the original unit cell, X and Y, which are rotated by 45° from the x and y axes of the Fe lattice. Doing mean-field decoupling of Eq. (4.8) on this model will only take account of four order parameters. Symmetry considerations impose that the orbital-diagonal elements $M_{\alpha\alpha}$ of the d_{XZ} and d_{YZ} orbitals are equal to each other. However, the off-diagonal element $M_{\alpha\beta}=M_{\beta\alpha}$ ($\alpha=d_{XZ}$, $\beta=d_{YZ}$) can acquire non-zero values, but will not be captured by the mean-field theory. Hence we will use the model [50] where the orbitals are defined along the Fe-Fe bond, and expect better results compared to earlier studies [195, 196] based on Ref. [46] under orbital-diagonal mean-field decoupling.

Straightforward calculation yields the mean-field interaction term

$$\begin{aligned}\mathcal{H}_I &= C+\sum_{\boldsymbol{k}\alpha\mu}\Big[\epsilon_\alpha c^{\dagger}_{\boldsymbol{k}\alpha\mu}c_{\boldsymbol{k}\alpha\mu}\\ &+\ \eta_{\alpha\mu}\left(c^{\dagger}_{\boldsymbol{k}\alpha\mu}c_{\boldsymbol{k}+\boldsymbol{q},\alpha\mu}+h.c.\right)\Big], \end{aligned} \tag{4.9}$$

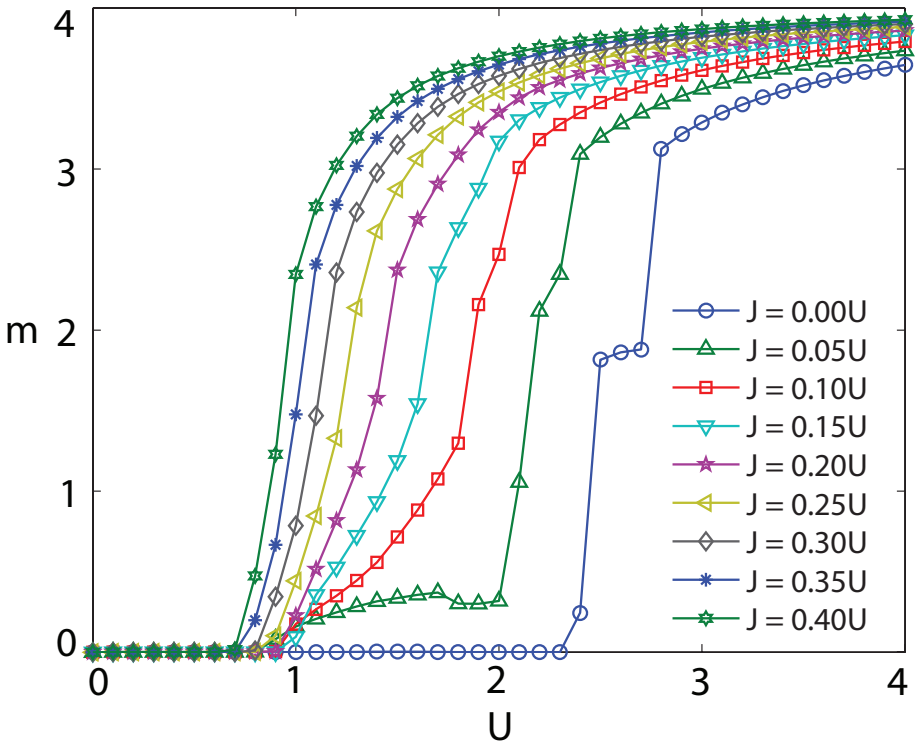

Figure 4.5: The total staggered magnetic moment m as a function of the Coulomb repulsion U for different Hund's exchanges J. We set the energy splitting $\Delta = 0$ in order to find the regime of parameters that are of interest in the context of iron-based superconductors.

where

$$\epsilon_\alpha = \frac{U}{2} n_\alpha + \left(V - \frac{J}{2} \right) \sum_{\beta \neq \alpha} n_\beta, \tag{4.10}$$

$$\eta_{\alpha\mu} = -\frac{\mu}{2} \left(U m_\alpha + J \sum_{\beta \neq \alpha} m_\beta \right), \tag{4.11}$$

and the constant

$$C = -\frac{U}{4} \sum_\alpha \left(n_\alpha^2 - m_\alpha^2 \right) - \frac{2V - J}{4} \sum_{\alpha \neq \beta} n_\alpha n_\beta + \frac{J}{4} \sum_{\alpha \neq \beta} m_\alpha m_\beta. \tag{4.12}$$

Note in $\mathcal{H}_I$ (4.9), $\boldsymbol{k}$ can be simply replaced by $\tilde{\boldsymbol{k}}$ without changing the form of the equation. The full Hamiltonian, $\mathcal{H} = \mathcal{H}_K + \mathcal{H}_N + \mathcal{H}_I$, is quadratic in electron operators $c_{\tilde{\boldsymbol{k}}\alpha\mu}$ and can be solved with order parameters n_α and m_α being determined self-consistently.

So far there is still no systematic mean-field study of this three-dimensional

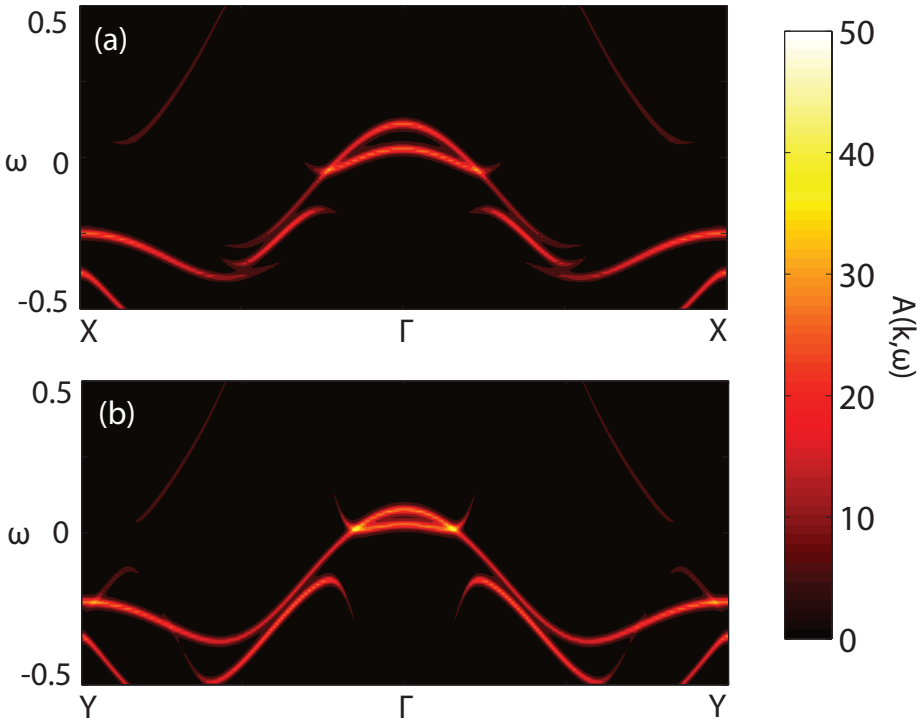

Figure 4.6: Polarized dispersions along (a) X-Γ-X and (b) Y-Γ-Y, for $U = 1.08$, $J = 0.20U$, and $\Delta = 0$. The corresponding magnetic moment $m = 0.46$.

tight-binding model [50] specially constructed for $BaFe_2As_2$. Thus as the first step we need to search for appropriate values of U and J that are consistent with experimental observations. At the outset, we set the orbital nematic order Δ to zero to simplify our calculations. Generally a non-zero Δ produces further modifications, but the physically relevant regime of U and J is not greatly affected by the choice of Δ. In Fig. 4.5, we plot the total staggered magnetic moment $m = \sum_\alpha m_\alpha$ as a function of Coulomb repulsion U for various Hund's couplings J. It is found that there exists a metallic phase with antiferromagnetic order at intermediate Coulomb repulsion U. Furthermore the ratio of J and U also needs to take intermediate values. This requirement of U and J is qualitatively consistent with earlier studies [51, 163] based on other five-orbital models.

For a typical value of $U = 1.08$ and $J = 0.20U$, we plot the polarized dispersions along the two diagonal directions in Fig. 4.6(a) and (b), respectively. Clearly, the magnetic order opens up a gap close to Fermi energy and significantly modifies the original band structure shown in Fig. 4.2. However, this $(\pi, 0, \pi)$ antiferromagnetism, although breaking the C_4 symmetry, produces only a small splitting between the bands at X and Y. In fact, the band energy at Y is even slightly higher than that at X. From our calculation using other values of U and J, this near degeneracy of the bands at X and Y is quite robust, which contradicts ARPES measurements [138]. As will be seen, this problem

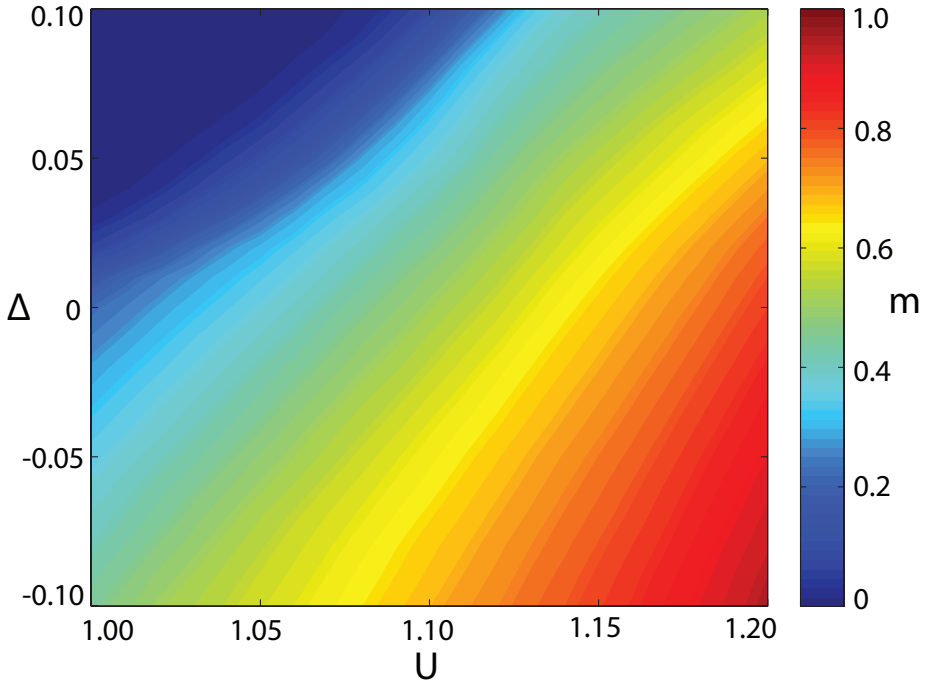

Figure 4.7: The total staggered magnetic moment as a function of the Coulomb repulsion U and orbital nematic order parameter Δ. We set Hund's exchange $J = 0.20U$.

can be alleviated by including orbital ordering. Hence, orbital order $\mathcal{H}_N$ (4.5) is still present in the antiferromagnetic phase and has important experimental consequences.

In order to simplify our discussions, we set $J = 0.20U$ and focus in the regime $U \in [1.0, 1.2]$ and $\Delta \in [-0.1, 0.1]$, where significant agreement with experiment can be found. We first investigate variations of the total staggered magnetic moment m for different U and Δ. As discussed in Sec. 4.3, a negative Δ induces better nesting between hole and electron pockets and stabilizes the $(\pi, 0, \pi)$ magnetic order, thus leading to an increase of m as shown in Fig. 4.7. In contrast, the magnetic moment m decreases when Δ takes larger positive values. In fact, a positive Δ places the d_{xz} orbital higher in energy compared to d_{yz}, and favors the antiferromagnetism with $\boldsymbol{q} = (0, \pi, \pi)$ instead. This interesting interplay between the orbital and magnetic order is also noted recently [197] based on LDA results and a Ginzburg-Landau phenomenological theory.

To further illustrate the role of orbital order in the reconstruction of the electronic structure in the magnetically ordered phase, we plot the Fermi surfaces and polarized dispersions in Fig. 4.8. We use the set of parameters, $U = 1.08$, $J = 0.20U$, and $\Delta = -0.08$, to be consistent with previous figures. From Fig. 4.8(c) and (d), the desired band splitting between X and Y is successfully produced due to a negative Δ. Furthermore, there are multiple band crossings at the Fermi energy along X-Γ-X whereas only a single crossing occurs along

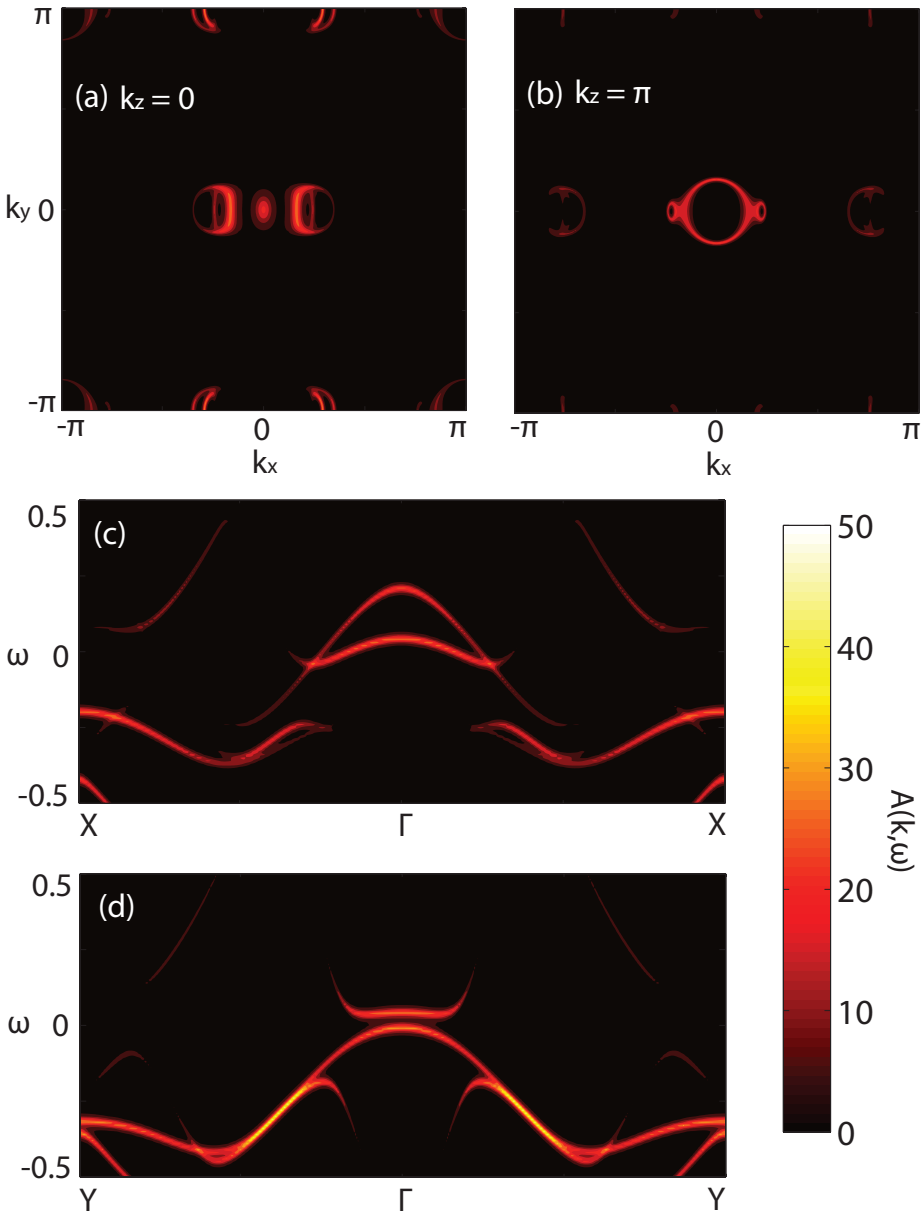

Figure 4.8: Fermi surfaces in the plane of (a) $k_z = 0$ and (b) $k_z = \pi$. Polarized dispersions along the line of (c) X-Γ-X and (d) Y-Γ-Y. The parameters used here are $U = 1.08$, $J = 0.20U$ and $\Delta = -0.08$, with the total mean-field staggered moment $m = 0.62$.

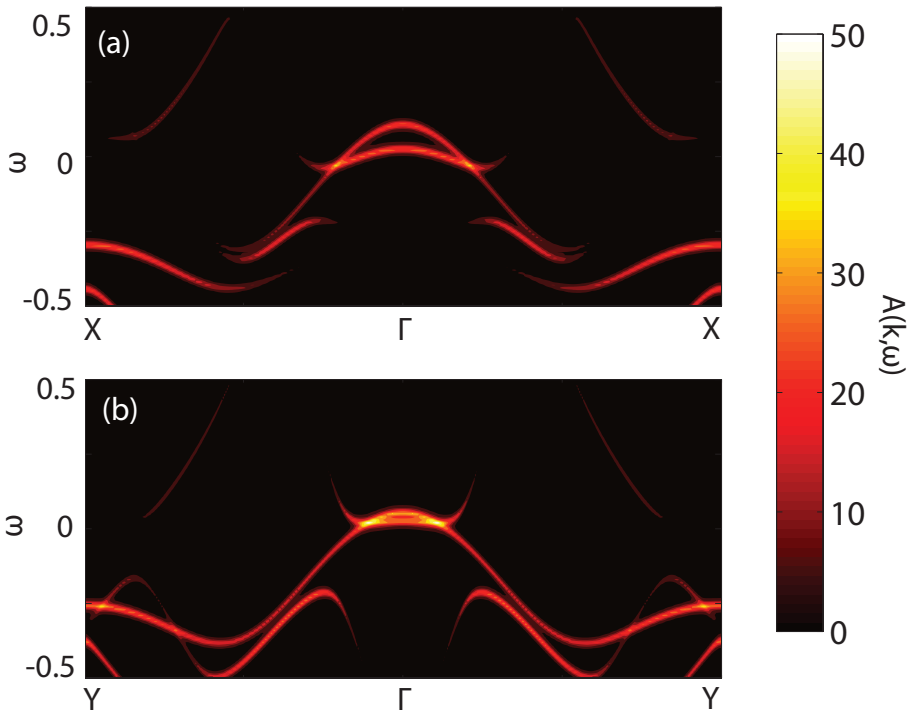

Figure 4.9: Polarized dispersions along (a) X-Γ-X and (b) Y-Γ-Y, for $U = 1.13$, $J = 0.20U$, and $\Delta = 0$. The corresponding magnetic moment $m = 0.61$, which is close to $m = 0.62$ of Fig. 4.8.

Y-Γ-Y, also in agreement with ARPES findings [138]. We further point out that the two small Fermi surfaces adjacent to the large hole pocket in Fig. 4.8(b) are actually Dirac cones, which have been predicted theoretically [42] and confirmed experimentally [138, 198], Note however, that the existence of Dirac cones relies on the degeneracy between the d_{xz} and d_{yz} orbitals [42]. But the small orbital order used here is not enough to annihilate such Dirac features. Finally the two Fermi surface segments close to the zone center in Fig. 4.8(a) are mostly aligned along the ferromagnetic y-direction and in principle can produce the quasi-one-dimensional interference pattern observed in STM [111].

However, attentive readers may notice that for Fig. 4.8, the corresponding magnetic moment $m = 0.62$, which is larger than $m = 0.46$ of Fig. 4.6. Hence it is possible that the splitting between the bands at X and Y is caused by the stronger magnetic order in Fig. 4.8. In order to confirm the splitting is entirely due to the orbital order term $\mathcal{H}_N$ (4.5), we plot the polarized dispersions in Fig. 4.9 for $U = 1.13$, $J = 0.20U$, and $\Delta = 0$. These parameters produce a staggered magnetic moment $m = 0.61$, which is close to the value of $m = 0.62$ in Fig. 4.8. However, no splitting between the bands at X and Y is generated in Fig. 4.9, where the band energy at X is even slightly lower than that at Y. As we have pointed out earlier, this near degeneracy between the band energy at X and Y survives for other values of U and J as well, as long as the orbital

nematic order parameter $\Delta = 0$. Therefore we have shown that it is the orbital order $\mathcal{H}_N$ (4.5), rather than the stripe antiferromagnetism, that is responsible for the band splitting at X and Y observed in ARPES [138].

We end this section by discussing the optical spectra in the presence of both orbital and magnetic order. The same set of parameters as those of Fig. 4.8 are used here. From Fig. 4.10(a), we see that the optical conductivity shows two peaks at frequency ω_1 and ω_2, which have similar values as we defined previously. Compared to the results without the magnetic order (see Fig. 4.4), the magnitude of the peak at ω_1 increased significantly. So the onset of this low-energy peak at ω_1 is mostly due to antiferromagnetism which opens up a gap at the chemical potential and shifts part of the Drude weight to the region around ω_1. On the other hand, the high-energy peak at ω_2 comes from the inter-band transitions that are already present in the original multi-orbital model. However, we cannot distinguish along which direction the optical conductivity dominates since there are multiple crossings (as a function of frequency) between the two curves of σ_{xx} and σ_{yy}. But naively, σ_{xx} does have higher values in most of the regions around ω_1, which matches the experimental results [130] at the low-temperature antiferromagnetic phase. Also of note is the region around ω_1 where σ_{xx} displays a single peak whereas σ_{yy} acquires a double-peak structure, which is also reproduced in recent LDA+DMFT study [199]. Anisotropy of the Drude weight is presented as a function of U and Δ in Fig. 4.10(b). If we assume an isotropic scattering rate, the dc conductivity anisotropy has the correct directionality in a very large region of parameter space. However, considering the $(\pi, 0, \pi)$ antiferromagnetism, we should expect a larger scattering rate along the x-direction where the spins are antiparallel to their neighbors. This should further restrict the parameter space of interest. Nonetheless, we find that in a reasonable range of parameters, both orbital and magnetic order underlie the resistivity anisotropy in a multi-orbital model of the pnictides.

4.5 Final remarks

In summary, we have solved a three-dimensional five-orbital model using the mean-field approximation in the presence of both orbital and magnetic order. We modeled the orbital order phenomenologically as an energy splitting term between the two otherwise degenerate d_{xz} and d_{yz} orbitals, and find that it is solely responsible for the splitting between the bands at X and Y observed by polarized ARPES [138]. This orbital nematic order also causes the Drude weight difference between the two diagonal directions for the paramagnetic phase, in agreement with the analysis based on optical conductivity [130]. On the other hand, the magnetic order sets in at a lower temperature. It opens up a gap at the Fermi energy and shifts part of the Drude weight to high energies, leading to the emergence of a peak structure at $\omega_1 \approx 0.2$ in the optical conductivity. However, magnetic order alone cannot explain the anisotropic dispersions, especially the

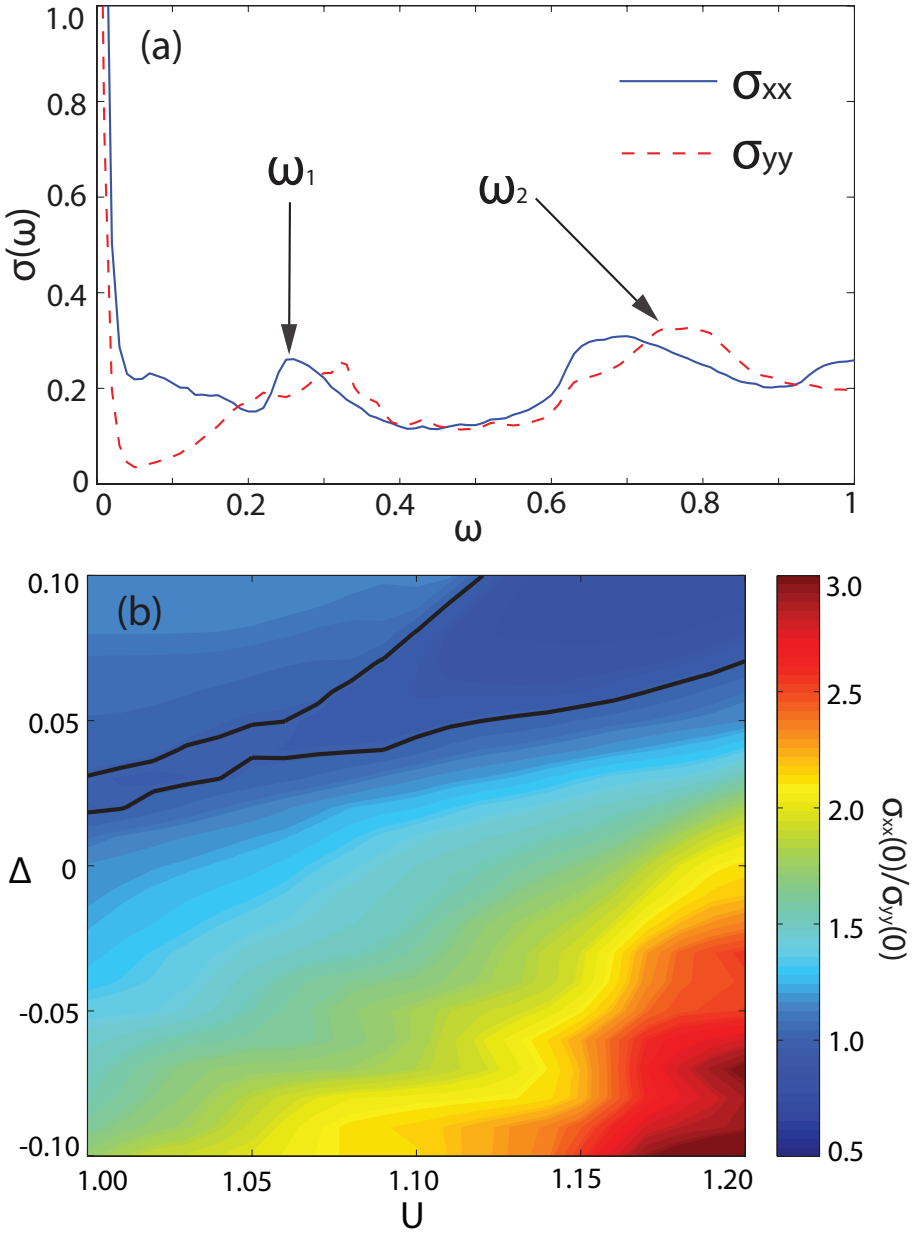

Figure 4.10: (a) Optical conductivity $\sigma_{xx}(\omega)$ and $\sigma_{yy}(\omega)$ calculated using $U = 1.08$, $J = 0.20U$, and $\Delta = -0.08$. They are plotted in the same unit as Fig. 4.4. (b) Anisotropy of Drude weight, $\sigma_{xx}(0)/\sigma_{yy}(0)$ as a function of U and Δ. The black line separates the regions where $\sigma_{xx}(0) > \sigma_{yy}(0)$ and where $\sigma_{xx}(0) < \sigma_{yy}(0)$. We choose $J = 0.20U$ here.

band splitting between X and Y. Thus both orbital and magnetic orders are present in the low-temperature antiferromagnetic phase, and together induce various anisotropies seen by different experimental techniques. This result is in contrast with earlier studies [121, 137, 163] which claimed that the magnetic order is the driving mechanism for the anisotropy. Thus, our study establishes the importance of orbital order, irrespective of whether long-range magnetic order is present or not.

Besides orbital order, the anisotropy observed above the magneto-structural transition can come from a different mechanism, for example, static short-range magnetic order. Its existence is indeed supported by recent INS experiments [100]. In principle, we can model this by a probability distribution of the ordering wave vector peaked at $\boldsymbol{q} = (\pi, 0, \pi)$ [200], and investigate its modification to the electronic structure. It is expected that the magnitude of the sub-peak at ω_1 in Fig. 4.4(b) will increase due to this short-range magnetic order, thus yielding better agreement with experiments [130]. Nevertheless, the orbital order should always be present until the band splitting vanishes.

Of course, it remains an outstanding issue whether the nematic order above the magneto-structural transition is orbitally or magnetically driven. Thermodynamic measurement cannot distinguish them as both transitions fall into the Ising universality class. Indeed, increasing sample quality does drive the magnetic transition closer to the structural transition [201]. In our point of view, these two degrees of freedom actually coexist and cooperate with one another. A non-zero orbital order can certainly induce a spin nematicity without long-range magnetic order, and vice versa. It will be interesting if future INS experiments can settle the onset temperature of the spin nematic order and compare it to that of the orbital order measured by ARPES [138]. However, to account for the large anisotropy of the magnetic exchanges [81, 100], orbital degrees of freedom have to be considered.

One ingredient we ignored in our theory is the role of the structural distortions, which in principle should enhance the orbital order [202]. We also neglected possible strong-correlation physics, which may cause an orbital-selective Mott transition [203]. To conclude, orbital order is an important part of the minimal model of iron-based superconductors. It induces strong exchange anisotropy between the local moments, and leads to an electron nematic order on the itinerant level, governing the physics over a very large energy scale. The study of the interplay between the orbital and magnetic orders should shed new insight into the mechanism of superconductivity in this multi-orbital system.

Chapter 5

Orbital order from the local-itinerant model[1]

The magnetic excitations of the iron pnictides are explained within a degenerate double-exchange model. The local moment spins are coupled by superexchanges J_1 and J_2 between nearest and next-nearest neighbors, respectively, and interact with the itinerant electrons of the degenerate d_{xz} and d_{yz} orbitals via a ferromagnetic Hund exchange. The latter stabilizes $(\pi, 0)$ stripe antiferromagnetism due to emergent ferro-orbital order and the resulting kinetic energy gain by hopping preferably along the ferromagnetic spin direction. Taking the quantum nature of the spins into account, we calculate the magnetic excitation spectra in the presence of both super- and double-exchange. A dramatic increase of the spin-wave energies at the competing Néel ordering wave vector is found, in agreement with recent neutron scattering data. The spectra are fitted by a spin-only model with a strong spatial anisotropy and additional longer ranged couplings along the ferromagnetic chains. Over a realistic parameter range, the effective couplings along the chains are negative corresponding to unfrustrated stripe antiferromagnetism.

5.1 Introduction

The discovery of superconductivity in the pnictides [1, 8, 9, 10, 13, 204]. with transition temperatures challenging those of single-layer, high-T_c cuprates, immediately raised the question of whether, despite all their differences, the two classes of materials share the same key mechanism for superconductivity [205, 206, 207]. Arguably the most striking similarity is that superconductivity emerges upon doping antiferromagnetically ordered parent compounds. In the pnictides, however, the magnetic ordering is unusual, characterized by an antiferromagnetic arrangement of ferromagnetic chains, corresponding to an in-plane ordering wave vector $\boldsymbol{Q} = (\pi, 0)$ [19, 21, 22, 23, 176, 208, 209, 210, 211, 212]. Whereas the pnictides are metallic, the parent cuprates are Mott insulators. The conductivities in the pnictides are typical of bad metals, suggesting that electronic correlations [38, 83, 84, 95, 145, 146, 213, 214, 215, 216] are crucial. By contrast, the local-density approximation seems to be adequate [31] to describe their band structure.

[1] This chapter is from Ref. [103]

As a result of this dichotomy, both itinerant magnetism [31, 39, 41, 46, 67, 72, 217, 218] and local moment [84, 145, 146, 158, 178, 219, 220, 221, 222] scenarios have been suggested to explain the unusual stripe antiferromagnetism. Although the former weak-coupling theories which attribute the magnetism to a spin-density wave instability of a nested Fermi surface, can explain the magnetic low-energy excitations around the correct ordering wave vector, they fail to describe the spectra at higher energies which have been measured in great detail by inelastic neutron scattering [81, 109]. In particular, the itinerant scenarios can not explain the observed maximum in the dispersion at (π, π) but rather suggest that the excitations rapidly dissolve into a particle-hole continuum [218] which has not been found experimentally up to energies of 200meV. So far, a consistent description of the excitations over the entire energy range has been obtained only by using suitably parametrized Heisenberg models.

Because of the positions of the arsenic ions above or below the iron plaquettes, such a spin-only model is expected to be strongly frustrated with comparable, antiferromagnetic superexchanges J_1 and J_2 between nearest and next-nearest neighbors. In this regime, the model indeed exhibits long-range stripe-antiferromagnetic order [87, 144, 148], and the strong frustration and proximity to a continuous magnetic phase transition might explain why the observed magnetic moments are relatively small [84, 220]. Interestingly, the neutron scattering experiments tell a radically different story. The spin-wave velocities indicate that the exchange coupling along the ferromagnetic spin direction is much smaller than the one perpendicular to the chains [19], $J_{1y} \ll J_{1x}$. More recently, it has been argued [81] that the observed maximum of the dispersion at (π, π) even requires a slightly ferromagnetic exchange $J_{1y} < 0$ corresponding to an unfrustrated spin model in contrast to early claims [84] of high frustration.

What might be the cause of such a strong spatial anisotropy? In fact, before the magnetic order sets in, a structural transition occurs at which the two in-plane lattice constants become inequivalent. The structural and magnetic transition are clearly separated in the so-called '1111 compounds' [19, 21, 209, 211], whereas they occur at the same temperature in the '122 family' [22, 23, 210, 212]. However, inspecting the numbers, it appears that the orthorhombic lattice distortion is too small, by two orders of magnitude, to explain the magnetic anisotropy [222].

To this end, some have proposed [158, 159, 172, 173] that orbital-ordering physics of a similar kind as in the manganite transition-metal oxides not only provides a mechanism for the lattice distortion but more importantly explains the strong in-plane anisotropies. In particular, it has been argued [158] that due to an orbital degeneracy, the localized limit is described by a complicated spin-orbital super-exchange (Kugel-Khomskii) model rather than by a Heisenberg Hamiltonian. Further, it was shown that the stripe antiferromagnetism is stabilized by ferro-orbital order which breaks the in-plane lattice symmetry and induces a strong anisotropy between the magnetic exchange couplings.

Since the C_4 lattice symmetry is broken by the orbital order and the accompanying orthorhombic distortion, the electronic structure must reflect this spatial anisotropy with reduced symmetry [223]. Such an anisotropic electronic state has been confirmed recently in scanning-tunneling-microscopy (STM) experiments [111] and in-plane resistivity measurement [119, 120]. Moreover, dramatic Fermi-surface reconstructions at the structural transition [135]. as well as enormous transport [224] and phonon[181] anomalies, have been interpreted as clear indirect evidence for orbital ordering. Hence, on this interpretation, it is the orbital ordering that underlies the electronic anisotropy not an inherent anisotropy due entirely to the electrons, indicative of a true nematic state.

Consequently, an open problem with the pnictides is the role itineracy and local physics play in mediating the apparently unfrustrated anisotropic magnetism. In this work, we start from the idea of the 'local-itinerant dichotomy' [95, 96, 97] of the iron pnictides and motivate an effective degenerate double-exchange (DDEX) model very similar to the ones used to describe metallic manganites with orbital degeneracies [225, 226, 227]. To be more precise, we assume a ferromagnetic Hund coupling between the local moments, which are described by the aforementioned J_1-J_2 Heisenberg model, and the itinerant bands of the doubly-degenerate d_{xz} and d_{yz} orbitals. In the context of the manganites it has been shown [225, 226, 227] that such DDEX models exhibit phases with long-range stripe-antiferromagnetic order. Despite the antiferromagnetic couplings between neighboring local moment spins, emergent ferro-orbital order goes hand in hand with the formation of ferromagnetic spin chains in order to minimize the kinetic energy of the itinerant electrons by directing it predominantly along the chains. Obviously, the resulting electronic state is highly anisotropic. Moreover, the double exchange is expected to strongly suppress the effective coupling between local moments along the chains, and possibly to make it even ferromagnetic [228].

In this work, we analyze the effective DDEX model for the iron pnictides layers. We indeed find the orbitally ordered $(\pi, 0)$ antiferromagnet to be stable over a wide parameter range including realistic values for the parent pnictide materials. In particular, the seizable next-nearest neighbor superexchange J_2 further stabilizes this phase. Whereas these results are to a large extend not surprising given the similarities with the manganites, the magnetic excitation spectra so far have been calculated only for a ladder system [229]. For the manganites, the DDEX model is usually simplified [225, 226, 227] by treating the core spins as classical and by taking the limit of large or infinite Hund's coupling J_{H} which is not justified for the pnictides. Here, we instead focus on the regime of small and intermediate J_{H} and develop the tools to calculate the magnetic excitation spectra in the presence of both, super- and double-exchange to linear-spin-wave order. The spectra are found to be in good agreement with the neutron scattering data [81]. In particular, in some parameter space the double exchange along the ferromagnetic chains can overcompensate the bare

antiferromagnetic superexchange as suggested by the experiment.

This chapter is organized as follows. In Sec. 5.2, we construct the local-itinerant, DDEX model. Sec. 5.3 deals with the methods we use to solve the model. Namely, a canonical transformation is performed to identify the true magnons of the system. In Sec. 5.4, we summarize our results, including ferro-orbital ordering, the magnetic excitation spectra, and the magnetic anisotropy. Finally Sec. 5.5 discusses several aspects of our theory and validates its applicability to the pnictides.

5.2 Model

In this Section, we proceed to motivate the DDEX model for the pnictides. This model accounts for the presence of local moments, as suggested by the neutron scattering experiments, as well as itinerant electrons responsible for the bad-metal behavior of the parent compounds. Moreover, the orbital degeneracy in combination with the Hund coupling between electronic and spin degrees of freedom gives rise to orbital-ordering physics beyond simple band-structure theory. The Hamiltonian consists of three parts,

$$\mathcal{H} = \mathcal{H}_{\rm loc} + \mathcal{H}_{\rm it} + \mathcal{H}_{\rm H}, \tag{5.1}$$

where $\mathcal{H}_{\rm loc}$ describes the superexchange couplings between local moments, $\mathcal{H}_{\rm it}$ the itinerant electrons of the degenerate d_{xz} and d_{yz} orbitals, and $\mathcal{H}_{\rm H}$ the ferromagnetic Hund coupling between the local moments and the itinerant electrons. We point out that in order for this model to be valid, the Hund coupling $J_{\rm H}$ should be small compared to the tetrahedral crystal field splitting between the t_{2g} and e_g multiplets, but larger than the tetragonal splitting between the d_{xy} orbital and the degenerate d_{xz},d_{yz} doublet [158].

The local moments with spin S are coupled by super-exchanges J_1 and J_2 between nearest and next-nearest neighbors, respectively. The corresponding Heisenberg Hamiltonian reads

$$\mathcal{H}_{\rm loc} = \frac{J_1}{S^2} \sum_{\langle i,j \rangle} \boldsymbol{S}_i \cdot \boldsymbol{S}_j + \frac{J_2}{S^2} \sum_{\langle\langle i,j \rangle\rangle} \boldsymbol{S}_i \cdot \boldsymbol{S}_j, \tag{5.2}$$

where, for convenience, the super-exchanges are measured in units of S^2. Likewise, the Hund exchange $J_{\rm H}$ which couples the electron spins to the local moments will be measured in units of S. This convention will facilitate our large-S expansion later. The superexchanges are mediated by virtual hopping processes via the p-orbitals of the arsenic ions which have alternating positions above or below the iron plaquettes. Certainly, a quantitative comparison of the exchange couplings would require knowledge of the two different Fe-As-Fe bond angles and the precise shape of the orbitals. Assuming that the virtual processes for the nearest-neighbor and diagonal bonds involve roughly the same energies, we

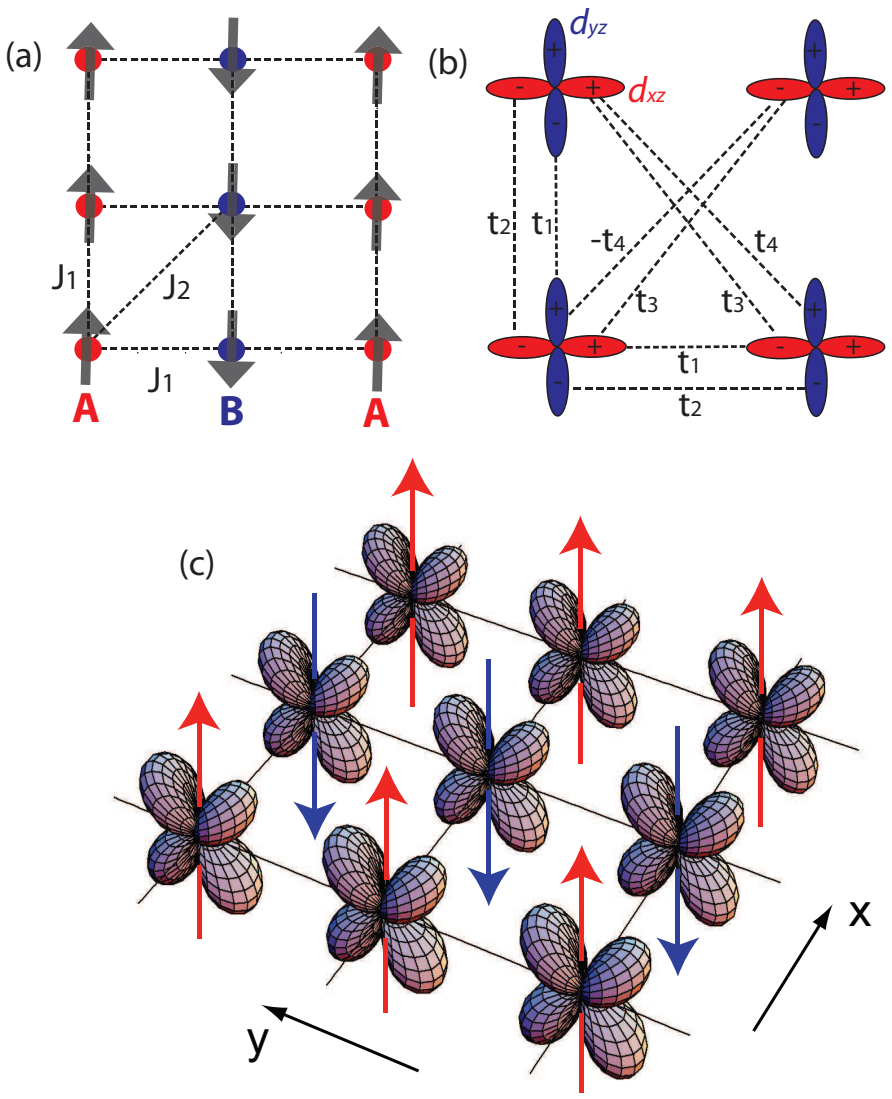

Figure 5.1: Illustration of the degenerate double-exchange model for the pnictides. (a) The local moments are coupled by nearest- and next-nearest-neighbor exchanges J_1 and J_2, respectively, and interact via a ferromagnetic Hund coupling $J_{\rm H}$ with the itinerant electrons of the degenerate d_{xz}, d_{yz} orbitals. (b) Illustration of the hopping parameters in a two-band model of these orbitals (shown as projections in the plane). (c) Resulting ferro-orbital order which stabilizes the $(\pi, 0)$ antiferromagnetism by directing the kinetic energy of the electrons along the ferromagnetic spin direction.

estimate $J_1 \approx 2J_2$ since two exchange paths via different arsenic ions contribute to J_1. Therefore, we expect the Heisenberg model (5.2) to be strongly frustrated and potentially in the quantum disordered regime.

The itinerant electrons of the degenerate d_{xz} and d_{yz} orbitals are described by a tight-binding Hamiltonian

$$\mathcal{H}_{\mathrm{it}} = -\sum_{ij,\alpha\beta,\nu} t_{ij}^{\alpha\beta} c_{i\alpha\nu}^{\dagger} c_{j\beta\nu}, \tag{5.3}$$

where $c_{i\alpha\nu}^{\dagger}$ creates an electron at site i on orbital α with spin ν. The hopping integrals $t_{ij}^{\alpha\beta}$ are illustrated in Fig. 5.1(b) and defined in the same way as Ref. [41]. For simplicity, we neglect inter- and intra-orbital Coulomb interactions [52] between the itinerant electrons. This is justified since on the level of the effective DDEX model, the local moments are formed as a consequence of strong correlations whereas the residual charge carriers should be viewed as weakly interacting quasiparticles. We will assume t_1 to be dominant hopping amplitude because a larger wave-function overlap is expected when the orbitals point towards one another. However, the precise shape of the orbitals is not determined by geometry but depends on quantum chemistry, for example, on the amount of hybridization between the Fe d- and As p-orbitals [95]. Here we simply denote the orbitals by d_{xz} and d_{yz} because of the spatial symmetry shared with the atomic Fe orbitals. Recently, it has been suggested [172] that the hybridization leads to a strong deformation of the orbitals which make the π overlap, t_2 the dominant one. We point out that our results persist for the exchange of t_1 and t_2, the only difference being that the orbital polarization will be inverted in order to maximize the overlap along the ferromagnetic spin direction.

We do not attempt to fit our hopping parameters to reproduce the electron and hole pockets as being done in the previous two-orbital models [41, 43] on the level of a tight-binding approximation. Such parameters are inherently arbitrary since the hopping amplitudes are not uniquely determined by a particular constant energy cut [43] and because Coulomb interactions and Hund's exchange are of the order of the electronic bandwidth [38, 83, 213, 214, 215, 216].

Finally the local moments and the itinerant electrons interact by a ferromagnetic Hund coupling,

$$\mathcal{H}_{\mathrm{H}} = -\frac{J_{\mathrm{H}}}{2S} \sum_{i,\alpha,\nu\nu'} \boldsymbol{S}_i \cdot c_{i\alpha\nu}^{\dagger} \boldsymbol{\sigma}_{\nu\nu'} c_{i\alpha\nu'}, \tag{5.4}$$

where $\boldsymbol{\sigma}_{\nu\nu'} = (\sigma^x, \sigma^y, \sigma^z)_{\nu\nu'}$ with σ^{α} are the standard Pauli matrices and $J_{\mathrm{H}} > 0$. As mentioned before, the Hund exchange is measured in units of the local moment S. We note that similar models have been proposed in the context of the pnictides [96, 97]. However, the orbital degeneracy which is the pre-requisite for orbital-ordering physics and the resulting spatial anisotropies has not been

included.

5.3 Method

In this Section, we outline the approximations and transformation we employ to analyze the complicated DDEX model for the pnictides. In similar models for the maganites, the problem is typically simplified by treating the local moments as classical spins and assuming an infinitely strong Hund exchange [225, 226, 227]. In the pnictides, these approximations are not justified since the Hund coupling is of the order of the electronic bandwidth and since the local moments are small and presumably best described by the extreme quantum limit, $S = 1/2$. Moreover, our goal is the calculation of the magnetic excitation spectra in the presence of super- and double-exchange which will require the inclusion of quantum fluctuations of the spins. Although the spins are small and the Heisenberg model $\mathcal{H}_{\rm loc}$ is strongly frustrated, it is reasonable to treat the local moments on the level of linear spin-wave theory since the double exchange leads to a dramatic stabilization of the magnetic order. Moreover, it has been argued that the $1/S$ expansion is much better behaved for $(\pi, 0)$ order as compared to conventional (π, π) Néel antiferromagnetism [220].

Since the Hund coupling $\mathcal{H}_{\rm H}$ does not conserve the magnons describing the spin-wave excitation of the isolated local moments, we perform a canonical transformation in order to identify the true magnons of the coupled system. Readers not interested in the details of this calculation can skip immediately to the results, Sec. 5.4.

5.3.1 Operator rotations

Following the standard treatment of the antiferromagnetic Heisenberg model, we perform the spin rotation $S_i^x = \tilde{S}_i^x$, $S_i^y = \kappa_i \tilde{S}_i^y$, and $S_i^z = \kappa_i \tilde{S}_i^z$ where $\kappa_i = \exp(i\boldsymbol{Q}\cdot\boldsymbol{r}_i) = \pm 1$ for sublattice A and B respectively [see Fig. 5.1(a)]. Representing the rotated spin operators $\tilde{\boldsymbol{S}}_i$ by Holstein-Primakoff (HP) bosons a_i, $a_i^\dagger$, to the leading order, $\tilde{S}_i^z = S - a_i^\dagger a_i$, $\tilde{S}_i^+ = \sqrt{2S}a_i$, and $\tilde{S}_i^- = a_i^\dagger\sqrt{2S}$ ($\tilde{S}_i^\pm = \tilde{S}_i^x \pm i\tilde{S}_i^y$), we immediately derive the following expression for $\mathcal{H}_{\rm loc}$ in the linear spin-wave approximation,

$$\begin{aligned}\mathcal{H}_{\rm loc}^{\rm sw} &= \sum_q \Big[A_0(q)\left(a_q^\dagger a_q + a_{-q}a_{-q}^\dagger\right) \\ &\quad + B_0(q)\left(a_q^\dagger a_{-q}^\dagger + a_{-q}a_q\right)\Big], \end{aligned} \tag{5.5}$$

where $A_0(q) = (J_1\cos q_y + 2J_2)/S$ and $B_0(q) = (J_1\cos q_x + 2J_2\cos q_x\cos q_y)/S$.

In order to leave the Hund coupling term $\mathcal{H}_{\rm H}$ invariant, we perform exactly the same rotation of the electron spins $\boldsymbol{s}_{i\alpha} = \frac{1}{2}\sum_{\nu\nu'} c_{i\alpha\nu}^\dagger \boldsymbol{\sigma}_{\nu\nu'} c_{i\alpha\nu'}$. This is achieved by transforming the fermion operators as $c_{i\alpha\nu} = \tilde{c}_{i\alpha\nu}$ for sites i on

sublattice A and $c_{i\alpha\nu} = \tilde{c}_{i\alpha\bar{\nu}}$ on sublattice B. In the latter expression, we have defined $\bar{\nu} = \downarrow$ for $\nu = \uparrow$ and vice versa. In terms of the HP boson creation and annihilation operators a_i, $a_i^\dagger$ and rotated fermion operators $\tilde{c}_{i\alpha\nu}$, $\tilde{c}_{i\alpha\nu}^\dagger$ the Hund exchange can be written as

$$\begin{aligned}
\mathcal{H}_{\rm H} &= \mathcal{H}_{\rm H}^{(0)} + \mathcal{H}_{\rm H}^{(1)} + \mathcal{H}_{\rm H}^{(2)}, && (5.6)\\
\mathcal{H}_{\rm H}^{(0)} &= -\frac{J_{\rm H}}{2} \sum_{k,\alpha,\nu} \nu \tilde{c}_{k\alpha\nu}^\dagger \tilde{c}_{k\alpha\nu}, && (5.7)\\
\mathcal{H}_{\rm H}^{(1)} &= -\frac{J_{\rm H}}{\sqrt{2S}} \sum_{kq,\alpha} \left(a_q \tilde{c}_{k+q,\alpha\downarrow}^\dagger \tilde{c}_{k\alpha\uparrow} + {\rm h.c.} \right), && (5.8)\\
\mathcal{H}_{\rm H}^{(2)} &= \frac{J_{\rm H}}{2S} \sum_{k,qq',\alpha\nu} \nu a_q^\dagger a_{q'} \tilde{c}_{k-q,\alpha\nu}^\dagger \tilde{c}_{k-q',\alpha\nu}, && (5.9)
\end{aligned}$$

where $\nu = \pm 1$ for up and down spins respectively. Note that $\mathcal{H}_{\rm H}^{(0)}$ only involves the electronic operators and represents the zeroth-order corrections to the electron energies by the classical background stripe antiferromagnetism. $\mathcal{H}_{\rm H}^{(1)}$ and $\mathcal{H}_{\rm H}^{(2)}$ are the couplings between the electrons and the HP bosons, linear and quadratic in the boson operators. In the following, we include the term $\mathcal{H}_{\rm H}^{(0)}$ in the itinerant electron Hamiltonian, yielding the effective free-electron Hamiltonian

$$\begin{aligned}
\mathcal{H}_{\rm e} &= \mathcal{H}_{\rm it} + \mathcal{H}_{\rm H}^{(0)} \\
&= \sum_{k,\alpha,\nu} \Bigg[\left(\varepsilon_1^\alpha(k) - \nu \frac{J_{\rm H}}{2} \right) \tilde{c}_{k\alpha\nu}^\dagger \tilde{c}_{k\alpha\nu} \\
&\qquad + \varepsilon_2^\alpha(k)\, \tilde{c}_{k\alpha\nu}^\dagger \tilde{c}_{k\alpha\bar{\nu}} + \varepsilon_3(k)\, \tilde{c}_{k\alpha\nu}^\dagger \tilde{c}_{k\bar{\alpha}\bar{\nu}} \Bigg], && (5.10)
\end{aligned}$$

where $\bar{\alpha} = yz$ for $\alpha = xz$ and vice versa. We have defined $\varepsilon_1^{xz}(k) = -2t_2 \cos k_y$, $\varepsilon_1^{yz}(k) = -2t_1 \cos k_y$, $\varepsilon_2^{xz}(k) = -2t_1 \cos k_x - 4t_3 \cos k_x \cos k_y$, $\varepsilon_2^{yz}(k) = -2t_2 \cos k_x - 4t_3 \cos k_x \cos k_y$, and $\varepsilon_3(k) = -4t_4 \sin k_x \sin k_y$.

5.3.2 Canonical transformation

Apparently, the interaction term $\mathcal{H}_{\rm H}^{(1)}$ is linear in the HP boson a_i, which shows that these bosons do not represent the Goldstone modes of the system, namely the transverse fluctuations of the total staggered magnetic moments, which consist of not only the local moments, but also the spins of the itinerant electrons. In order to correctly identify the true magnons and carry out the subsequent spin-wave calculations, we need to perform a canonical transformation of the original Hamiltonian $\mathcal{H} = \mathcal{H}_{\rm loc}^{\rm sw} + \mathcal{H}_{\rm e} + \mathcal{H}_{\rm H}^{(1)} + \mathcal{H}_{\rm H}^{(2)}$,

$$\begin{aligned}
\mathcal{H}' &= e^{\Delta} \mathcal{H} e^{-\Delta} \\
&= \mathcal{H} + [\Delta, \mathcal{H}] + \frac{1}{2} [\Delta, [\Delta, \mathcal{H}]] + \ldots && (5.11)
\end{aligned}$$

with Δ a suitable anti-Hermitian operator, $\Delta^\dagger = -\Delta$, such that in the transformed $\mathcal{H}'$, the terms linear in a_i's are eliminated. Similar canonical transformations [230, 231] and equivalent perturbative methods [232] have been used in order to explain ferromagnetism in double-exchange models with a single itinerant band. Up to the leading order, the transformation is determined by

$$[\Delta, \mathcal{H}_{\rm e}] + \mathcal{H}_{\rm H}^{(1)} = 0. \tag{5.12}$$

To find the Δ satisfying (5.12), we first diagonalize $\mathcal{H}_{\rm e}$ by a unitary transformation $\tilde{c}_{k\alpha\nu} = \sum_n U^n_{\alpha\nu}(k) d_{nk}$, yielding $\mathcal{H}_{\rm e} = \sum_{n,k} E_n(k) d^\dagger_{nk} d_{nk}$. Here, n labels the four electronic bands arising after diagonalization from the two orbital and two spin degrees of freedom. In the new basis of d_{nk}, it is easy to verify that (5.12) is solved by

$$\begin{aligned} \Delta &= \frac{J_{\rm H}}{\sqrt{2S}} \sum_{kq,mn,\alpha} \left(\frac{a_q d^\dagger_{m,k+q} d_{nk}}{E_n(k) - E_m(k+q)} \right. \\ &\qquad \left. \times\ U^{m*}_{\alpha\downarrow}(k+q) U^n_{\alpha\uparrow}(k) - \text{h.c.} \right). \end{aligned} \tag{5.13}$$

After the canonical transformation (5.11), the Hamiltonian up to order $1/S$ reads $\mathcal{H}' = \mathcal{H}_{\rm e} + \mathcal{H}^{\rm sw}_{\rm loc} + \mathcal{H}^{(2)}_{\rm H} + \mathcal{H}'_2$, where $\mathcal{H}'_2 = [\Delta, \mathcal{H}^{(1)}_{\rm H}] + \frac{1}{2}[\Delta[\Delta, \mathcal{H}_{\rm e}]] = \frac{1}{2}[\Delta, \mathcal{H}^{(1)}_{\rm H}]$. The commutators $[\Delta, \mathcal{H}^{\rm sw}_{\rm loc}]$ and $[\Delta, \mathcal{H}^{(2)}_{\rm K}]$ are of higher orders in $1/S$ and the boson operators, and thus can be dropped in the linear spin-wave approximation. The contributions $\mathcal{H}^{(2)}_{\rm H}$ and $\mathcal{H}'_2$ are bilinear in both the bosonic and fermionic operators. After taking the expectation values of the electronic operators with respect to the diagonal electronic Hamiltonian $\mathcal{H}_{\rm e}$, we obtain the final spin-wave Hamiltonian

$$\begin{aligned} \mathcal{H}^{\rm sw} &= \mathcal{H}^{\rm sw}_{\rm loc} + \left\langle \mathcal{H}^{(2)}_{\rm H} + \frac{1}{2}[\Delta, \mathcal{H}^{(1)}_{\rm H}] \right\rangle_{\rm e} \\ &= \sum_q \Big[A(q) \left(a^\dagger_q a_q + a_{-q} a^\dagger_{-q} \right) \\ &\qquad + B(q) \left(a^\dagger_q a^\dagger_{-q} + a_{-q} a_q \right) \Big] \end{aligned} \tag{5.14}$$

with $A(q) = A_0(q) + A_1 + A_2(q)$ and $B(q) = B_0(q) + B_2(q)$. The constant 'self-energy' correction, A_1, arises from $H^{(2)}_{\rm K}$ whereas $H'_2 = \frac{1}{2}[\Delta, \mathcal{H}^{(1)}_{\rm H}]$ generates momentum-dependent corrections to both the 'self-energy' and the 'anomalous amplitude', which are denoted as $A_2(q)$ and $B_2(q)$. These corrections are ex-

pressed as

$$A_1 = \frac{J_{\rm H}}{2S}\sum_{k,n} f_n(k)\sum_{\alpha,\nu}\nu\left|U^n_{\alpha\nu}(k)\right|^2, \tag{5.15}$$

$$A_2(q) = \frac{J_{\rm H}^2}{2S}\sum_{k,mn}\frac{f_n(k)-f_m(k+q)}{E_n(k)-E_m(k+q)} \times\left|\sum_{\alpha} U^{m*}_{\alpha\downarrow}(k+q)U^n_{\alpha\uparrow}(k)\right|^2, \tag{5.16}$$

$$B_2(q) = \frac{J_{\rm H}^2}{2S}\sum_{k,mn}\frac{f_n(k)-f_m(k+q)}{E_n(k)-E_m(k+q)} \times\sum_{\alpha\beta} U^{m*}_{\alpha\downarrow}(k+q)U^n_{\alpha\uparrow}(k)U^{n*}_{\beta\downarrow}(k)U^m_{\beta\uparrow}(k+q), \tag{5.17}$$

where $f_n(k) = 1/(1+e^{\beta(E_n(k)-\mu)})$ is the Fermi distribution function with μ the chemical potential. The Hamiltonian (5.14) is diagonalized by a Bogoliubov transformation yielding the spin-wave dispersion

$$\omega(q) = \sqrt{A^2(q)-B^2(q)} \tag{5.18}$$

of the system in the presence of both super- and double-exchange.

5.4 Results

5.4.1 Classical phase diagram

As a pre-requisite for the spin-wave expansion, we have to clarify the classical phase diagram at first. In the absence of the itinerant electrons, the line $J_2 = J_1/2$ separates two classical antiferromagnetic ground states of the local moments characterized by ordering wave vectors of $(\pi, 0)$ and (π, π), respectively. For $J_2 > J_1/2$ where the stripe order is favored, the itinerant electrons will be more likely to occupy the d_{yz} orbital that has a larger hopping amplitude along the ferromagnetic y-direction. According to the double-exchange mechanism, this ferro-orbital-ordered state will induce an effective ferromagnetic exchange that is stronger along the y-direction than along the x-direction. Thus the spin frustration should be reduced and the stripe order should be further stabilized. However, when $J_2 < J_1/2$, the local moments will form a (π, π) Néel order, in which the hoppings of the itinerant electrons will be impeded due to the Hund exchange. So it is possible that for a sufficient large $J_{\rm H}$ the stripe order can still develop if the the kinetic energy gains by hoppings along ferromagnetic spin direction win out against the difference of magnetic energies of the two spin states.

Now we set out to compute the phase diagram by comparing the classical ground state energy of the two spin configurations. The tight-binding hopping

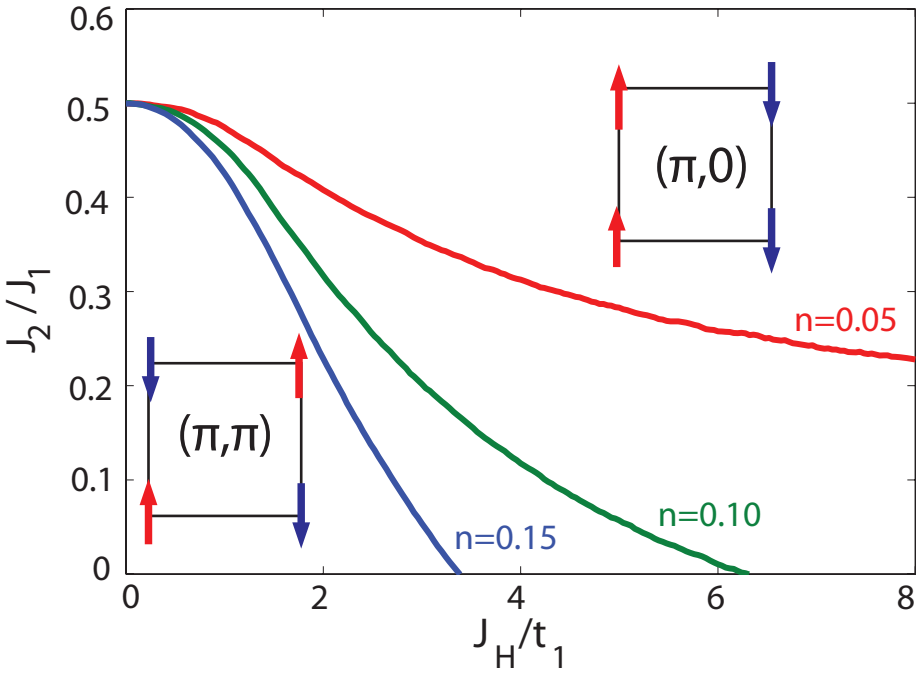

Figure 5.2: The classical phase diagram of the degenerate double-exchange model for $J_1 = 0.04t_1$, at filling levels $n = 0.05$, $n = 0.10$, and $n = 0.15$. The tight-binding hopping parameters being used to produce the figure are $t_2 = -0.1t_1$, $t_3 = 0.2t_1$, and $t_4 = 0.05t_1$.

parameters are chosen as $t_2 = -0.1t_1$, $t_3 = 0.2t_1$, and $t_4 = 0.05t_1$, so that t_1 is much larger than the other hopping amplitudes to enhance the transport along the ferromagnetic spin chains. In addition, the relatively small t_4 helps to reduce the overlap of the two orbitals and thus promotes the desired ferro-orbital ordering. Here and thereafter, all the energies will be expressed in the unit of t_1, the largest of the hopping amplitudes. We further set $J_1 = 0.04t_\sigma$ so that the exchange constants are of the order of 10 meV for a bandwidth of 1 eV, in agreement with both numerical [178] and experimental [81] observations. The resulting phase diagram is displayed in Fig. 5.2 for the filling of the itinerant electrons $n = 0.05$, $n = 0.1$, and $n = 0.15$, respectively. As being predicted, a large $J_{\rm H}$ can stabilize the stripe $(\pi, 0)$ order even when $J_2 < J_1/2$ favors a (π, π) Néel order. Moreover, as the filling level n increases, the stripe order is also preferred because the electrons can gain more kinetic energy in that configuration. Similar results have already been obtained in the context of the manganites [225, 226, 227].

However, in our following calculations we will mostly focus on the regime $J_2 > J_1/2$, where both the kinetic energy of the itinerant electrons and the exchange energy of the local moments prefer the $(\pi, 0)$ order. Therefore we can safely set up the spin-wave expansions for any $J_{\rm H}$ as long as the ferro-orbital order maintains. In principle, when $J_2 < J_1/2$, the linear spin-wave calculations

can still be carried out for a $J_{\rm H}$ that is large enough to drive the system to the stripe order classically. However, due to the strong competition between the electron kinetic energy and the magnetic exchange energy, the system may be disordered quantum mechanically, where the spin-wave expansion is unreliable. An interesting comparison can be drawn between the pnictides and the manganites. In manganites, the core spin has a length of $S = 3/2$ and is presumably described by a classical $O(3)$ vector. Furthermore, because of the nearly infinite strong Hund coupling and the relatively weak bare exchange between the local moments, the electron kinetic energy dictates the ground state by the classical double-exchange mechanism. In contrast, for the pnictides, the local moments are intrinsically quantum mechanical due to its small size, and the Hund coupling is only of the order of the electron bandwidth. More importantly, the local moments are strongly coupled by relatively large J_1 and J_2 exchange constants. Therefore, in pnictides, the $(\pi, 0)$ striped order is established mainly by the J_1-J_2 Heisenberg model, whereas the itinerant electrons give corrections to the spin-wave dispersions quantum mechanically and further stabilize the stripe order due to the kinetic energy gains from hopping along the ferromagnetic chains.

5.4.2 Orbital and spin polarization

We start with the inspection of the electronic Hamiltonian $\mathcal{H}_{\rm e}$ (5.10) which includes the Hund coupling to the local moments on a classical level given by $\mathcal{H}_{\rm H}^{(0)}$. From the diagonalization of $\mathcal{H}_{\rm e}$ (5.10) with the same set of hopping parameters as previously, we obtain the dispersions of the electronic bands $E_n(k)$ shown in Fig. 5.3(a) and (b) for a Hund exchange $J_{\rm H} = 1.0t_1$ and $J_{\rm H} = 0.1t_1$, respectively. The colors of each band are determined by the weight of the d_{yz} orbital, W_{yz}. We have 'blue' corresponding to $W_{yz} = 1$, a complete d_{yz} orbital, whereas a complete d_{xz} orbital ($W_{yz} = 0$) is displayed in 'red'. With t_4 being non-zero, these electronic bands are always superpositions of the two orbitals. However, if $J_{\rm H}$ is strong enough, each band is dominated by a single orbital throughout the Brillouin zone [Fig. 5.3(a)]. On the other hand, orbital mixing is much more prominent for a small $J_{\rm H}$ [Fig. 5.3(b)]. As will be shown, most of our calculations are done for a strong Hund exchange $J_{\rm H} \gtrsim 1.0t_1$. Therefore, from now on, we will denote these bands as 'd_{xz}' and 'd_{yz}' for simplicity.

Assuming translational invariance, the electron densities $\rho_{\alpha\nu}$ can be easily calculated as $\rho_{\alpha\nu} = \left\langle \tilde{c}^{\dagger}_{i\alpha\nu}\tilde{c}_{i\alpha\nu} \right\rangle$ with $\alpha = xz, yz$ the orbital and $\nu = \uparrow, \downarrow$ the spin index. Obviously, these densities sum up to the total filling of the bands, $n = \sum_{\alpha\nu} \rho_{\alpha\nu}$. In Fig. 5.3(c) and (d), the orbital and spin polarization, $n_o = \sum_{\nu}(\rho_{yz,\nu} - \rho_{xz,\nu})$ and $n_s = \sum_{\alpha}(\rho_{\alpha,\uparrow} - \rho_{\alpha,\downarrow})$ are plotted as functions of the total filling n for different values of the Hund coupling J_H/t_σ, using the same hopping amplitudes.

Without the presence of the itinerant electrons, the local moments form a

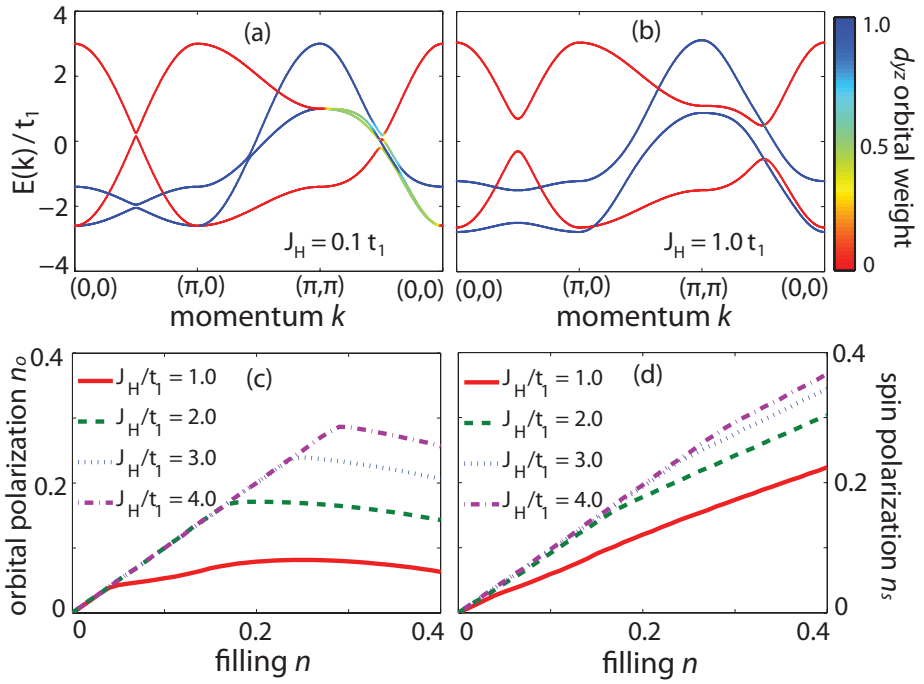

Figure 5.3: (a, b) The dispersions of the itinerant electron bands for $J_{\rm H} = 1.0t_1$(a) and $J_{\rm H} = 0.1t_1$(b), along the path $(0,0)$-$(\pi,0)$-(π,π)-$(0,0)$ in the Brillouin zone containing one Fe atom per unit cell. The bands are colored according to the weight of the d_{yz} orbital, from 'blue' for a complete d_{yz} orbital, to 'red' for a complete d_{xz} orbital. (c, d) orbital polarization n_o(c) and spin polarization n_s(d) as a function of the filling n of the itinerant bands, for various Hund's couplings $J_{\rm H}$. The hopping amplitudes are chosen the same as previously.

$(\pi,0)$ stripe antiferromagnetic ground state when $J_2 > J_1/2$. The spins are parallel along the y-direction and anti-parallel along the x-direction, as illustrated by Fig. 5.1(a). Due to the on-site ferromagnetic Hund coupling, the spins of itinerant electrons are more likely to be aligned in the same direction as are the local moments on every site. Hoppings along the x and diagonal directions put the electrons in the opposite spin states to the local moments either before or after the hopping process, and thus cost more energy in comparison to that involving hopping along the y-direction. With the assumption that t_1 is dominant, the electrons will first occupy the d_{yz} orbitals because of the kinetic energies gained by hopping along the ferromagnetic y-direction. Therefore, the system will form a ferro-orbital-ordered state with all the electrons occupying the d_{yz} orbitals [see Fig. 5.1(c)] until the Fermi energy reaches the bottom of the band of the d_{xz} orbitals. This behavior is shown in Fig. 5.3(c) for different Hund's coupling $J_{\rm H}$. In general, a larger $J_{\rm H}$ increases the energy difference between the two bands, and thus push the complete orbital polarization to a higher filling level. We denote the maximum filling level to which the ferro-orbital order is sustained by $\bar{n}$. When $n > \bar{n}$, electrons start to populate the d_{xz} orbitals, resulting in a decrease of the orbital polarization n_o. We have to note that 'd_{xz}' and

'd_{yz}' denote the diagonal electronic bands here, instead of the original orbitals defined in Fig. 5.1(b), as being mentioned before. The usage of these notations will be self-evident in our following discussions.

Furthermore, as the Hund coupling J_{H} tends to align the spins of the itinerant electrons with the local moments, the electrons are favored in a spin-up state on sublattice A, whereas a spin-down state obtains on sublattice B, corresponding to a spin-up polarized state on both sublattices in the space of the rotated electron operators $\tilde{c}_{i\alpha\nu}$. However, since the other hopping amplitudes, t_2, t_3 and t_4 are non-zero, the expectation values of the spin off-diagonal elements in $\mathcal{H}_{\mathrm{e}}$ (5.10) are always finite, leading to incomplete spin polarizations, as shown in Fig. 5.3(d). Generally speaking, a larger J_{H} produces a stronger spin polarization by increasing the energy difference between the spin-up and spin-down state. In actuality, assuming t_1 to be dominant, we expect that the spin polarization of the d_{yz} orbitals is larger than that of the d_{xz} orbitals. This is indeed reflected by the change in the slope of the spin polarization curves coinciding with the kink in the orbital polarization.

5.4.3 Spin-wave spectrum

Now we set out to calculate the spin-wave spectrum by considering the corrections from the itinerant bands to the original, strongly frustrated J_1-J_2 Heisenberg model. The hopping amplitudes are chosen the same as before. The spin length S of the local moment is $1/2$, which reflects the relatively small moment measured by the experiment [21] and is consistent with a local multiplet structure with an orbital degeneracy [158]. Finally the original Heisenberg model is strongly frustrated with $J_1 = 0.04t_1$ and $J_2 = 0.6J_1$.

We first calculate the spin-wave spectra for different filling levels n with $J_{\mathrm{H}} = 2.0t_1$, shown by Fig. 5.4(a). In this case, the complete orbital polarization is found up to $\bar{n} = 0.16$ [see Fig. 5.3(c)]. When $n = 0$, corresponding to an empty itinerant band, our model reduces to an isotropic J_1-J_2 Heisenberg model, where the linear spin-wave energies are zero at both $(\pi, 0)$ and (π, π). At finite electron densities $n < \bar{n}$, we observe that the spin-wave energy at (π, π) is pushed to higher values as n increases. This indicates a stabilization of the stripe antiferromagnetism over the competing Néel order. We also note a significant mode softening along the $(0, 0)$-$(\pi, 0)$ direction at low fillings due to the other finite hopping amplitudes t_2, t_3, and t_4. When $n > \bar{n}$, the anisotropy weakens with increasing filling n. This becomes manifest in a decreasing spin-wave energy at (π, π). As the filling level continues to rise, the spin-wave spectrum becomes unstable, not shown in the graph, suggesting that the system may evolve to a different ground state, possibly to a spin-disordered, superconducting state.

Fig. 5.4(b) shows the spin-wave spectra for different values of the Hund coupling J_{H}, which represents the interaction strength between the local moments and the itinerant electrons. The parameters used are the same as above, and

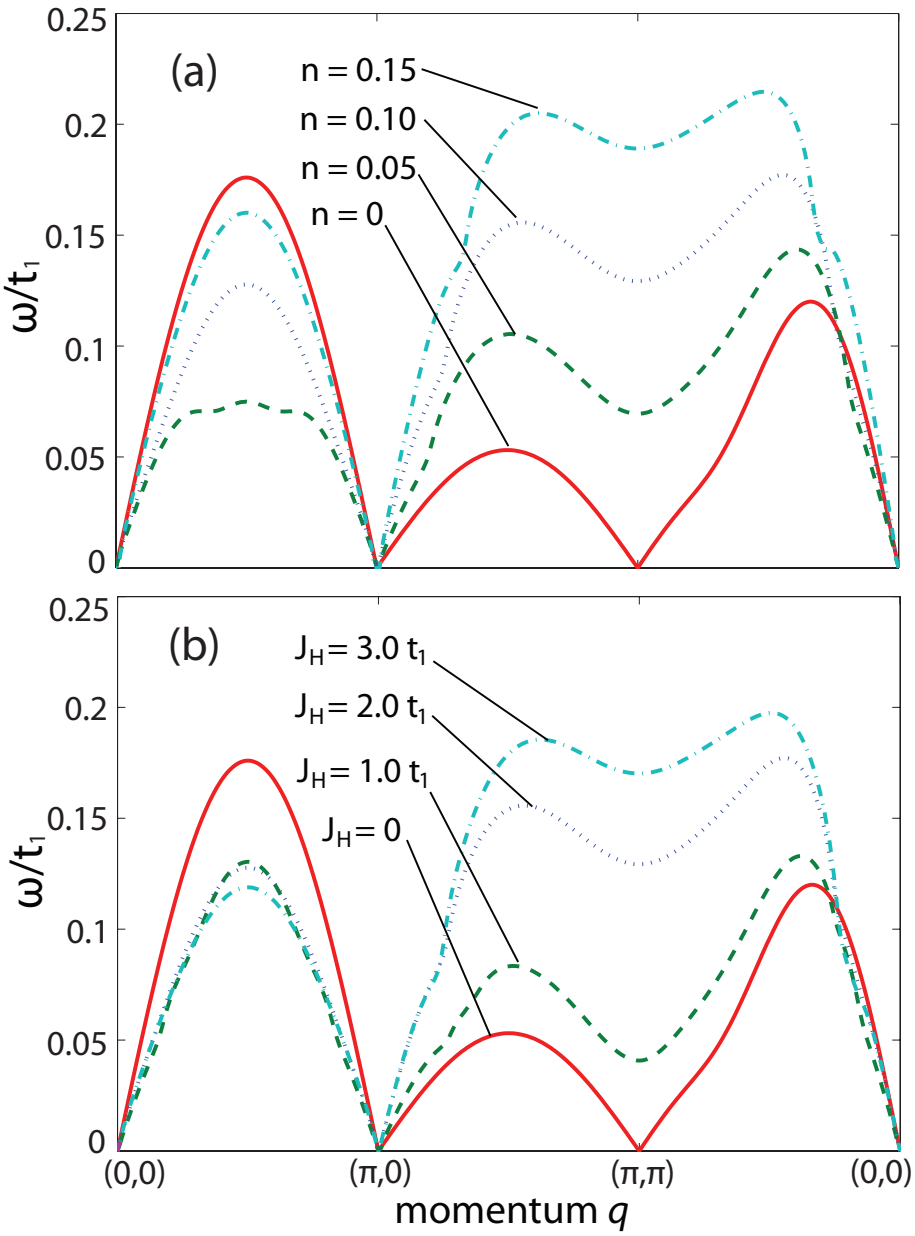

Figure 5.4: Spin-wave energy ω in the unit of t_1 as a function of the momentum q along the path $(0,0)$-$(\pi,0)$-(π,π)-$(0,0)$ in the Brillouin zone containing one Fe atom per unit cell. Both graphs share the following common parameters: the core spin length $S = 1/2$; and the bare exchange constants $J_1 = 0.04t_1$, $J_2 = 0.6J_1$. (a) different filling levels n, $J_{\rm H} = 2.0t_1$; (b) different Hund's couplings $J_{\rm H}$, $n = 0.1$.

the filling level $n = 0.1$. According to Fig. 5.3(c), we have complete orbital polarization for all the $J_{\rm H}$'s used in Fig. 5.4(b), except for $J_{\rm H} = 1.0t_\sigma$. As expected, a larger $J_{\rm H}$ produces stronger corrections to the spin-wave dispersion, especially around (π, π) where the spin-wave energy almost reaches a maximum. In contrast, the dispersion along $(0, 0)$ to $(\pi, 0)$ is almost unaffected after $J_{\rm H}$ reaches some certain value.

5.4.4 Magnetic anisotropy

In Section 5.4.3 we saw that the double exchange leads to a dramatic change of the magnetic excitation spectra. In particular, the spin-wave modes at the Néel antiferromagnetic wave vector (π, π) are almost pushed to a maximum consistent with the neutron-scattering data [81]. Since the orbital ordering leads to a dramatic anisotropy in the electronic structure, the ferromagnetic double-exchange contribution is expected to be much larger along the y-direction along which the ferromagnetic spin chains are formed. To quantify the induced magnetic anisotropy, in this Section, we fit the spin-wave dispersions calculated in the presence of both super- and double-exchange to an effective, anisotropic Heisenberg model, illustrated by the inset of Fig. 5.5(a) where the fitting parameters $\tilde{J}_{1x}$, $\tilde{J}_{1y}$, $\tilde{J}_2$ and $\tilde{J}_{3y}$ are the effective exchange constants of nearest neighbors along the x- and y-direction, next-nearest neighbors, and third-nearest neighbors along the y-direction, respectively. Please note the different symbols used here to distinguish those in the original Heisenberg model $\mathcal{H}_{\rm loc}$ (5.2). Furthermore, we also introduce an additional exchange between the third-nearest neighbors along the y-direction, $\tilde{J}_{3y}$, which will be shown to be slightly negative, in order to get a better fit to the spin-wave spectra. In the relevant regime $\tilde{J}_{1x} > \tilde{J}_{1y}$, $\tilde{J}_{1y} < 2\tilde{J}_2$, $\tilde{J}_{3y} < 0$, where the $(\pi, 0)$ stripe antiferromagnetism is stable, the linear-spin wave dispersion $\tilde{\omega}(q)$ is determined by $\tilde{\omega}^2(q) = \tilde{A}^2(q) - \tilde{B}^2(q)$ with $\tilde{A}(q) = \tilde{J}_{1x} - \tilde{J}_{1y}(1 - \cos q_y) + 2\tilde{J}_2 - \tilde{J}_{3y}(1 - \cos 2q_y)$ and $\tilde{B}(q) = \tilde{J}_{1x} \cos q_x + 2\tilde{J}_2 \cos q_x \cos q_y$.

The necessity of this extra fitting parameter $\tilde{J}_{3y}$ is already known in the ferromagnetic double-exchange model where simple nearest neighbor exchange is unable to reproduce the calculated dispersions from either canonical transformations [230, 231] or diagrammatic perturbations [232]. Indeed, by comparing the fitted spin-wave dispersions with and without $\tilde{J}_{3y}$ to the original calculated one [see Fig. 5.5(a)], we find out that the fitting results are much better behaved with a nonzero $\tilde{J}_{3y}$. The hopping amplitudes and the bare exchanges are the same as those in Fig. 5.4(a) and (b), with the filling $n = 0.1$ and the Hund exchange $J_{\rm H} = 3.0t_1$. In fact, setting $\tilde{J}_{3y} = 0$ gives an unrealistic large correction to the nearest-neighbor exchange along the x-direction ($\tilde{J}_{1x} = -0.27J_1$), which has to be compensated by a fairly substantial increase of the diagonal exchange, $\tilde{J}_2 = 0.90J_1$. This result is certainly unphysical, since we expect a slower decrease of $\tilde{J}_{1x}$ than that of $\tilde{J}_2$ for $t_2 < t_3$ from the classical double-exchange

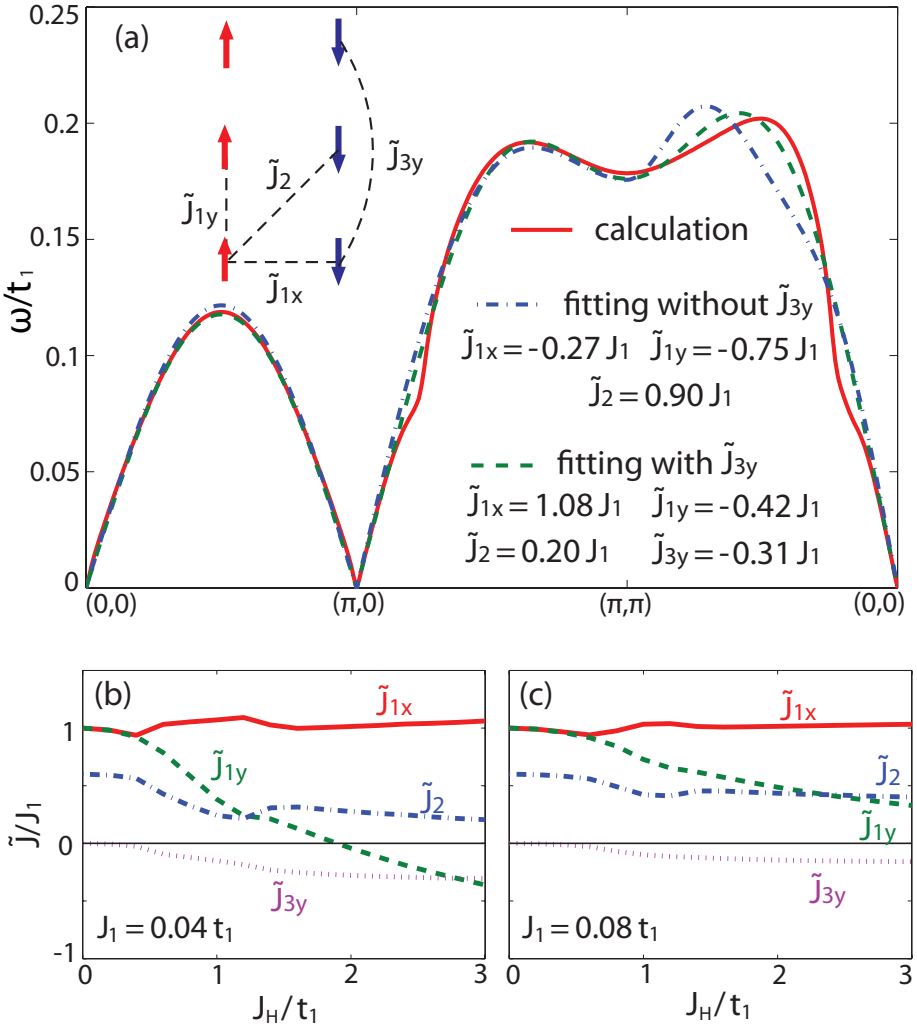

Figure 5.5: (a) The comparison of the fitting results with and without J_{3y} to the original calculated spin-wave dispersion of $n = 0.1$ and $J_{\rm H} = 3.0t_1$. We use the same hopping parameters and bare exchanges as previously. The results of the fitted effective exchanges are written down explicitly in the figure. (Inset: the effective spin-only model with additional third nearest-neighbor coupling along the y-direction, $\tilde{J}_{3y}$.) (b, c) The fitted, effective exchange constants $\tilde{J}_{1x}$, $\tilde{J}_{1y}$, $\tilde{J}_2$ and $\tilde{J}_{3y}$ as functions of the Hund coupling $J_{\rm H}$ for bare exchange constants $J_1 = 0.04t_1$(b) and $J_1 = 0.08t_1$(c). In both cases, the ratio of the bare exchange constants is given by $J_2/J_1 = 0.6$ corresponding to the regime of strong frustration but where the $(\pi, 0)$ stripe order is classically stable.

argument. In contrast, by including $\tilde{J}_{3y}$, we obtain more physical fitting results. Consequently, in the following, all of the fittings will be performed with $\tilde{J}_{3y} \neq 0$.

We further carry out the fitting process for different Hund's couplings, and analyze the dependence of the effective magnetic exchanges on the strength of $J_{\rm H}$. Fig. 5.5(b) displays the fitting results for $J_1 = 0.04t_1$ and $n = 0.1$, corresponding to spin-wave spectra shown in Fig. 5.4(b). As expected, a larger $J_{\rm H}$ causes more significant corrections to the exchange constants. As expected from simple classical arguments of the double-exchange mechanism, $\tilde{J}_{1y}$ changes by the most amount because t_1 produces the strongest effective ferromagnetic exchanges along the y-direction. The modification to $\tilde{J}_{1x}$ is smaller compared to that of $\tilde{J}_2$ as the diagonal hopping t_3 is larger than t_2. These are indeed confirmed by our results shown in Fig. 5.5(b). We also note that the seemingly uncontinuous behavior around $J_{\rm H} \approx 1.0t_1$ is not unphysical, but due to the fact that the complete orbital polarization is not achieved until $J_{\rm H} \gtrsim 1.5t_1$.

Interestingly, for a sufficient strong Hund exchange $J_{\rm H} \gtrsim 2.0t_1$, $\tilde{J}_{1y}$ becomes negative, which completely removes the frustration in the effective spin-only model. Such an effective negative exchange coupling along the ferromagnetic spin direction has been used phenomenologically to rationalize the spectra measured by inelastic neutron scattering [81]. Very remarkably, around $J_{\rm H} \approx 2.0t_1$, the ratio of the three exchange constants $\tilde{J}_{1x}$, $\tilde{J}_{1y}$, and $\tilde{J}_2$, agrees well with the experimental estimates [81] on a quantitative level, except for an additional $\tilde{J}_{3y}$.

The fitting is also performed for a larger bare nearest-neighbor exchange $J_1 = 0.08t_1$, shown in Fig. 5.5(c). In this case, the relative corrections are smaller and $\tilde{J}_{1y}$ never comes to ferromagnetic. In order to achieve the experimentally observed negative $\tilde{J}_{1y}$ within reasonable parameter space, we require $J_1 \lesssim 0.05t_\sigma$. In fact, inelastic neutron scattering [81] suggests that the exchange constants are of the order of 10 meV, which in our theory leads to an electronic bandwidth and a Hund coupling $J_{\rm H}$ both of the order of 1 eV, in agreement with other experimental estimates [38].

Finally, as being discussed before, the spin-wave expansion around $(\pi, 0)$ can still be carried out even when the Heisenberg model alone favors the (π, π) order for $J_2 < J_1/2$, as long as the Hund coupling is sufficient strong so that the kinetic energy of the itinerant electrons wins out the exchange energy of the local moments. We carry out the spin-wave calculations for $J_2 = 0.4J_1$ and filling $n = 0.1$. From the phase diagram in Fig. 5.2, the stripe $(\pi, 0)$ order is stabilized classically for $J_{\rm H} \gtrsim 2.0t_1$. Indeed, in this regime, the calculated spin-wave spectra with both super- and double-exchange are well-behaved as shown in Fig. 5.6. The dispersions are also fitted by a spin-only model, with the effective exchange constants as functions of the Hund coupling $J_{\rm H}$ shown in the inset of Fig. 5.6. However, the result shows no significant difference from that of $J_2 = 0.6J_1$ [Fig. 5.5(b)]. Furthermore, the exact ground state is unknown as strong quantum fluctuations might drive the system to a disordered state.

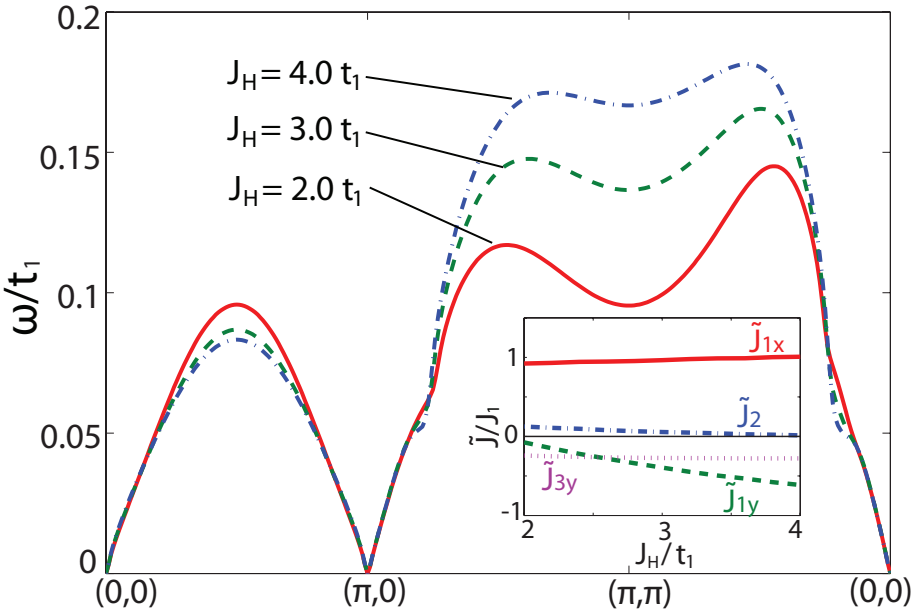

Figure 5.6: Spin-wave energy ω in the unit of t_1 as a function of the momentum q along the path $(0,0)$-$(\pi,0)$-(π,π)-$(0,0)$ in the Brillouin zone containing one Fe atom per unit cell for various $J_{\rm H}$ that are sufficient large to stabilize the $(\pi,0)$ order. We use the bare exchanges $J_1 = 0.04t_1$ and $J_2 = 0.4J_1$, where the Heisenberg model prefers a (π,π) order classically without the presence of the itinerant electrons. (Inset: the fitted, effective exchange constants $\tilde{J}_{1x}$, $\tilde{J}_{1y}$, $\tilde{J}_2$ and $\tilde{J}_{3y}$ as functions of the Hund coupling $J_{\rm H}$.)

Consequently, we will not perform further analysis for the case of $J_2 < J_1/2$ and concentrate our discussions for $J_2 > J_1/2$.

To conclude this Section, we stress that the degenerate double-exchange model explains the strong magnetic anisotropy observed experimentally [81] In a realistic parameter regime, the double-exchange contribution along the ferromagnetic direction can exceed the bare antiferromagnetic super-exchange, J_1, leading to an effective exchange $\tilde{J}_{1y}$ which is slightly ferromagnetic, consistent with the experimental data. In this regime, the $(\pi,0)$ antiferromagnetism is unfrustrated.

5.5 Discussion and conclusion

In summary, we have studied a degenerate double-exchange model for the iron pnictides which explains the dramatic magnetic [81, 109] and electronic [111, 119] anisotropies in these materials. The model consists of local moments which are coupled by antiferromagnetic super-exchanges J_1 and J_2 between nearest- and next-nearest-neighbor spins, respectively, and of itinerant electrons in the bands of the degenerate d_{xz} and d_{yz} orbitals. The electrons are coupled to the local moments by a ferromagnetic Hund exchange, J_H. The system spontaneously

develops ferro-orbital order because of the kinetic energy gained by directing the itinerant electrons along ferromagnetic spin chains which are stabilized by the double-exchange mechanism.

The calculated spin-wave spectra in the presence of both super- and double-exchange are found to be in good agreement with the neutron-scattering data [81, 109]. In particular, we find that the spin-wave dispersion is pushed almost to a local maximum at the competing Néel ordering wave vector as seen in the experiment [81]. This stabilization of $(\pi, 0)$-antiferromagnetic order results from the strong anisotropy in the electronic sector which makes the ferromagnetic double-exchange much stronger along the y-direction. Remarkably, in a realistic parameter regime, we find that the ferromagnetic double-exchange can exceed the super-exchange J_1 between the local moments leading to a slightly ferromagnetic exchange $\tilde{J}_{1y}$ along the y-direction in an effective spin-only model. In this regime, the $(\pi, 0)$ antiferromagnetism is unfrustrated.

It is feasible that the parent, undoped materials self-tune the size of the local moments and the carrier density to the point where the $(\pi, 0)$ antiferromagnetism is most stable. In our theory, this is the case for the optimal filling level $n = \bar{n}$. In fact, the starting Heisenberg model $\mathcal{H}_{\rm loc}$ (5.2) is likely to be in the regime of strong frustration, $J_2 \sim 0.5 J_1$, leading to a spin disordered ground state in the absence of itinerant electrons. Only through interaction with the ferro-orbital ordered itinerant bands, does the stripe antiferromagnetism emerge. Electron or hole doping the system at $n = \bar{n}$ diminishes the orbital order and thus increases the magnetic frustration, lowering the transition temperature to a spin-ordered state.

We conclude by stressing that the degenerate double-exchange model motivated and studied in this work qualitatively explains many properties of the undoped and slightly doped iron pnictides. The emergent ferro-orbital order breaks the in plane lattice symmetry, thereby driving the orthorhombic lattice distortion. Further, orbital order induces a strong electronic anisotropy which explains why the structural transition is accompanied by dramatic Fermi-surface reconstructions [135] and transport anomalies [224]. Moreover, recent STM experiments [111] and in-plane resistivity measurements [119, 120] have unambiguously demonstrated the spatial anisotropy of the electronic structure below the structural transition temperature. Finally, the orbital ordering produces the strong magnetic anisotropy, essential to explain the experimentally observed magnetic excitation spectra [81, 109].

During the review of this work, several mean-field calculations [132, 137, 163] based on the five-orbital model have shown that the total occupations of the d_{xz} and d_{yz} orbitals are close to each other, but there is a significant difference in the densities of the states for the two orbitals at the chemical potential. The ferro-orbital order in our theory does not contradict these results. In fact, by viewing the itinerant electrons as quasiparticles, our model is an effective low-energy theory that successfully describes the strong anisotropic electron state

around the Fermi surface.

References

[1] Y. Kamihara, T. Watanabe, M. Hirano, and H. Hosono, "Iron-Based Layered Superconductor La[$O_{1-x}F_x$]FeAs (x = 0.05-0.12) with T_c = 26 K", *Journal of the American Chemical Society* **130**, 3296 (2008).

[2] M. R. Norman, "High-temperature superconductivity in the iron pnictides", *Physics* **1**, 21 (2008).

[3] K. Ishida, Y. Nakai, and H. Hosono, "To What Extent Iron-Pnictide New Superconductors Have Been Clarified: A Progress Report", *Journal of the Physical Society of Japan* **78**, 062001 (2009).

[4] J. Paglione and R. L. Greene, "High-temperature superconductivity in iron-based materials", *Nature Physics* **6**, 645 (2010).

[5] D. C. Johnston, "The puzzle of high temperature superconductivity in layered iron pnictides and chalcogenides", *Advances in Physics* **59**, 803 (2010).

[6] G. R. Stewart, "Superconductivity in iron compounds", *Rev. Mod. Phys.* **83**, 1589 (2011).

[7] H. Takahashi, K. Igawa, K. Arii, Y. Kamihara, M. Hirano, and H. Hosono, "Superconductivity at 43 K in an iron-based layered compound $LaO_{1-x}F_xFeAs$", *Nature* **453**, 376 (2008).

[8] X. H. Chen, T. Wu, G. Wu, R. H. Liu, H. Chen, and D. F. Fang, "Superconductivity at 43 K in $SmFeAsO_{1-x}F_x$", *Nature* **453**, 761 (2008).

[9] G. F. Chen, Z. Li, D. Wu, G. Li, W. Z. Hu, J. Dong, P. Zheng, J. L. Luo, and N. L. Wang, "Superconductivity at 41 K and Its Competition with Spin-Density-Wave Instability in Layered $CeO_{1-x}F_xFeAs$", *Phys. Rev. Lett.* **100**, 247002 (2008).

[10] Z.-A. Ren, J. Yang, W. Lu, W. Yi, X.-L. Shen, Z.-C. Li, G.-C. Che, X.-L. Dong, L.-L. Sun, F. Zhou, and Z.-X. Zhao, "Superconductivity in the iron-based F-doped layered quaternary compound Nd[$O_{1-x}F_x$]FeAs", *EPL (Europhysics Letters)* **82**, 57002 (2008).

[11] Z.-A. Ren, W. Lu, J. Yang, W. Yi, X.-L. Shen, Z.-C. Li, G.-C. Che, X.-L. Dong, L.-L. Sun, F. Zhou, and Z.-X. Zhao, "Superconductivity at 55 K in Iron-Based F-Doped Layered Quaternary Compound Sm[$O_{1-x}F_x$]FeAs", *Chinese Physics Letters* **25**, 2215 (2008).

[12] M. Rotter, M. Tegel, D. Johrendt, I. Schellenberg, W. Hermes, and R. Pöttgen, "Spin-density-wave anomaly at 140 K in the ternary iron arsenide $BaFe_2As_2$", *Phys. Rev. B* **78**, 020503 (2008).

[13] M. Rotter, M. Tegel, and D. Johrendt, "Superconductivity at 38 K in the Iron Arsenide ($Ba_{1-x}K_x$)Fe_2As_2", *Phys. Rev. Lett.* **101**, 107006 (2008).

[14] X. Wang, Q. Liu, Y. Lv, W. Gao, L. Yang, R. Yu, F. Li, and C. Jin, "The superconductivity at 18 K in LiFeAs system", *Solid State Communications* **148**, 538 (2008).

[15] J. H. Tapp, Z. Tang, B. Lv, K. Sasmal, B. Lorenz, P. C. W. Chu, and A. M. Guloy, "LiFeAs: An intrinsic FeAs-based superconductor with $T_c = 18$ K", *Phys. Rev. B* **78**, 060505 (2008).

[16] F.-C. Hsu, J.-Y. Luo, K.-W. Yeh, T.-K. Chen, T.-W. Huang, P. M. Wu, Y.-C. Lee, Y.-L. Huang, Y.-Y. Chu, D.-C. Yan, and M.-K. Wu, "Superconductivity in the PbO-type structure α-FeSe", *Proceedings of the National Academy of Sciences* **105**, 14262 (2008).

[17] P. M. Shirage, K. Kihou, C.-H. Lee, H. Kito, H. Eisaki, and A. Iyo, "Emergence of Superconductivity in "32522" Structure of ($Ca_3Al_2O_{5-y}$)(Fe_2Pn_2) (Pn = As and P)", *Journal of the American Chemical Society* **133**, 9630 (2011).

[18] N. Ni, J. M. Allred, B. C. Chan, and R. J. Cava, "High T_c electron doped $Ca_{10}(Pt_3As_8)(Fe_2As_2)_5$ and $Ca_{10}(Pt_4As_8)(Fe_2As_2)_5$ superconductors with skutterudite intermediary layers", *Proceedings of the National Academy of Sciences* **108**, E1019 (2011).

[19] J. Zhao, Q. Huang, C. de la Cruz, S. Li, J. W. Lynn, Y. Chen, M. A. Green, G. F. Chen, G. Li, Z. Li, J. L. Luo, N. L. Wang, and P. Dai, "Structural and magnetic phase diagram of $CeFeAsO_{1-x}F_x$ and its relation to high-temperature superconductivity", *Nature Materials* **7**, 953 (2008).

[20] S. Nandi, M. G. Kim, A. Kreyssig, R. M. Fernandes, D. K. Pratt, A. Thaler, N. Ni, S. L. Bud'ko, P. C. Canfield, J. Schmalian, R. J. McQueeney, and A. I. Goldman, "Anomalous Suppression of the Orthorhombic Lattice Distortion in Superconducting $Ba(Fe_{1-x}Co_x)_2As_2$ Single Crystals", *Phys. Rev. Lett.* **104**, 057006 (2010).

[21] C. de la Cruz, Q. Huang, J. W. Lynn, J. Li, W. R. II, J. L. Zarestky, H. A. Mook, G. F. Chen, J. L. Luo, N. L. Wang, and P. Dai, "Magnetic order close to superconductivity in the iron-based layered $LaO_{1-x}F_xFeAs$ systems", *Nature* **453**, 899 (2008).

[22] Q. Huang, Y. Qiu, W. Bao, M. A. Green, J. W. Lynn, Y. C. Gasparovic, T. Wu, G. Wu, and X. H. Chen, "Neutron-Diffraction Measurements of Magnetic Order and a Structural Transition in the Parent $BaFe_2As_2$ Compound of FeAs-Based High-Temperature Superconductors", *Phys. Rev. Lett.* **101**, 257003 (2008).

[23] A. I. Goldman, D. N. Argyriou, B. Ouladdiaf, T. Chatterji, A. Kreyssig, S. Nandi, N. Ni, S. L. Bud'ko, P. C. Canfield, and R. J. McQueeney, "Lattice and magnetic instabilities in $CaFe_2As_2$: A single-crystal neutron diffraction study", *Phys. Rev. B* **78**, 100506 (2008).

[24] S. Li, C. de la Cruz, Q. Huang, Y. Chen, J. W. Lynn, J. Hu, Y.-L. Huang, F.-C. Hsu, K.-W. Yeh, M.-K. Wu, and P. Dai, "First-order magnetic and structural phase transitions in $Fe_{1+y}Se_xTe_{1-x}$", *Phys. Rev. B* **79**, 054503 (2009).

[25] W. Bao, Y. Qiu, Q. Huang, M. A. Green, P. Zajdel, M. R. Fitzsimmons, M. Zhernenkov, S. Chang, M. Fang, B. Qian, E. K. Vehstedt, J. Yang, H. M. Pham, L. Spinu, and Z. Q. Mao, "Tunable ($\delta\pi$, $\delta\pi$)-Type Antiferromagnetic Order in α-Fe(Te,Se) Superconductors", *Phys. Rev. Lett.* **102**, 247001 (2009).

[26] M. G. Kim, R. M. Fernandes, A. Kreyssig, J. W. Kim, A. Thaler, S. L. Bud'ko, P. C. Canfield, R. J. McQueeney, J. Schmalian, and A. I. Goldman, "Character of the structural and magnetic phase transitions in the parent and electron-doped $BaFe_2As_2$ compounds", *Phys. Rev. B* **83**, 134522 (2011).

[27] C. R. Rotundu and R. J. Birgeneau, "First- and second-order magnetic and structural transitions in $BaFe_{2(1-x)}Co_{2x}As_2$", *Phys. Rev. B* **84**, 092501 (2011).

[28] T. M. McQueen, A. J. Williams, P. W. Stephens, J. Tao, Y. Zhu, V. Ksenofontov, F. Casper, C. Felser, and R. J. Cava, "Tetragonal-to-Orthorhombic Structural Phase Transition at 90 K in the Superconductor $Fe_{1.01}Se$", *Phys. Rev. Lett.* **103**, 057002 (2009).

[29] N. F. Berk and J. R. Schrieffer, "Effect of Ferromagnetic Spin Correlations on Superconductivity", *Phys. Rev. Lett.* **17**, 433 (1966).

[30] D. Scalapino, "Superconductivity and Spin Fluctuations", *Journal of Low Temperature Physics* **117**, 179 (1999).

[31] I. I. Mazin, D. J. Singh, M. D. Johannes, and M. H. Du, "Unconventional Superconductivity with a Sign Reversal in the Order Parameter of $LaFeAsO_{1-x}F_x$", *Phys. Rev. Lett.* **101**, 057003 (2008).

[32] H. Kontani and S. Onari, "Orbital-Fluctuation-Mediated Superconductivity in Iron Pnictides: Analysis of the Five-Orbital Hubbard-Holstein Model", *Phys. Rev. Lett.* **104**, 157001 (2010).

[33] P. J. Hirschfeld, M. M. Korshunov, and I. I. Mazin, "Gap symmetry and structure of Fe-based superconductors", *Reports on Progress in Physics* **74**, 124508 (2011).

[34] A. Chubukov, "Pairing Mechanism in Fe-Based Superconductors", *Annual Review of Condensed Matter Physics* **3**, 57 (2012).

[35] D. J. Singh and M.-H. Du, "Density Functional Study of $LaFeAsO_{1-x}F_x$: A Low Carrier Density Superconductor Near Itinerant Magnetism", *Phys. Rev. Lett.* **100**, 237003 (2008).

[36] D. H. Lu, M. Yi, S.-K. Mo, A. S. Erickson, J. Analytis, J.-H. Chu, D. J. Singh, Z. Hussain, T. H. Geballe, I. R. Fisher, and Z.-X. Shen, "Electronic structure of the iron-based superconductor LaOFeP", *Nature* **455**, 81 (2008).

[37] M. M. Qazilbash, J. J. Hamlin, R. E. Baumbach, L. Zhang, D. J. Singh, M. B. Maple, and D. N. Basov, "Electronic correlations in the iron pnictides", *Nature Physics* **5**, 647 (2009).

[38] W. L. Yang, A. P. Sorini, C.-C. Chen, B. Moritz, W.-S. Lee, F. Vernay, P. Olalde-Velasco, J. D. Denlinger, B. Delley, J.-H. Chu, J. G. Analytis, I. R. Fisher, Z. A. Ren, J. Yang, W. Lu, Z. X. Zhao, J. van den Brink,

Z. Hussain, Z.-X. Shen, and T. P. Devereaux, "Evidence for weak electronic correlations in iron pnictides", *Phys. Rev. B* **80**, 014508 (2009).

[39] V. Cvetkovic and Z. Tesanovic, "Multiband magnetism and superconductivity in Fe-based compounds", *EPL (Europhysics Letters)* **85**, 37002 (2009).

[40] P. A. Lee and X.-G. Wen, "Spin-triplet p-wave pairing in a three-orbital model for iron pnictide superconductors", *Phys. Rev. B* **78**, 144517 (2008).

[41] S. Raghu, X.-L. Qi, C.-X. Liu, D. J. Scalapino, and S.-C. Zhang, "Minimal two-band model of the superconducting iron oxypnictides", *Phys. Rev. B* **77**, 220503 (2008).

[42] Y. Ran, F. Wang, H. Zhai, A. Vishwanath, and D.-H. Lee, "Nodal spin density wave and band topology of the FeAs-based materials", *Phys. Rev. B* **79**, 014505 (2009).

[43] A. Moreo, M. Daghofer, J. A. Riera, and E. Dagotto, "Properties of a two-orbital model for oxypnictide superconductors: Magnetic order, B_{2g} spin-singlet pairing channel, and its nodal structure", *Phys. Rev. B* **79**, 134502 (2009).

[44] M. Daghofer, A. Nicholson, A. Moreo, and E. Dagotto, "Three orbital model for the iron-based superconductors", *Phys. Rev. B* **81**, 014511 (2010).

[45] R. Yu, K. T. Trinh, A. Moreo, M. Daghofer, J. A. Riera, S. Haas, and E. Dagotto, "Magnetic and metallic state at intermediate Hubbard U coupling in multiorbital models for undoped iron pnictides", *Phys. Rev. B* **79**, 104510 (2009).

[46] K. Kuroki, S. Onari, R. Arita, H. Usui, Y. Tanaka, H. Kontani, and H. Aoki, "Unconventional Pairing Originating from the Disconnected Fermi Surfaces of Superconducting $LaFeAsO_{1-x}F_x$", *Phys. Rev. Lett.* **101**, 087004 (2008).

[47] S. Graser, T. A. Maier, P. J. Hirschfeld, and D. J. Scalapino, "Near-degeneracy of several pairing channels in multiorbital models for the Fe pnictides", *New Journal of Physics* **11**, 025016 (2009).

[48] M. J. Calderón, B. Valenzuela, and E. Bascones, "Tight-binding model for iron pnictides", *Phys. Rev. B* **80**, 094531 (2009).

[49] H. Eschrig and K. Koepernik, "Tight-binding models for the iron-based superconductors", *Phys. Rev. B* **80**, 104503 (2009).

[50] S. Graser, A. F. Kemper, T. A. Maier, H.-P. Cheng, P. J. Hirschfeld, and D. J. Scalapino, "Spin fluctuations and superconductivity in a three-dimensional tight-binding model for $BaFe_2As_2$", *Phys. Rev. B* **81**, 214503 (2010).

[51] Q. Luo, G. Martins, D.-X. Yao, M. Daghofer, R. Yu, A. Moreo, and E. Dagotto, "Neutron and ARPES constraints on the couplings of the multiorbital Hubbard model for the iron pnictides", *Phys. Rev. B* **82**, 104508 (2010).

[52] A. M. Oleś, "Antiferromagnetism and correlation of electrons in transition metals", *Phys. Rev. B* **28**, 327 (1983).

[53] E. Kaneshita and T. Tohyama, "Spin and charge dynamics ruled by antiferromagnetic order in iron pnictide superconductors", *Phys. Rev. B* **82**, 094441 (2010).

[54] K. Kubo, "Pairing symmetry in a two-orbital Hubbard model on a square lattice", *Phys. Rev. B* **75**, 224509 (2007).

[55] J. R. Schrieffer, X. G. Wen, and S. C. Zhang, "Dynamic spin fluctuations and the bag mechanism of high-T_c superconductivity", *Phys. Rev. B* **39**, 11663 (1989).

[56] A. V. Chubukov and D. M. Frenkel, "Renormalized perturbation theory of magnetic instabilities in the two-dimensional Hubbard model at small doping", *Phys. Rev. B* **46**, 11884 (1992).

[57] A. F. Kemper, T. A. Maier, S. Graser, H.-P. Cheng, P. J. Hirschfeld, and D. J. Scalapino, "Sensitivity of the superconducting state and magnetic susceptibility to key aspects of electronic structure in ferropnictides", *New Journal of Physics* **12**, 073030 (2010).

[58] K. Kuroki, H. Usui, S. Onari, R. Arita, and H. Aoki, "Pnictogen height as a possible switch between high-T_c nodeless and low-T_c nodal pairings in the iron-based superconductors", *Phys. Rev. B* **79**, 224511 (2009).

[59] H. Ding, P. Richard, K. Nakayama, K. Sugawara, T. Arakane, Y. Sekiba, A. Takayama, S. Souma, T. Sato, T. Takahashi, Z. Wang, X. Dai, Z. Fang, G. F. Chen, J. L. Luo, and N. L. Wang, "Observation of Fermi-surfacedependent nodeless superconducting gaps in $Ba_{0.6}K_{0.4}Fe_2As_2$", *EPL (Europhysics Letters)* **83**, 47001 (2008).

[60] C.-T. Chen, C. C. Tsuei, M. B. Ketchen, Z.-A. Ren, and Z. X. Zhao, "Integer and half-integer flux-quantum transitions in a niobium-iron pnictide loop", *Nature Physics* **6**, 260 (2010).

[61] A. D. Christianson, E. A. Goremychkin, R. Osborn, S. Rosenkranz, M. D. Lumsden, C. D. Malliakas, I. S. Todorov, H. Claus, D. Y. Chung, M. G. Kanatzidis, R. I. Bewley, and T. Guidi, "Unconventional superconductivity in $Ba_{0.6}K_{0.4}Fe_2As_2$ from inelastic neutron scattering", *Nature* **456**, 930 (2008).

[62] T. Hanaguri, S. Niitaka, K. Kuroki, and H. Takagi, "Unconventional s-Wave Superconductivity in Fe(Se,Te)", *Science* **328**, 474 (2010).

[63] K. Suzuki, H. Usui, and K. Kuroki, "Spin fluctuations and unconventional pairing in KFe_2As_2", *Phys. Rev. B* **84**, 144514 (2011).

[64] T. A. Maier, S. Graser, P. J. Hirschfeld, and D. J. Scalapino, "*d*-wave pairing from spin fluctuations in the $K_xFe_{2-y}Se_2$ superconductors", *Phys. Rev. B* **83**, 100515 (2011).

[65] Y. Zhang, L. X. Yang, M. Xu, Z. R. Ye, F. Chen, C. He, H. C. Xu, J. Jiang, B. P. Xie, J. J. Ying, X. F. Wang, X. H. Chen, J. P. Hu, M. Matsunami, S. Kimura, and D. L. Feng, "Nodeless superconducting gap in $A_xFe_2Se_2$ (A=K,Cs) revealed by angle-resolved photoemission spectroscopy", *Nature Materials* **10**, 273 (2011).

[66] W. Metzner, M. Salmhofer, C. Honerkamp, V. Meden, and K. Schönhammer, "Functional renormalization group approach to correlated fermion systems", *Rev. Mod. Phys.* **84**, 299 (2012).

[67] F. Wang, H. Zhai, Y. Ran, A. Vishwanath, and D.-H. Lee, "Functional Renormalization-Group Study of the Pairing Symmetry and Pairing Mechanism of the FeAs-Based High-Temperature Superconductor", *Phys. Rev. Lett.* **102**, 047005 (2009).

[68] H. Zhai, F. Wang, and D.-H. Lee, "Antiferromagnetically driven electronic correlations in iron pnictides and cuprates", *Phys. Rev. B* **80**, 064517 (2009).

[69] F. Wang, F. Yang, M. Gao, Z.-Y. Lu, T. Xiang, and D.-H. Lee, "The electron pairing of $K_xFe_{2-y}Se_2$", *EPL (Europhysics Letters)* **93**, 57003 (2011).

[70] R. Thomale, C. Platt, W. Hanke, and B. A. Bernevig, "Mechanism for Explaining Differences in the Order Parameters of FeAs-Based and FeP-Based Pnictide Superconductors", *Phys. Rev. Lett.* **106**, 187003 (2011).

[71] R. Thomale, C. Platt, W. Hanke, J. Hu, and B. A. Bernevig, "Exotic *d*-Wave Superconducting State of Strongly Hole-Doped $\mathbf{K}_xBa_{1-x}Fe_2As_2$", *Phys. Rev. Lett.* **107**, 117001 (2011).

[72] A. V. Chubukov, D. V. Efremov, and I. Eremin, "Magnetism, superconductivity, and pairing symmetry in iron-based superconductors", *Phys. Rev. B* **78**, 134512 (2008).

[73] D. Parker, M. G. Vavilov, A. V. Chubukov, and I. I. Mazin, "Coexistence of superconductivity and a spin-density wave in pnictide superconductors: Gap symmetry and nodal lines", *Phys. Rev. B* **80**, 100508 (2009).

[74] A. B. Vorontsov, M. G. Vavilov, and A. V. Chubukov, "Superconductivity and spin-density waves in multiband metals", *Phys. Rev. B* **81**, 174538 (2010).

[75] R. M. Fernandes, D. K. Pratt, W. Tian, J. Zarestky, A. Kreyssig, S. Nandi, M. G. Kim, A. Thaler, N. Ni, P. C. Canfield, R. J. McQueeney, J. Schmalian, and A. I. Goldman, "Unconventional pairing in the iron arsenide superconductors", *Phys. Rev. B* **81**, 140501 (2010).

[76] R. M. Fernandes and J. Schmalian, "Transfer of optical spectral weight in magnetically ordered superconductors", *Phys. Rev. B* **82**, 014520 (2010).

[77] R. M. Fernandes and J. Schmalian, "Competing order and nature of the pairing state in the iron pnictides", *Phys. Rev. B* **82**, 014521 (2010).

[78] S. Maiti, M. M. Korshunov, T. A. Maier, P. J. Hirschfeld, and A. V. Chubukov, "Evolution of the Superconducting State of Fe-Based Compounds with Doping", *Phys. Rev. Lett.* **107**, 147002 (2011).

[79] S. Maiti, M. M. Korshunov, T. A. Maier, P. J. Hirschfeld, and A. V. Chubukov, "Evolution of symmetry and structure of the gap in iron-based superconductors with doping and interactions", *Phys. Rev. B* **84**, 224505 (2011).

[80] Y. Xia, D. Qian, L. Wray, D. Hsieh, G. F. Chen, J. L. Luo, N. L. Wang, and M. Z. Hasan, "Fermi Surface Topology and Low-Lying Quasiparticle Dynamics of Parent $Fe_{1+x}Te/Se$ Superconductor", *Phys. Rev. Lett.* **103**, 037002 (2009).

[81] J. Zhao, D. T. Adroja, D.-X. Yao, R. Bewley, S. Li, X. F. Wang, G. Wu, X. H. Chen, J. Hu, and P. Dai, "Spin waves and magnetic exchange interactions in $CaFe_2As_2$", *Nature Physics* **5**, 555 (2009).

[82] T. Shimojima, F. Sakaguchi, K. Ishizaka, Y. Ishida, T. Kiss, M. Okawa, T. Togashi, C.-T. Chen, S. Watanabe, M. Arita, K. Shimada, H. Namatame, M. Taniguchi, K. Ohgushi, S. Kasahara, T. Terashima, T. Shibauchi, Y. Matsuda, A. Chainani, and S. Shin, "Orbital-Independent Superconducting Gaps in Iron Pnictides", *Science* **332**, 564 (2011).

[83] K. Haule, J. H. Shim, and G. Kotliar, "Correlated Electronic Structure of $LaO_{1-x}F_xFeAs$", *Phys. Rev. Lett.* **100**, 226402 (2008).

[84] Q. Si and E. Abrahams, "Strong Correlations and Magnetic Frustration in the High T_c Iron Pnictides", *Phys. Rev. Lett.* **101**, 076401 (2008).

[85] D.-X. Yao and E. W. Carlson, "Magnetic excitations in the high-T_c iron pnictides", *Phys. Rev. B* **78**, 052507 (2008).

[86] K. Seo, B. A. Bernevig, and J. Hu, "Pairing Symmetry in a Two-Orbital Exchange Coupling Model of Oxypnictides", *Phys. Rev. Lett.* **101**, 206404 (2008).

[87] P. Chandra and B. Doucot, "Possible spin-liquid state at large S for the frustrated square Heisenberg lattice", *Phys. Rev. B* **38**, 9335 (1988).

[88] G. Baskaran, Z. Zou, and P. Anderson, "The resonating valence bond state and high-Tc superconductivity - A mean field theory", *Solid State Communications* **63**, 973 (1987).

[89] G. Kotliar, "Resonating valence bonds and d-wave superconductivity", *Phys. Rev. B* **37**, 3664 (1988).

[90] P. Goswami, P. Nikolic, and Q. Si, "Superconductivity in multi-orbital t-J_1-J_2 model and its implications for iron pnictides", *EPL (Europhysics Letters)* **91**, 37006 (2010).

[91] R. Yu, P. Goswami, Q. Si, P. Nikolic, and J.-X. Zhu, "Pairing strength and symmetries of (K,Tl)Fe_xSe_2 in comparison with iron pnictides", arXiv:1103.3259.

[92] C. Fang, Y.-L. Wu, R. Thomale, B. A. Bernevig, and J. Hu, "Robustness of s-Wave Pairing in Electron-Overdoped $A_{1-y}Fe_{2-x}Se_2$ (A=K,Cs)", *Phys. Rev. X* **1**, 011009 (2011).

[93] Y. Zhou, W.-Q. Chen, and F.-C. Zhang, "Symmetry of superconducting states with two orbitals on a tetragonal lattice: Application to $LaFeAsO_{1-x}F_x$", *Phys. Rev. B* **78**, 064514 (2008).

[94] K. I. Kugel and D. I. Khomskii, "The Jahn-Teller effect and magnetism: transition metal compounds", *Soviet Physics Uspekhi* **25**, 231 (1982).

[95] J. Wu, P. Phillips, and A. H. C. Neto, "Theory of the Magnetic Moment in Iron Pnictides", *Phys. Rev. Lett.* **101**, 126401 (2008).

[96] J. Dai, Q. Si, J.-X. Zhu, and E. Abrahams, "Iron pnictides as a new setting for quantum criticality", *Proceedings of the National Academy of Sciences* **106**, 4118 (2009).

[97] S.-P. Kou, T. Li, and Z.-Y. Weng, "Coexistence of itinerant electrons and local moments in iron-based superconductors", *EPL (Europhysics Letters)* **88**, 17010 (2009).

[98] F. Yang, S.-P. Kou, and Z.-Y. Weng, "Collective spin mode in a multicomponent system of coupled itinerant and localized electrons", *Phys. Rev. B* **81**, 245130 (2010).

[99] S. O. Diallo, D. K. Pratt, R. M. Fernandes, W. Tian, J. L. Zarestky, M. Lumsden, T. G. Perring, C. L. Broholm, N. Ni, S. L. Bud'ko, P. C. Canfield, H.-F. Li, D. Vaknin, A. Kreyssig, A. I. Goldman, and R. J. McQueeney, "Paramagnetic spin correlations in $CaFe_2As_2$ single crystals", *Phys. Rev. B* **81**, 214407 (2010).

[100] L. W. Harriger, H. Q. Luo, M. S. Liu, C. Frost, J. P. Hu, M. R. Norman, and P. Dai, "Nematic spin fluid in the tetragonal phase of $BaFe_2As_2$", *Phys. Rev. B* **84**, 054544 (2011).

[101] R. A. Ewings, T. G. Perring, J. Gillett, S. D. Das, S. E. Sebastian, A. E. Taylor, T. Guidi, and A. T. Boothroyd, "Itinerant spin excitations in $SrFe_2As_2$ measured by inelastic neutron scattering", *Phys. Rev. B* **83**, 214519 (2011).

[102] Y.-Z. You, F. Yang, S.-P. Kou, and Z.-Y. Weng, "Magnetic and superconducting instabilities in a hybrid model of itinerant/localized electrons for iron pnictides", *Phys. Rev. B* **84**, 054527 (2011).

[103] W. Lv, F. Krüger, and P. Phillips, "Orbital ordering and unfrustrated $(\pi, 0)$ magnetism from degenerate double exchange in the iron pnictides", *Phys. Rev. B* **82**, 045125 (2010).

[104] W.-G. Yin, C.-C. Lee, and W. Ku, "Unified Picture for Magnetic Correlations in Iron-Based Superconductors", *Phys. Rev. Lett.* **105**, 107004 (2010).

[105] V. Oganesyan, S. A. Kivelson, and E. Fradkin, "Quantum theory of a nematic Fermi fluid", *Phys. Rev. B* **64**, 195109 (2001).

[106] S. A. Kivelson, E. Fradkin, and V. J. Emery, "Electronic liquid-crystal phases of a doped Mott insulator", *Nature* **393**, 550 (1998).

[107] E. Fradkin, S. A. Kivelson, M. J. Lawler, J. P. Eisenstein, and A. P. Mackenzie, "Nematic Fermi Fluids in Condensed Matter Physics", *Annual Review of Condensed Matter Physics* **1**, 153 (2010).

[108] I. R. Fisher, L. Degiorgi, and Z. X. Shen, "In-plane electronic anisotropy of underdoped '122' Fe-arsenide superconductors revealed by measurements of detwinned single crystals", *Reports on Progress in Physics* **74**, 124506 (2011).

[109] J. Zhao, D.-X. Yao, S. Li, T. Hong, Y. Chen, S. Chang, W. Ratcliff, J. W. Lynn, H. A. Mook, G. F. Chen, J. L. Luo, N. L. Wang, E. W. Carlson, J. Hu, and P. Dai, "Low Energy Spin Waves and Magnetic Interactions in $SrFe_2As_2$", *Phys. Rev. Lett.* **101**, 167203 (2008).

[110] J. E. Hoffman, "Spectroscopic scanning tunneling microscopy insights into Fe-based superconductors", *Reports on Progress in Physics* **74**, 124513 (2011).

[111] T.-M. Chuang, M. P. Allan, J. Lee, Y. Xie, N. Ni, S. L. Bud'ko, G. S. Boebinger, P. C. Canfield, and J. C. Davis, "Nematic Electronic Structure in the "Parent" State of the Iron-Based Superconductor $Ca(Fe_{1-x}Co_x)_2As_2$", *Science* **327**, 181 (2010).

[112] I. I. Mazin, S. A. J. Kimber, and D. N. Argyriou, "Quasiparticle interference in antiferromagnetic parent compounds of iron-based superconductors", *Phys. Rev. B* **83**, 052501 (2011).

[113] J. Knolle, I. Eremin, A. Akbari, and R. Moessner, "Quasiparticle Interference in the Spin-Density Wave Phase of Iron-Based Superconductors", *Phys. Rev. Lett.* **104**, 257001 (2010).

[114] X. Zhou, C. Ye, P. Cai, X. Wang, X. Chen, and Y. Wang, "Quasiparticle Interference of C_2-Symmetric Surface States in a LaOFeAs Parent Compound", *Phys. Rev. Lett.* **106**, 087001 (2011).

[115] C.-L. Song, Y.-L. Wang, P. Cheng, Y.-P. Jiang, W. Li, T. Zhang, Z. Li, K. He, L. Wang, J.-F. Jia, H.-H. Hung, C. Wu, X. Ma, X. Chen, and Q.-K. Xue, "Direct Observation of Nodes and Twofold Symmetry in FeSe Superconductor", *Science* **332**, 1410 (2011).

[116] D. Chowdhury, E. Berg, and S. Sachdev, "Nematic order in the vicinity of a vortex in superconducting FeSe", *Phys. Rev. B* **84**, 205113 (2011).

[117] H.-H. Hung, C.-L. Song, X. Chen, X. Ma, Q.-k. Xue, and C. Wu, "Anisotropic vortex lattice structures in the FeSe superconductor", *Phys. Rev. B* **85**, 104510 (2012).

[118] J.-H. Chu, J. G. Analytis, D. Press, K. De Greve, T. D. Ladd, Y. Yamamoto, and I. R. Fisher, "In-plane electronic anisotropy in underdoped $Ba(Fe_{1-x}Co_x)_2As_2$ revealed by partial detwinning in a magnetic field", *Phys. Rev. B* **81**, 214502 (2010).

[119] J.-H. Chu, J. G. Analytis, K. De Greve, P. L. McMahon, Z. Islam, Y. Yamamoto, and I. R. Fisher, "In-Plane Resistivity Anisotropy in an Underdoped Iron Arsenide Superconductor", *Science* **329**, 824 (2010).

[120] M. A. Tanatar, E. C. Blomberg, A. Kreyssig, M. G. Kim, N. Ni, A. Thaler, S. L. Bud'ko, P. C. Canfield, A. I. Goldman, I. I. Mazin, and R. Prozorov, "Uniaxial-strain mechanical detwinning of $CaFe_2As_2$ and $BaFe_2As_2$ crystals: Optical and transport study", *Phys. Rev. B* **81**, 184508 (2010).

[121] B. Valenzuela, E. Bascones, and M. J. Calderón, "Conductivity Anisotropy in the Antiferromagnetic State of Iron Pnictides", *Phys. Rev. Lett.* **105**, 207202 (2010).

[122] R. M. Fernandes, E. Abrahams, and J. Schmalian, "Anisotropic In-Plane Resistivity in the Nematic Phase of the Iron Pnictides", *Phys. Rev. Lett.* **107**, 217002 (2011).

[123] J. J. Ying, X. F. Wang, T. Wu, Z. J. Xiang, R. H. Liu, Y. J. Yan, A. F. Wang, M. Zhang, G. J. Ye, P. Cheng, J. P. Hu, and X. H. Chen, "Measurements of the Anisotropic In-Plane Resistivity of Underdoped FeAs-Based Pnictide Superconductors", *Phys. Rev. Lett.* **107**, 067001 (2011).

[124] E. C. Blomberg, M. A. Tanatar, R. M. Fernandes, B. Shen, H.-H. Wen, J. Schmalian, and R. Prozorov, "Sign-reversal of the in-plane resistivity anisotropy in hole-doped iron pnictides", arXiv:1202.4430.

[125] E. C. Blomberg, A. Kreyssig, M. A. Tanatar, R. M. Fernandes, M. G. Kim, A. Thaler, J. Schmalian, S. L. Bud'ko, P. C. Canfield, A. I. Goldman, and R. Prozorov, "Effect of tensile stress on the in-plane resistivity anisotropy in $BaFe_2As_2$", *Phys. Rev. B* **85**, 144509 (2012).

[126] C. Dhital, Z. Yamani, W. Tian, J. Zeretsky, A. S. Sefat, Z. Wang, R. J. Birgeneau, and S. D. Wilson, "Effect of Uniaxial Strain on the Structural and Magnetic Phase Transitions in $BaFe_2As_2$", *Phys. Rev. Lett.* **108**, 087001 (2012).

[127] E. C. Blomberg, M. A. Tanatar, A. Kreyssig, N. Ni, A. Thaler, R. Hu, S. L. Bud'ko, P. C. Canfield, A. I. Goldman, and R. Prozorov, "In-plane anisotropy of electrical resistivity in strain-detwinned $SrFe_2As_2$", *Phys. Rev. B* **83**, 134505 (2011).

[128] M. Nakajima, S. Ishida, K. Kihou, Y. Tomioka, T. Ito, Y. Yoshida, C. H. Lee, H. Kito, A. Iyo, H. Eisaki, K. M. Kojima, and S. Uchida, "Evolution of the optical spectrum with doping in $Ba(Fe_{1-x}Co_x)_2As_2$", *Phys. Rev. B* **81**, 104528 (2010).

[129] A. Dusza, A. Lucarelli, A. Sanna, S. Massidda, J.-H. Chu, I. R. Fisher, and L. Degiorgi, "Anisotropic in-plane optical conductivity in detwinned $Ba(Fe_{1-x}Co_x)_2As_2$", *New Journal of Physics* **14**, 023020 (2012).

[130] A. Dusza, A. Lucarelli, F. Pfuner, J.-H. Chu, I. R. Fisher, and L. Degiorgi, "Anisotropic charge dynamics in detwinned $Ba(Fe_{1-x}Co_x)_2As_2$", *EPL (Europhysics Letters)* **93**, 37002 (2011).

[131] M. Nakajima, T. Liang, S. Ishida, Y. Tomioka, K. Kihou, C. H. Lee, A. Iyo, H. Eisaki, T. Kakeshita, T. Ito, and S. Uchida, "Unprecedented anisotropic metallic state in undoped iron arsenide $BaFe_2As_2$ revealed by optical spectroscopy", *Proceedings of the National Academy of Sciences* **108**, 12238 (2011).

[132] C.-C. Chen, J. Maciejko, A. P. Sorini, B. Moritz, R. R. P. Singh, and T. P. Devereaux, "Orbital order and spontaneous orthorhombicity in iron pnictides", *Phys. Rev. B* **82**, 100504 (2010).

[133] W. Lv and P. Phillips, "Orbitally and magnetically induced anisotropy in iron-based superconductors", *Phys. Rev. B* **84**, 174512 (2011).

[134] A. Damascelli, Z. Hussain, and Z.-X. Shen, "Angle-resolved photoemission studies of the cuprate superconductors", *Rev. Mod. Phys.* **75**, 473 (2003).

[135] T. Shimojima, K. Ishizaka, Y. Ishida, N. Katayama, K. Ohgushi, T. Kiss, M. Okawa, T. Togashi, X.-Y. Wang, C.-T. Chen, S. Watanabe, R. Kadota, T. Oguchi, A. Chainani, and S. Shin, "Orbital-Dependent Modifications of Electronic Structure across the Magnetostructural Transition in $BaFe_2As_2$", *Phys. Rev. Lett.* **104**, 057002 (2010).

[136] Q. Wang, Z. Sun, E. Rotenberg, F. Ronning, E. D. Bauer, H. Lin, R. S. Markiewicz, M. Lindroos, B. Barbiellini, A. Bansil, and D. S. Dessau, "Uniaxial "nematic-like" electronic structure and Fermi surface of untwinned $CaFe_2As_2$", arXiv:1009.0271.

[137] M. Daghofer, Q.-L. Luo, R. Yu, D. X. Yao, A. Moreo, and E. Dagotto, "Orbital-weight redistribution triggered by spin order in the pnictides", *Phys. Rev. B* **81**, 180514 (2010).

[138] M. Yi, D. Lu, J.-H. Chu, J. G. Analytis, A. P. Sorini, A. F. Kemper, B. Moritz, S.-K. Mo, R. G. Moore, M. Hashimoto, W.-S. Lee, Z. Hussain, T. P. Devereaux, I. R. Fisher, and Z.-X. Shen, "Symmetry-breaking orbital anisotropy observed for detwinned $Ba(Fe_{1-x}Co_x)_2As_2$ above the spin density wave transition", *Proceedings of the National Academy of Sciences* **108**, 6878 (2011).

[139] M. Yi, D. H. Lu, R. G. Moore, K. Kihou, C. H. Lee, A. Iyo, H. Eisaki, T. Yoshida, A. Fujimori, and Z. X. Shen, "Electronic reconstruction through the structural and magnetic transitions in detwinned NaFeAs", arXiv:1111.6134.

[140] Y. Zhang, C. He, Z. R. Ye, J. Jiang, F. Chen, M. Xu, Q. Q. Ge, B. P. Xie, J. Wei, M. Aeschlimann, X. Y. Cui, M. Shi, J. P. Hu, and D. L. Feng, "Symmetry breaking via orbital-dependent reconstruction of electronic structure in detwinned NaFeAs", *Phys. Rev. B* **85**, 085121 (2012).

[141] H. Z. Arham, C. R. Hunt, W. K. Park, J. Gillett, S. D. Das, S. E. Sebastian, Z. J. Xu, J. S. Wen, Z. W. Lin, Q. Li, G. Gu, A. Thaler, S. L. Budko, P. C. Canfield, and L. H. Greene, "Gap-like feature in the normal state of $\mathbf{X(Fe_{1-x}Co_x)_2As_2}$, $\mathbf{X = Ba, Sr}$ and $\mathbf{Fe_{1+y}Te}$ revealed by Point Contact Spectroscopy", arXiv:1108.2749.

[142] H. Z. Arham, C. R. Hunt, W. K. Park, J. Gillett, S. D. Das, S. E. Sebastian, Z. J. Xu, J. S. Wen, Z. W. Lin, Q. Li, G. Gu, A. Thaler, S. Ran, S. L. Bud'ko, P. C. Canfield, D. Y. Chung, M. G. Kanatzidis, and L. H. Greene, "Detection of orbital fluctuations above the structural transition temperature in the iron pnictides and chalcogenides", *Phys. Rev. B* **85**, 214515 (2012).

[143] W.-C. Lee and P. W. Phillips, "Non-Fermi Liquid due to Orbital Fluctuations in Iron Pnictide Superconductors", arXiv:1110.5917.

[144] P. Chandra, P. Coleman, and A. I. Larkin, "Ising transition in frustrated Heisenberg models", *Phys. Rev. Lett.* **64**, 88 (1990).

[145] C. Fang, H. Yao, W.-F. Tsai, J. Hu, and S. A. Kivelson, "Theory of electron nematic order in LaFeAsO", *Phys. Rev. B* **77**, 224509 (2008).

[146] C. Xu, M. Müller, and S. Sachdev, "Ising and spin orders in the iron-based superconductors", *Phys. Rev. B* **78**, 020501 (2008).

[147] Villain, J., Bidaux, R., Carton, J.-P., and Conte, R., "Order as an effect of disorder", *J. Phys. France* **41**, 1263 (1980).

[148] C. L. Henley, "Ordering due to disorder in a frustrated vector antiferromagnet", *Phys. Rev. Lett.* **62**, 2056 (1989).

[149] N. D. Mermin and H. Wagner, "Absence of Ferromagnetism or Antiferromagnetism in One- or Two-Dimensional Isotropic Heisenberg Models", *Phys. Rev. Lett.* **17**, 1133 (1966).

[150] Y. Qi and C. Xu, "Global phase diagram for magnetism and lattice distortion of iron-pnictide materials", *Phys. Rev. B* **80**, 094402 (2009).

[151] J. Hu, C. Setty, and S. Kivelson, "Pressure effects on magnetically driven electronic nematic states in iron pnictide superconductors", *Phys. Rev. B* **85**, 100507 (2012).

[152] A. L. Wysocki, K. D. Belashchenko, and V. P. Antropov, "Consistent model of magnetism in ferropnictides", *Nature Physics* **7**, 485 (2011).

[153] P. Goswami, R. Yu, Q. Si, and E. Abrahams, "Spin dynamics of a J_1-J_2 antiferromagnet and its implications for iron pnictides", *Phys. Rev. B* **84**, 155108 (2011).

[154] R. Yu, Z. Wang, P. Goswami, A. Nevidomskyy, Q. Si, and E. Abrahams, "Spin Dynamics of a J_1-J_2-K Model for the Paramagnetic Phase of Iron Pnictides", arXiv:1112.4785.

[155] J. Hu, B. Xu, W. Liu, N.-N. Hao, and Y. Wang, "Unified minimum effective model of magnetic properties of iron-based superconductors", *Phys. Rev. B* **85**, 144403 (2012).

[156] R. M. Fernandes, A. V. Chubukov, J. Knolle, I. Eremin, and J. Schmalian, "Preemptive nematic order, pseudogap, and orbital order in the iron pnictides", *Phys. Rev. B* **85**, 024534 (2012).

[157] I. Eremin and A. V. Chubukov, "Magnetic degeneracy and hidden metallicity of the spin-density-wave state in ferropnictides", *Phys. Rev. B* **81**, 024511 (2010).

[158] F. Krüger, S. Kumar, J. Zaanen, and J. van den Brink, "Spin-orbital frustrations and anomalous metallic state in iron-pnictide superconductors", *Phys. Rev. B* **79**, 054504 (2009).

[159] W. Lv, J. Wu, and P. Phillips, "Orbital ordering induces structural phase transition and the resistivity anomaly in iron pnictides", *Phys. Rev. B* **80**, 224506 (2009).

[160] I. J. Pomeranchuk, "On the stability of a Fermi liquid", *Sov. Phys. JETP* **8**, 361 (1958).

[161] W.-C. Lee and C. Wu, "Theory of unconventional metamagnetic electron states in orbital band systems", *Phys. Rev. B* **80**, 104438 (2009).

[162] S. Raghu, A. Paramekanti, E. A. Kim, R. A. Borzi, S. A. Grigera, A. P. Mackenzie, and S. A. Kivelson, "Microscopic theory of the nematic phase in $Sr_3Ru_2O_7$", *Phys. Rev. B* **79**, 214402 (2009).

[163] E. Bascones, M. J. Calderón, and B. Valenzuela, "Low Magnetization and Anisotropy in the Antiferromagnetic State of Undoped Iron Pnictides", *Phys. Rev. Lett.* **104**, 227201 (2010).

[164] Y. Tokura and N. Nagaosa, "Orbital Physics in Transition-Metal Oxides", *Science* **288**, 462 (2000).

[165] P. Horsch, *Orbital Physics in Transition Metal Oxides: Magnetism and Optics* (John Wiley & Sons, Ltd, 2007), .

[166] J. B. Goodenough, "Theory of the Role of Covalence in the Perovskite-Type Manganites [La, M(II)]MnO_3", *Phys. Rev.* **100**, 564 (1955).

[167] J. Kanamori, "Superexchange interaction and symmetry properties of electron orbitals", *Journal of Physics and Chemistry of Solids* **10**, 87 (1959).

[168] N. Binggeli and M. Altarelli, "Orbital ordering, Jahn-Teller distortion, and resonant x-ray scattering in $KCuF_3$", *Phys. Rev. B* **70**, 085117 (2004).

[169] A. M. Oleś, L. F. Feiner, and J. Zaanen, "Quantum melting of magnetic long-range order near orbital degeneracy: Classical phases and Gaussian fluctuations", *Phys. Rev. B* **61**, 6257 (2000).

[170] J. C. T. Lee, S. Yuan, S. Lal, Y. I. Joe, Y. Gan, S. Smadici, K. Finkelstein, Y. Feng, A. Rusydi, P. M. Goldbart, S. Lance Cooper, and P. Abbamonte, "Two-stage orbital order and dynamical spin frustration in $KCuF_3$", *Nature Physics* **8**, 63 (2012).

[171] M. Liu, L. W. Harriger, H. Luo, M. Wang, R. A. Ewings, T. Guidi, H. Park, K. Haule, G. Kotliar, S. M. Hayden, and P. Dai, "Nature of magnetic excitations in superconducting $BaFe_{1.9}Ni_{0.1}As_2$", *Nature Physics* **8**, 376 (2012).

[172] C.-C. Lee, W.-G. Yin, and W. Ku, "Ferro-Orbital Order and Strong Magnetic Anisotropy in the Parent Compounds of Iron-Pnictide Superconductors", *Phys. Rev. Lett.* **103**, 267001 (2009).

[173] C.-C. Chen, B. Moritz, J. van den Brink, T. P. Devereaux, and R. R. P. Singh, "Finite-temperature spin dynamics and phase transitions in spin-orbital models", *Phys. Rev. B* **80**, 180418 (2009).

[174] R. Applegate, R. R. P. Singh, C.-C. Chen, and T. P. Devereaux, "Phase transitions in spin-orbital models with spin-space anisotropies for iron pnictides: Monte Carlo simulations", *Phys. Rev. B* **85**, 054411 (2012).

[175] T. Nomura, S. W. Kim, Y. Kamihara, M. Hirano, P. V. Sushko, K. Kato, M. Takata, A. L. Shluger, and H. Hosono, "Crystallographic phase transition and high-Tc superconductivity in LaFeAsO:F", *Superconductor Science and Technology* **21**, 125028 (2008).

[176] J. Dong, H. J. Zhang, G. Xu, Z. Li, G. Li, W. Z. Hu, D. Wu, G. F. Chen, X. Dai, J. L. Luo, Z. Fang, and N. L. Wang, "Competing orders and spin-density-wave instability in $La(O_{1-x}F_x)FeAs$", *EPL (Europhysics Letters)* **83**, 27006 (2008).

[177] H. Luetkens, H.-H. Klauss, M. Kraken, F. J. Litterst, T. Dellmann, R. Klingeler, C. Hess, R. Khasanov, A. Amato, C. Baines, M. Kosmala, O. J. Schumann, M. Braden, J. Hamann-Borrero, N. Leps, A. Kondrat, G. Behr, J. Werner, and B. Buchner, "The electronic phase diagram of the $LaO_{1-x}F_xFeAs$ superconductor", *Nature Materials* **8**, 305 (2009).

[178] T. Yildirim, "Origin of the 150-K Anomaly in LaFeAsO: Competing Antiferromagnetic Interactions, Frustration, and a Structural Phase Transition", *Phys. Rev. Lett.* **101**, 057010 (2008).

[179] P. V. Sushko, A. L. Shluger, M. Hirano, and H. Hosono, "Mechanism of phase transitions and electronic density of states in $LaFeAsO_{1-x}F_x$ and $SmFeAsO_{1-x}F_x$ from ab initio density functional calculations", *Phys. Rev. B* **78**, 172508 (2008).

[180] R. R. P. Singh, "Exchange Constants and Neutron Spectra of Iron Pnictide Materials", arXiv:0903.4408.

[181] A. Akrap, J. J. Tu, L. J. Li, G. H. Cao, Z. A. Xu, and C. C. Homes, "Infrared phonon anomaly in $BaFe_2As_2$", *Phys. Rev. B* **80**, 180502 (2009).

[182] J. Wu and P. Phillips, "Magnon-mediated pairing and isotope effect in iron-based superconductors", *Journal of Physics: Condensed Matter* **23**, 094203 (2011).

[183] K. Vladár and A. Zawadowski, "Theory of the interaction between electrons and the two-level system in amorphous metals. I. Noncommutative model Hamiltonian and scaling of first order", *Phys. Rev. B* **28**, 1564 (1983).

[184] K. Vladár and A. Zawadowski, "Theory of the interaction between electrons and the two-level system in amorphous metals. II. Second-order scaling equations", *Phys. Rev. B* **28**, 1582 (1983).

[185] K. Vladár and A. Zawadowski, "Theory of the interaction between electrons and the two-level system in amorphous metals. III. Experimentally observable quantities", *Phys. Rev. B* **28**, 1596 (1983).

[186] S. Katayama, S. Maekawa, and H. Fukuyama, "Kondo-like Effect of Atomic Motion on Resistivity in $Pb_{1-x}Ge_xTe$", *Journal of the Physical Society of Japan* **56**, 697 (1987).

[187] J. Dai, G. Cao, H.-H. Wen, and Z. Xu, "Possible Kondo effect in the iron arsenides", arXiv:0901.2787.

[188] C. Zener, "Interaction between the *d*-Shells in the Transition Metals. II. Ferromagnetic Compounds of Manganese with Perovskite Structure", *Phys. Rev.* **82**, 403 (1951).

[189] P. W. Anderson and H. Hasegawa, "Considerations on Double Exchange", *Phys. Rev.* **100**, 675 (1955).

[190] P. G. de Gennes, "Effects of Double Exchange in Magnetic Crystals", *Phys. Rev.* **118**, 141 (1960).

[191] A. M. Turner, F. Wang, and A. Vishwanath, "Kinetic magnetism and orbital order in iron telluride", *Phys. Rev. B* **80**, 224504 (2009).

[192] H.-H. Kuo, J.-H. Chu, S. C. Riggs, L. Yu, P. L. McMahon, K. De Greve, Y. Yamamoto, J. G. Analytis, and I. R. Fisher, "Possible origin of the nonmonotonic doping dependence of the in-plane resistivity anisotropy of $Ba(Fe_{1-x}T_x)_2As_2$ (T = Co, Ni and Cu)", *Phys. Rev. B* **84**, 054540 (2011).

[193] J. Kang and Z. Tešanović, "Theory of the valley-density wave and hidden order in iron pnictides", *Phys. Rev. B* **83**, 020505 (2011).

[194] I. Zeljkovic, E. J. Main, T. L. Williams, M. C. Boyer, K. Chatterjee, W. D. Wise, Y. Yin, M. Zech, A. Pivonka, T. Kondo, T. Takeuchi, H. Ikuta, J. Wen, Z. Xu, G. D. Gu, E. W. Hudson, and J. E. Hoffman, "Scanning tunnelling microscopy imaging of symmetry-breaking structural distortion in the bismuth-based cuprate superconductors", *Nature Materials* **11**, 585 (2012).

[195] E. Kaneshita, T. Morinari, and T. Tohyama, "Modeling the Antiferromagnetic Phase in Iron Pnictides: Weakly Ordered State", *Phys. Rev. Lett.* **103**, 247202 (2009).

[196] K. Sugimoto, E. Kaneshita, and T. Tohyama, "Origin of In-Plane Anisotropy in Optical Conductivity for Antiferromagnetic Metallic Phase of Iron Pnictides", *Journal of the Physical Society of Japan* **80**, 033706 (2011).

[197] A. H. Nevidomskyy, "Interplay of orbital and spin ordering in the iron pnictides", arXiv:1104.1747.

[198] P. Richard, K. Nakayama, T. Sato, M. Neupane, Y.-M. Xu, J. H. Bowen, G. F. Chen, J. L. Luo, N. L. Wang, X. Dai, Z. Fang, H. Ding, and T. Takahashi, "Observation of Dirac Cone Electronic Dispersion in $BaFe_2As_2$", *Phys. Rev. Lett.* **104**, 137001 (2010).

[199] Z. P. Yin, K. Haule, and G. Kotliar, "Magnetism and charge dynamics in iron pnictides", *Nature Physics* **7**, 294 (2011).

[200] N. Harrison, R. D. McDonald, and J. Singleton, "Cuprate Fermi Orbits and Fermi Arcs: The Effect of Short-Range Antiferromagnetic Order", *Phys. Rev. Lett.* **99**, 206406 (2007).

[201] A. Jesche, C. Krellner, M. de Souza, M. Lang, and C. Geibel, "Coupling between the structural and magnetic transition in CeFeAsO", *Phys. Rev. B* **81**, 134525 (2010).

[202] D.-Y. Liu, Y.-M. Quan, D.-M. Chen, L.-J. Zou, and H.-Q. Lin, "Ferro-orbital order induced by electron-lattice coupling in orthorhombic iron pnictides", *Phys. Rev. B* **84**, 064435 (2011).

[203] M. S. Laad and L. Craco, "Theory of the unusual high-temperature anisotropic resistivity of underdoped iron arsenide superconductors: Evidence for an orbital nematic order", *Phys. Rev. B* **84**, 054530 (2011).

[204] H.-H. Wen, G. Mu, L. Fang, H. Yang, and X. Zhu, "Superconductivity at 25 K in hole-doped $(La_{1-x}Sr_x)OFeAs$", *EPL (Europhysics Letters)* **82**, 17009 (2008).

[205] S. A. Kivelson and H. Yao, "Iron-based superconductors: Unity or diversity?", *Nature Materials* **7**, 927 (2008).

[206] J. Zaanen, "Condensed-matter physics: The pnictide code", *Nature* **457**, 546 (2009).

[207] Z. Tesanovic, "Are iron pnictides new cuprates?", *Physics* **2**, 60 (2009).

[208] Y. Chen, J. W. Lynn, J. Li, G. Li, G. F. Chen, J. L. Luo, N. L. Wang, P. Dai, C. dela Cruz, and H. A. Mook, "Magnetic order of the iron spins in NdFeAsO", *Phys. Rev. B* **78**, 064515 (2008).

[209] J. Zhao, Q. Huang, C. de la Cruz, J. W. Lynn, M. D. Lumsden, Z. A. Ren, J. Yang, X. Shen, X. Dong, Z. Zhao, and P. Dai, "Lattice and magnetic structures of PrFeAsO, $PrFeAsO_{0.85}F_{0.15}$, and $PrFeAsO_{0.85}$", *Phys. Rev. B* **78**, 132504 (2008).

[210] J. Zhao, W. Ratcliff, J. W. Lynn, G. F. Chen, J. L. Luo, N. L. Wang, J. Hu, and P. Dai, "Spin and lattice structures of single-crystalline $SrFe_2As_2$", *Phys. Rev. B* **78**, 140504 (2008).

[211] S. A. J. Kimber, D. N. Argyriou, F. Yokaichiya, K. Habicht, S. Gerischer, T. Hansen, T. Chatterji, R. Klingeler, C. Hess, G. Behr, A. Kondrat, and B. Büchner, "Magnetic ordering and negative thermal expansion in PrFeAsO", *Phys. Rev. B* **78**, 140503 (2008).

[212] S. D. Wilson, Z. Yamani, C. R. Rotundu, B. Freelon, E. Bourret-Courchesne, and R. J. Birgeneau, "Neutron diffraction study of the magnetic and structural phase transitions in $BaFe_2As_2$", *Phys. Rev. B* **79**, 184519 (2009).

[213] L. Craco, M. S. Laad, S. Leoni, and H. Rosner, "Normal-state correlated electronic structure of iron pnictides from first principles", *Phys. Rev. B* **78**, 134511 (2008).

[214] K. Nakamura, R. Arita, and M. Imada, "*Ab initio* Derivation of Low-Energy Model for Iron-Based Superconductors LaFeAsO and LaFePO", *Journal of the Physical Society of Japan* **77**, 093711 (2008).

[215] V. Vildosola, L. Pourovskii, R. Arita, S. Biermann, and A. Georges, "Bandwidth and Fermi surface of iron oxypnictides: Covalency and sensitivity to structural changes", *Phys. Rev. B* **78**, 064518 (2008).

[216] V. Anisimov, D. Korotin, S. Streltsov, A. Kozhevnikov, J. Kune, A. Shorikov, and M. Korotin, "Density-functional calculation of the Coulomb repulsion and correlation strength in superconducting LaFeAsO", *JETP Letters* **88**, 729 (2008).

[217] P. M. R. Brydon and C. Timm, "Spin excitations in the excitonic spin-density-wave state of the iron pnictides", *Phys. Rev. B* **80**, 174401 (2009).

[218] J. Knolle, I. Eremin, A. V. Chubukov, and R. Moessner, "Theory of itinerant magnetic excitations in the spin-density-wave phase of iron-based superconductors", *Phys. Rev. B* **81**, 140506 (2010).

[219] H. C. Jiang, F. Krüger, J. E. Moore, D. N. Sheng, J. Zaanen, and Z. Y. Weng, "Phase diagram of the frustrated spatially-anisotropic $S = 1$ antiferromagnet on a square lattice", *Phys. Rev. B* **79**, 174409 (2009).

[220] G. S. Uhrig, M. Holt, J. Oitmaa, O. P. Sushkov, and R. R. P. Singh, "Pnictides as frustrated quantum antiferromagnets close to a quantum phase transition", *Phys. Rev. B* **79**, 092416 (2009).

[221] R. Applegate, J. Oitmaa, and R. R. P. Singh, "Spin waves in J_{1a}-J_{1b}-J_2 orthorhombic square-lattice Heisenberg models: Application to iron pnictide materials", *Phys. Rev. B* **81**, 024505 (2010).

[222] B. Schmidt, M. Siahatgar, and P. Thalmeier, "Frustrated local-moment models for iron pnictide magnetism", *Phys. Rev. B* **81**, 165101 (2010).

[223] W.-C. Lee and C. Wu, "Spectroscopic Imaging Scanning Tunneling Microscopy as a Probe of Orbital Structures and Ordering", *Phys. Rev. Lett.* **103**, 176101 (2009).

[224] M. A. McGuire, A. D. Christianson, A. S. Sefat, B. C. Sales, M. D. Lumsden, R. Jin, E. A. Payzant, D. Mandrus, Y. Luan, V. Keppens, V. Varadarajan, J. W. Brill, R. P. Hermann, M. T. Sougrati, F. Grandjean, and G. J. Long, "Phase transitions in LaFeAsO: Structural, magnetic, elastic, and transport properties, heat capacity and Mössbauer spectra", *Phys. Rev. B* **78**, 094517 (2008).

[225] J. van den Brink and D. Khomskii, "Double Exchange via Degenerate Orbitals", *Phys. Rev. Lett.* **82**, 1016 (1999).

[226] J. van den Brink, G. Khaliullin, and D. Khomskii, "Charge and Orbital Order in Half-Doped Manganites", *Phys. Rev. Lett.* **83**, 5118 (1999).

[227] J. van den Brink and D. Khomskii, "Orbital ordering of complex orbitals in doped Mott insulators", *Phys. Rev. B* **63**, 140416 (2001).

[228] D. Senff, F. Krüger, S. Scheidl, M. Benomar, Y. Sidis, F. Demmel, and M. Braden, "Spin-Wave Dispersion in Orbitally Ordered $La_{1/2}Sr_{3/2}MnO_4$", *Phys. Rev. Lett.* **96**, 257201 (2006).

[229] D. R. Neuber, M. Daghofer, A. M. Olés, and W. von der Linden, "Two-band ferromagnetic Kondo lattice model on a ladder with quantum $S = 3/2$ core spins", *physica status solidi (c)* **3**, 32 (2006).

[230] E. L. Nagaev, "Magnon spectrum at the non-RKKY indirect exchange in conducting ferromagnets", *Phys. Rev. B* **58**, 827 (1998).

[231] D. I. Golosov, "Spin Wave Theory of Double Exchange Ferromagnets", *Phys. Rev. Lett.* **84**, 3974 (2000).

[232] N. Shannon and A. V. Chubukov, "Spin-wave expansion, finite temperature corrections, and order from disorder effects in the double exchange model", *Phys. Rev. B* **65**, 104418 (2002).